Numerical assessment of earthquake-induced pounding damage in unreinforced brick masonry buildings using DE macro-crack networks

Zinan Zhang

Department of Civil Engineering

McGill University, Montreal

June 2023

A thesis submitted to McGill University in partial fulfillment of the requirements of the degree of Master of Engineering.

Abstract

Old buildings were often constructed adjacent to each other, without the minimum gap recommended by modern codes. This further increases their seismic vulnerability by exposure to the risk of pounding, a complex mechanism involving repeated impacts between adjacent buildings. Although post-earthquake surveys worldwide confirmed that seismic pounding can significantly increase the extent of in-plane damage and cause early collapses, this phenomenon still remains largely unexplored, while ad-hoc assessment guidelines are missing. This preliminary study focuses on investigating the mechanical in-plane interaction among low-rise unreinforced masonry (URM) buildings of clay brick, a seismically vulnerable yet common structural typology across Canada and abroad. Main novelties consist in the unprecedented use for this task of experimentally validated numerical models developed in the Distinct Element Method (DEM) framework, enabling us to map accurately crack propagation up to collapse, as well as the quantification of key material and geometrical factors affecting earthquake performance. To reduce the otherwise prohibitive computational expense typically entailed by DEM and consider building-scale models, a new macro-modelling strategy is devised that idealizes masonry as an assembly of solid rigid blocks connected by nonlinear interface springs, forming an equivalent macro-crack network where failure occurs according to linearized softening joint constitutive laws. Using this expedited yet accurate analysis technique, firstly, a parametric study is conducted to investigate the influencing factors of pounding of adjacent URM façades including varying height, material degradation levels and the number of adjacent buildings, tested under pushover loading schemes. Then, a comprehensive numerical study of a fixed configuration model is carried out using acceleration time histories of various intensities. Preliminary results, which allowed a comparison

of structural response associated with each acceleration time history, seem to suggest that the pounding impact force is particularly dependent on the strength of the ground motion and poundings have the most pronounced effects when buildings are subjected to moderate-intensity earthquakes.

Résumé

Les anciens bâtiments étaient souvent construits les uns à côté des autres, sans l'espace minimum recommandé par les codes modernes. Cela augmente encore leur vulnérabilité sismique en les exposant au risque de martèlement, un mécanisme complexe impliquant des impacts répétés entre des bâtiments adjacents. Bien que des enquêtes post-sismiques dans le monde entier aient confirmé que le martèlement sismique peut augmenter considérablement l'étendue des dommages en plan et entraîner des effondrements prématurés, ce phénomène reste largement inexploré, tandis que des lignes directrices d'évaluation ad hoc font défaut. Cette étude préliminaire vise à étudier l'interaction mécanique en plan entre les bâtiments de maçonnerie non armée (URM) de faible hauteur en briques d'argile, une typologie structurelle séismiquement vulnérable mais courante au Canada et à l'étranger. Les principales nouveautés consistent en l'utilisation sans précédent, pour cette tâche, de modèles numériques validés expérimentalement développés dans le cadre de la méthode des éléments distincts (DEM), nous permettant de cartographier avec précision la propagation des fissures jusqu'à l'effondrement, ainsi que la quantification des facteurs matériels et géométriques clés affectant la performance sismique. Pour réduire les coûts de calcul autrement prohibitifs généralement associés à DEM et considérer des modèles à l'échelle du bâtiment, une nouvelle stratégie de macro-modélisation est élaborée qui idéalise la maçonnerie comme un assemblage de blocs rigides solides reliés par des ressorts d'interface non linéaires, formant un réseau de macro-fissures équivalent où la défaillance se produit selon des lois constitutives linéarisées d'interface adoucie. En utilisant cette technique d'analyse rapide mais précise, une étude paramétrique est d'abord menée pour étudier les facteurs influençant le martèlement des façades d'URM adjacentes, notamment la hauteur variable, les niveaux de dégradation des matériaux et le

nombre de bâtiments adjacents, testés selon des schémas de chargement à poussée. Ensuite, une étude numérique complète d'un modèle de configuration fixe est effectuée à l'aide de séismogrammes d'accélération de différentes intensités. Les résultats préliminaires, qui ont permis une comparaison de la réponse structurale associée à chaque séismogramme d'accélération, semblent suggérer que la force d'impact du martèlement dépend particulièrement de la puissance du mouvement du sol et que les martèlements ont les effets les plus prononcés lorsque les bâtiments sont soumis à des séismes de moyenne intensité.

Acknowledgements

I would like to express my sincere gratitude to my supervisor, Prof. Daniele Malomo, for his invaluable support and guidance throughout my research journey. His mentorship and expertise have been instrumental in shaping the direction and scope of my thesis. Professor Malomo gave me the opportunity to transfer from a non-thesis student to a thesis student and took me under his wing as one of his students. He has been patient, supportive, and always available to answer my questions and provide insightful feedback on my writing. His instructions and accompanying will have a significant influence on my later academic and career life.

I am also deeply grateful to my wife, who has been a constant source of love, encouragement, and support despite the distance that separates us. Her unwavering belief in me has given me the strength to persevere through the challenges of graduate school. I would also like to thank my parents for their unwavering financial and emotional support, which has allowed me to pursue my academic goals at McGill.

I owe a debt of gratitude to my friends at McGill, who have enriched my experience with their diverse perspectives and shared their cultures and experiences with me. Their company and inspiration have been invaluable in keeping me motivated and engaged in my studies.

Lastly, I would like to thank myself for never giving up and always striving to become better. The journey of completing a master's thesis has not been easy, but it has been immensely rewarding, and I am proud of what I have accomplished.

Contribution of Authors

This thesis has been written following the requirements of Graduate and Postdoctoral Studies for a manuscript-based thesis. The main findings of the research undertaken by the author as part of his master’s program are presented in a single manuscript. The author carried out the numerical analysis and wrote the manuscript under the supervision of Prof. Daniele Malomo (supervisor).

Contents

List of Figures

List of Tables

Chapter 1 - Introduction

1.1 Structural characteristics and seismic vulnerability of unreinforced masonry structures

Old unreinforced masonry (URM) buildings, erected before the introduction of robust seismic design codes, represent the main structural type in many densely populated and earthquake-prone cities globally (Lagomarsino & Cattari, 2015). The lack of seismic detailing and the presence of non-engineered structural systems, including unreinforced loadbearing members, flexible diaphragm and poor connections among components, make URM buildings particularly vulnerable to horizontal actions. Indeed, post-earthquake surveys worldwide have identified failures of URM structures as the leading cause of fatalities and economic losses in old urban centers (So & Spence, 2013) (see **Figure 1.1**).

Figure 1.1. Earthquake damage to URM structures in the 1989 Loma Prieta earthquake (California, USA) (SEAONC, 1992)

URM itself is inherently prone to brittle failures under earthquake motions. Being a highly anisotropic, nonlinear and inhomogeneous material, its primary source of weakness is related to the mechanical properties of constituting components (units and mortar), the presence of unevenly distributed joints, but also geometrical irregularities and material discontinuities (Asteris et al., 2015). During earthquakes, collapses are often induced by stress concentrations, as URM members are typically not able to dissipate energy through large inelastic deformations (Bruneau, 1994), causing cracks that may suddenly propagate primarily through mortar joints, units or both (Lourenço & Rots, 1997). The dynamic behaviour of URM also typically entails the activation of complex and sometimes conflicting aspects of the response, depending on the masonry and diaphragm type, the interaction between in-plane (IP) and out-of-plane (OOP) actions, as well as the number of stories and the degree of plan irregularity. In general, modern masonry structures with adequate wall-to-wall and wall-to-floor connections tend to activate more ductile (and thus more desirable from an earthquake engineering perspective) IP global responses (box-type behaviour), while non-engineered URM buildings often exhibit local OOP failures which prevent the full exploitation of their IP capacity (Abrams et al., 2017). However, due to different material availability, climate conditions and construction traditions, the structural typologies of URM buildings can vary considerably from region to region, further increasing the variability in their seismic response due to complementary factors, e.g. local ground motion characteristics.

The IP behaviour of URM structures mainly depends on the geometry of piers, spandrels and the presence of openings (Magenes & Calvi, 1997), in addition to material properties. The schematics of typical IP collapse mechanisms of masonry walls (note that also spandrel elements may suffer analogous damage, albeit compressive failure is seldom observed), namely flexural, diagonal shear and sliding shear failures, are graphically represented in **Figure 1.2**.

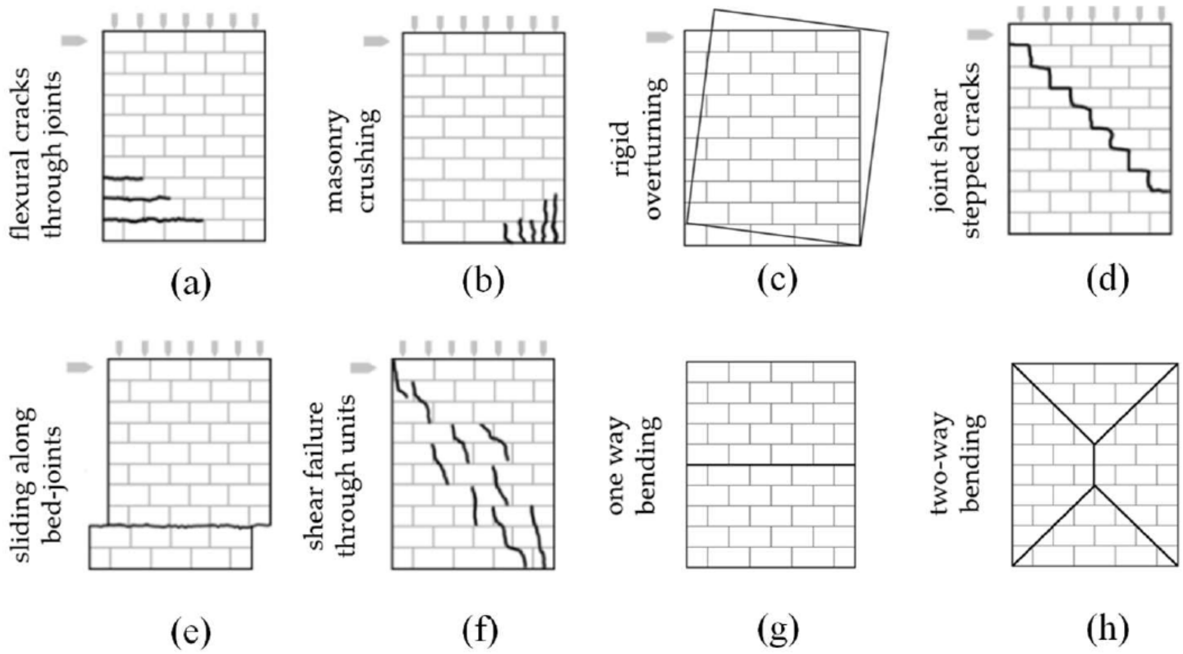

Figure 1.2. IP failure mode of a URM wall: (a) flexural failure mode with cracks through bed joints, (b) masonry crushing in compression, (c) rigid overturning, d) diagonal shear failure with stepped cracks through joints, (e) sliding along bed joints, and (f) diagonal shear failure with cracks through bricks. OOP failure mode of a URM wall: (g) one-way bending, and (h) two-way bending.

As depicted in **Figure 1.2a-b**, the flexural failure mode is caused by the excessive vertical loads that exceed the masonry bearing capacity, leading to the progressive rupture of the tensile zone and crushing the pier in the compressive area. The diagonal-shear failure mode, as shown in **Figure 1.2d**, is associated with the excessive shear force that forms the diagonal cracks along the direction of the principal compression stresses. Moreover, the sliding-shear failure is associated with the sliding-shear failure mode due to the formation of cracks parallel to the bed joints (see **Figure 1.2e**). On the other hand, the OOP failure of URM buildings is somewhat complex, which primarily depends on the connection between walls and floors/roof, the connection between transverse and longitudinal walls, and the IP stiffness of the floors (Mendes & Lourenço, 2014). Without proper connections, the masonry wall will lose its 'box behaviour' and be highly vulnerable to OOP failure, as shown in **Figure 1.2g-h**, due to different boundary conditions (Giordano et al., 2020).

1.2 Seismic pounding definitions and backgrounds

Structural pounding refers to the lateral collision of adjacent buildings during lateral dynamic loads, including wind and earthquakes. This thesis refers exclusively to earthquake-induced (or seismic) pounding, which tends to occur when there are insufficient building distances to accommodate the relative motions of adjacent buildings (Kasai and Maison 1997). The generated repeated impacts are often the cause of increased damage to structural members and/or non-structural components of the buildings (Filiatrault and Cervantes 1995).

Prior to the release of modern building codes (i.e., International Building Code (IBC) 2018, National Building Code of Canada (NBCC) 2015), the separation between adjacent buildings for seismic purposes was not required. Yet many old urban centers are characterized by predominantly masonry structures constructed progressively and with little to no separation between adjacent buildings (Rezavandi & Moghadam, 2007). URM structures are vulnerable to even moderate levels of seismic loading, often experiencing poor performance under lateral loads, and are the leading cause of seismic fatalities and economic losses worldwide (So & Spence, 2013). In old urban centers, many neighbouring structures built without separation are non-engineered low-rise URM structures (Anagnostopoulos, 1988), representing a serious threat to public safety and architectural heritage. In **Figure 1.3**, old URM building aggregates in Montreal and Quebec City (Quebec) and typical of the whole of Eastern Canada are displayed. These low-rise URM buildings are also common in many other parts of the world (see **Figure 1.3**).

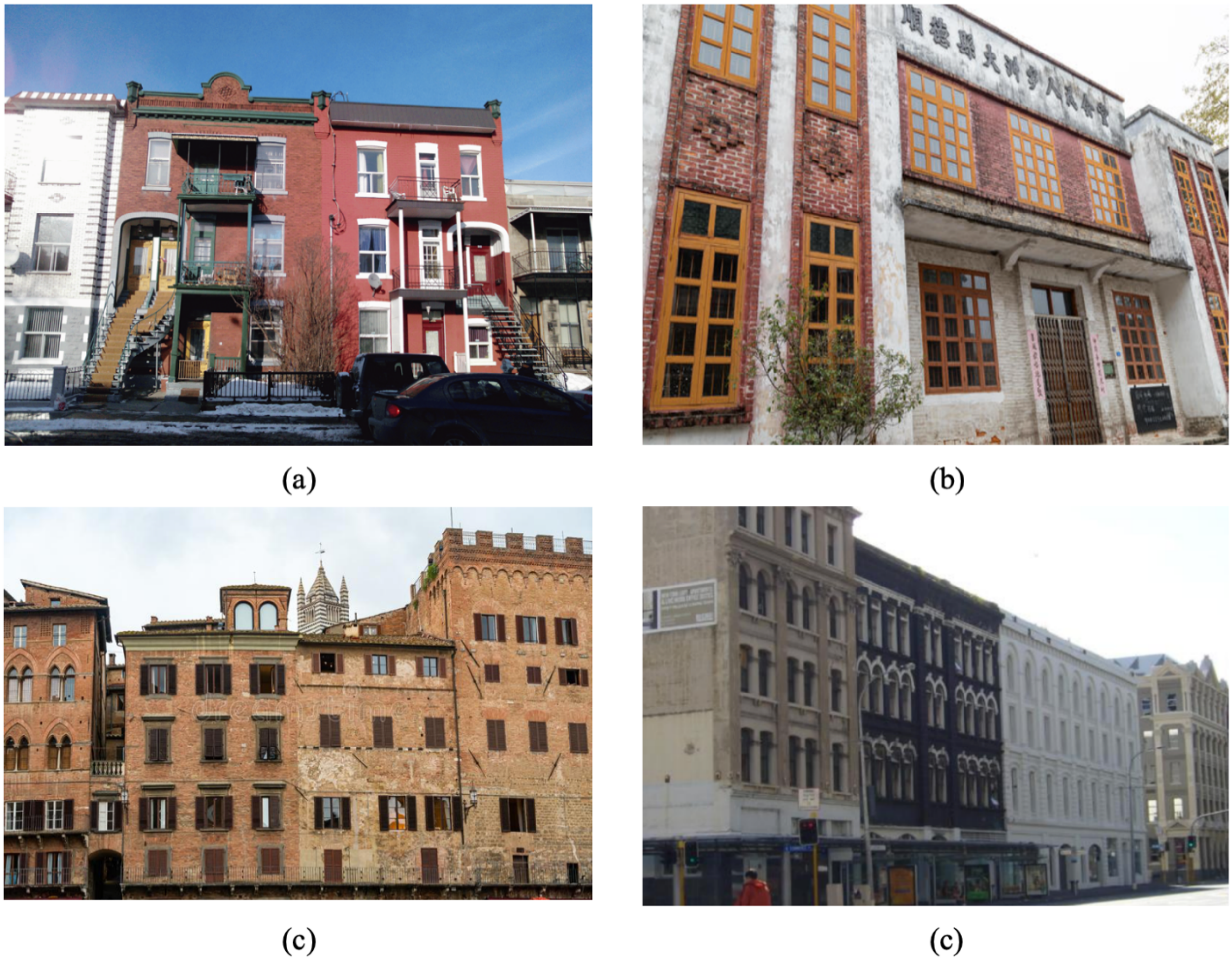

Figure 1.3. Old URM building aggregates in (a) Montreal (Quebec, Canada) (blogspot, 2013), (b) Sichuan (China) (alamy, 2019), (c) Siena (Italy) (dreamstime, 2023), (d) Wellington (New Zealand) (wikidata, 2023)

The pounding effect was not noticed until 1926 when the first book mentioned pounding about earthquake resistance design (Ford, 1926). Since then, there has been a nearly half-century gap. It remained overlooked among professionals and researchers; in 1971, they finally recognized the importance of the pounding problem after the San Fernando Earthquake that pounding caused severe damage to a hospital (Bertero & Collins, 1973).

Since then, many researchers have been devoted to finding the influence of pounding on existing buildings' seismic resisting performance. Crozet and co-authors found that pounding impacts may amplify the structural response of the structure that has higher stiffness. The pounding effects are susceptible to the stiffness of the impact element, as shown in **Figure 1.4.** (Crozet et al., 2019). The interstate drifts of the more rigid structures during the earthquake increased significantly (Rezavandi and Moghadam 2016, Baker 2007). Some evidence also showed that the natural period of the building that subjecting to pounding decreased to roughly half the value if pounding did not exist (R. O. Davis, 1992). Also, the peak acceleration at the pounding level could be more than ten times compared with those without pounding (Kasai et al., 1990). Another analytical study demonstrated that buildings having irregular lateral load-resisting systems result in the pounding effect at or near the building periphery against the adjacent buildings (Kasai & Maison, 1997). Moreover, adjacent buildings with different dynamic characteristics (natural frequencies, damping ratios) or floor levels are more conducive to seismic poundings (Jankowski et al., 2015). The maximum displacement response occurs when the excitation frequency is close to the more flexible building. It is also observed that the changes in distance between structures and ground motions could lead to entirely different pounding phenomena, either periodic or chaotic pounding (Chau et al., 2003). As for the stand-off distance, pounding at the top and the mid-level is possible for buildings with zero separation (less than 3 mm). For nonzero separation distance, the pounding is predominantly at the top (Chau et al., 2006).

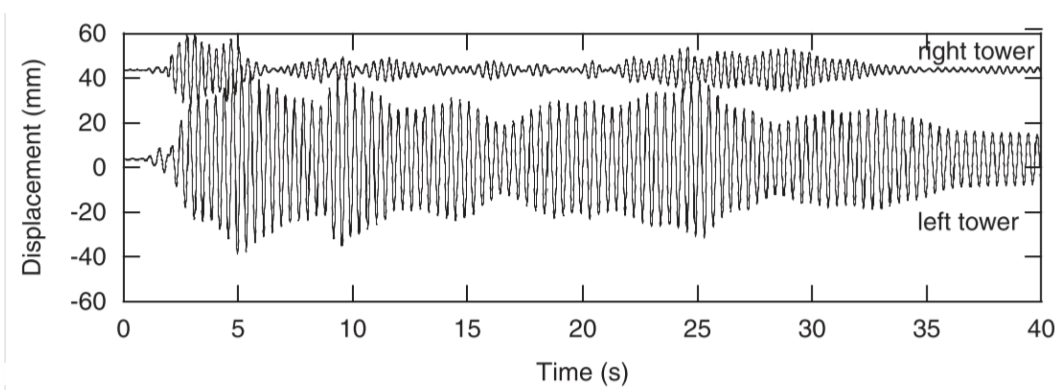

Figure 1.4. Displacement time history of two buildings with different stiffness where the right tower is stiffer than the left tower

In the last few decades, many researchers have come up with solutions to mitigate the problems caused by seismic poundings considering the potential influence factors mentioned above. A traditional mitigation strategy is to increase the individual buildings' stiffness, aiming at reducing their absolute and relative displacement. But this strategy represents the most expensive approach since it may involve a total retrofit of the current structure (Warnotte, 2007). The most direct way is to reduce the pounding effect by expanding the building separations. Although the current building codes prescribe a minimum separation between adjacent buildings, old URM buildings were built in ancient times without including the hazards brought by pounding. On the contrary, the experiment result from Rezavandi (Rezavandi & Moghadam, 2007) is opposite to some existing literature (Kasai et al., 1992). If the increase in distance between buildings is insufficient, the pounding effect may also amplify due to the rise in floor velocity. Some research efforts were devoted to reducing the pounding potential by using impact-absorbing material. Installing the polystyrene decreased the acceleration and displacement response considerably, which benefits non-structural elements (Rezavandi and Moghadam 2016). Adding damping devices or passive energy dissipaters to mitigate pounding between adjacent buildings has been regarded as the most economical and high-efficient solution because they do not affect the stiffness of structures and thus do not affect the dynamic properties. They mainly rely on specially designed instruments that can dissipate a large amount of energy (Monteiro et al., 2014). For example, Kasia found that adding dampers to adjacent buildings could significantly reduce the pounding effect (Kasai et al., 1992).

1.3 Pounding observation in URM buildings after the earthquake

Pounding damage to old URM buildings has been observed and reported in several past earthquakes, from limited hazardous effects to severe effects. For example, during the 1985

Mexico earthquake, pounding was present in over 40% of 330 collapsed or severely damaged buildings surveyed, and in 15% of all cases, it led to collapse (Miranda & Bertero, 1989).

In the 1971 San Fernando earthquake, a series of pounding-induced failures were observed, of which most of the pounding damages were due to buildings located next to each other forming a row in a block. Also, there is some evidence that the end or corner buildings account for the heaviest damage (Anagnostopoulos, 1988). The 1989 Loma Prieta earthquake resulted in pounding between many old multi-story URM buildings having virtually no building separations. The survey showed that most of them (79%) experienced minor damage and only had cosmetic damage and could maintain their primary structural function.

In 2010, a 7.1M earthquake occurred 30 km west of Christchurch, New Zealand (Wood et al., 2010). A photo survey of pounding-damaged structures showed that more severe pounding damage is only in URM buildings. The observed damage cracking and failure of parapets and column and wall cracking in URM buildings. Also, the roof level and parapet damage indicate that OOP shear due to pounding in the protruding interface wall is considered dangerous (see **Figure 1.5**). It could cause complete separation of the front façade and bring hazards to pedestrians (Brown & Elshaer, 2022). Also, during the inspection, almost all pounding-damaged structures were found in URM buildings with tiny building separations (less than 3mm). Therefore, the closely arranged URM buildings are particularly susceptible to pounding damage (Cole et al., 2010).

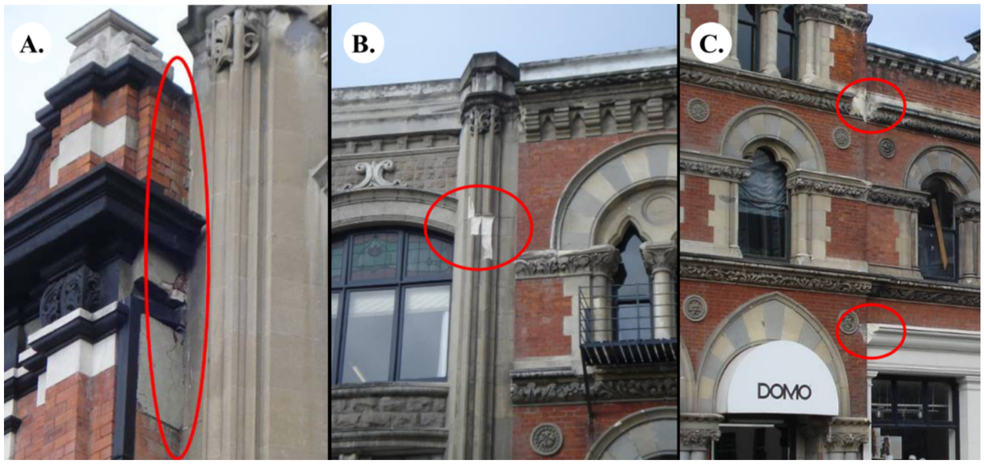

Figure 1.5. Pounding damage to the URM building aggregate (a) damage at the roof level and parapet; (b) masonry spalling; (c) the fell of decorative sections from the wall (Wood et al., 2010)

In recent years, a devastating earthquake in Nepal in 2015 resulted in heavy casualties and the massive collapse of URM buildings. The investigations showed that the severity of pounding damage has close ties with the unique building typologies, loading conditions, and design or construction deficiencies. Notably, it was observed that the pounding risk of URM buildings increased substantially when they were adjacent to reinforced concrete (RC) buildings. In contrast, RC buildings usually result in less severe damage, as shown in **.** (Shrestha & Hao, 2018).

(a) (b) (c)

Figure 1.6. (a) Pounding between RC and masonry building; (b) Severe damage to masonry building; (c) Failure of masonry walls observed from the interior of the building.

1.4 Seismicity and the resulting pounding damage of URM buildings in Eastern Canada.

The seismicity In Eastern Canada has its particular characteristics regarding intensity, frequency, and attenuation of seismic waves. In comparison to the west coast of Canada, most earthquakes in Eastern Canada are of low intensity and high frequency. Also, Due to the special geological structure, seismic waves propagate much further in Eastern Canada than in Western Canada. An example that proved this came from the 1988 Saguenay earthquake in Québec, the earthquake was felt over an exceptionally large area, as far as Thunder Bay (Ontario).

In Eastern Canada, due to the densely populated urban cities, even a moderate earthquake will bring severe damage to historic URM buildings, the cities such as Québec city, Trois-Rivière, Montréal, and Ottawa, located near the St.Lawrence Valley, are especially at substantial risk of pounding damage. Although the seismic hazard on the east coast of Canada is not as significant as the cities in the western part like Vancouver and Victoria, the eastern Canadian cities may be more vulnerable to pounding damage because of the age of their structures and the higher density of closely spaced URM buildings (Filiatrault et al., 1994). In old Montréal alone, almost 44% of buildings are old URM structures (Antunez et al., 2015).

So far, a case of pounding damage to URM buildings in Eastern Canada has been observed due to November 25, 1988, Saguenay earthquake (Quebec), which was the largest recorded seismic event in Eastern North Canada (M=6.0). The overall risk associated with these seismic events remains low in Eastern Canada for most modern buildings. However, old (erected before the first 1941 National Buildings Code of Canada, NBC) non-engineered constructions are predominant in many of eastern Canada's major cities and pose a severe threat to residents and pedestrians (L. Davis & Malomo, 2022). During this earthquake, the ground motion was felt over an extensive area. A case associated with this earthquake was observed at the Notre Dame Pavilion in Québec city. A sevenstory masonry wall was severely cracked when it pounded against an adjacent two-story building (Tinawi et al., 1990).

1.5 Pounding research in URM buildings

In the last 30 years, research on the seismic response of adjacent buildings or building aggregates has mainly been conducted on steel (Sołtysik & Jankowski, 2016), reinforced concrete (RC) buildings (Karayannis & Favvata, 2005), and their interactions (Kazemi et al., 2021) either experimentally or numerically. Several researchers compare the numerical analysis results to that of the lab test of both steel and RC structures (Rezavandi and Moghadam, 2016; Crozet, Politopoulos, and Chaudat, 2019), which showed acceptable agreements concerning IP motions, maximum displacements, and maximum accelerations owing to their isotropic material constitution as well as typical architectural style, where pounding effects are modelled through contact elements (Khatiwada et al., 2013), mass-dashpot assemblies (Ghandil & Aldaikh, 2017), or non-linear impact stiffness (Pulatsu et al., 2016).

On the other hand, because of the brittle, highly nonlinear anisotropic behaviour and failure mechanisms of the URM buildings, they could not be modelled either as single-degree-of-freedom (SDOF) (Anagnostopoulos, 1988) or multi-degree-of-freedom (MDOF) models (Anagnostopoulos & Spiliopoulos, 1992) to precisely simplify the structural configurations to investigate the complex pounding phenomenon (Mohebi et al., 2021). Similarly, numerical simulations of the URM buildings need more intricate details to account for the unique characteristics of URM buildings (spatial irregularities, influence of diaphragm stiffness, and opening layout). Thus, numerous endeavours have been undertaken to develop models for URM buildings, and such efforts can be broadly categorized into two primary methodologies: continuum-based and discrete models. In continuum-based analysis, Finite Element Modeling

(FEM) has been applied to Erdogan's study that detailed modelled the seismic behaviour of historical URM buildings under earthquake motion (Erdogan et al., 2019). Although a better understanding of the local behaviour of URM buildings in terms of the damage initiation and propagation and better seismic behaviour will get through the FEM approach, it might be computationally expensive if the research object is on a large scale. On the other hand, the Distinct Element Method (DEM) considers individual elements that interact with each other based on finite-difference principles (Orford, 1975) and is successfully used for simulating reduced-scale URM buildings (Pulatsu et al., 2016). In the DEM approach, mortar joints are represented as zero-thickness interfaces between the blocks. Masonry blocks are defined as an assembly of rigid or deformable blocks that may take any arbitrary geometry (Asteris et al., 2015). In the latest years, Equivalent Frame Models (EFM) have become widely accepted in various research on the seismic behaviour of URM buildings (Morandini et al., 2022; Chen et al., 2008); this simplified modelling strategy idealizes masonry into an assembly of deformable elements (i.e., spandrels and piers), connected by rigid regions, buildings a frame of macro-elements. Therefore, the EFM approach reduces the computational cost, allowing it to be employed for professional aims without losing accuracy ((Morandini et al., 2022; Senaldi et al., 2010). In the EFM framework, pounding is modelled in a simplified scope. The interface material is only defined as having zero thickness with linear elastic response in the compression stage and nonlinear tension softening law (Vanin et al., 2020). However, using this simplified approach, the interlocking mechanisms and the crack propagation cannot be accounted for numerically

1.6 Research Motivation

Although considerable investigations of the seismic response of individual URM buildings have been acquired numerically so far (Caliò et al., 2012; Malomo et al., 2019; Tomaževič et al., 1996).

This knowledge is not sufficient to explain some typical aspects of the interaction between adjacent buildings that in aggregate such as the impact mechanisms and the activation of collapses. Furthermore, the seismic response of URM building aggregates is often influenced by the presence of weak links and opening layouts which lead to the complex dynamic actions of each structural unit (Lourenço et al., 2011). For the above reasons, a detailed numerical simulation of the aggregate seismic response requires nonlinear dynamic analysis. This, however, is difficult to be implemented in large-scale buildings because of the high computational costs and extensive implementation time and very few applications concerning the modelling of large structures are documented in the literature (Ferrante et al., 2021; Gonen et al., 2021; Hamp et al., 2022) and in many cases lack experimental comparisons.

Therefore, there is an urgent need to develop a new modelling method that can enable faster numerical simulation with higher accuracy for the pounding response of URM building aggregates. To address this research gap, this study proposes a novel simplified DEM model based on macro-crack networks to reduce computational burden and allow the discrete simulation of the in-plane pounding response of URM building aggregates. To this end, an intuitive and easily applicable novel discretization algorithm is devised, that idealizes actual masonry as an assembly of rigid macro-blocks connected by a network of zero-thickness nonlinear interface springs (recently devised by Pulatsu et al. (2020a), minimizing unwanted scale effects through the use of fracture energy parameters). After this modelling approach is validated against several experimental results through implementation within the 3DEC commercial software framework (Itasca Consulting Group Inc., 2013), it is used to model the IP pounding behaviour of a URM building aggregate containing two façades with the same configuration under eleven different ground motion histories (ranging from low intensity to high intensity). The study concludes by presenting the pounding responses in terms of the pounding damage and pounding intensity.

1.7 Research outline

This research is organized into four subsequent chapters with the following contents:

Chapter 2 presents the proposed framework for DE macro-crack discretization and the selected joint contact-constitutive model. This strategy for macroblock modelling is then validated through a comparison with the results obtained from various laboratory experiments conducted under pushover, cyclic, and dynamic loading conditions. Additionally, the potential of modelling both IP and OOP failure mechanisms is examined.

Chapter 3 begins by analyzing the factors that influence the interaction effects among URM building aggregate under pushover load. The proposed modelling methodology is then applied to a URM building aggregate having two identical connected facades. The response of pounding damage and pounding intensity of this URM building aggregate is recorded and compared under eleven distinct ground motion histories.

Chapter 4 provides the research's conclusions

Chapter 2 – Development and Validation of a New Distinct Element (DE) Macro-crack Network

2.1 Idealizing masonry using DE macro-crack networks

Compared to the traditional macro-modelling methods, this research adopts new DE macro-crack networks (see **Figure 2.1**a) that can form along zero-thickness nonlinear spring interfaces (or joints), where the deformability of the system is lumped and separation (or macro-cracks) occur. The number of joints is fixed for each URM component (pier, spandrel, node – see Lagomarsino et al. 2013), resulting in multi-scale assemblies of eight rectangular interlocking rigid macro-blocks arranged in three layers (Zhang et al., 2023). As shown in **Figure 2.1**b, this simplified discretization scheme was derived from the observation of the most common IP failure modes of both URM spandrels and piers ((Magenes & Calvi, 1997, Beyer and Dazio 2012), namely top sliding (TS), diagonal shear (DS), rocking (R) and toe crushing (C). In order to achieve the idealized failure pattern, macro-blocks are arranged to allow the formation of diagonal cracks, as well as top/bottom horizontal cracks. The resulting macro-crack network is also symmetrical, meaning that the model can be loaded along either horizontal primary load direction.

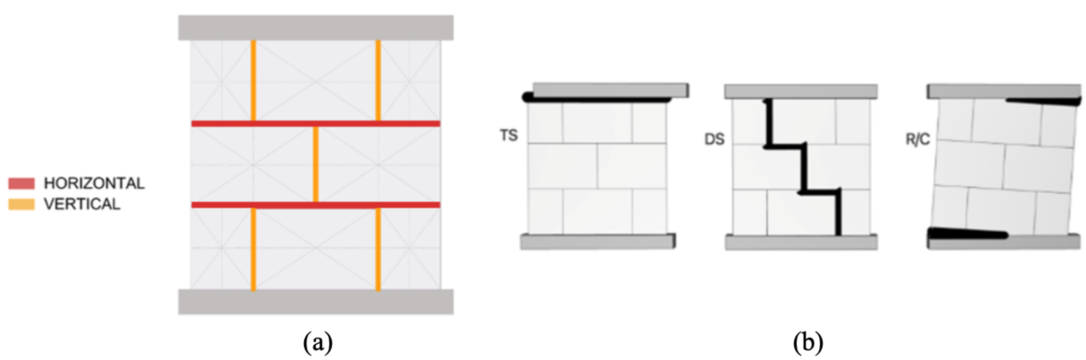

Figure 2.1. (a) A DE Macro-Crack Networks representative of a URM panel, (b) examples of in-plane failure modes

In this DE macro-crack network, the mechanical interaction between adjacent macro-blocks is analyzed along the contact surfaces. Contact stresses are calculated in the normal (σ) and shear (τ) directions based on the assigned contact stiffness of each spring (normal stiffness k_n and shear stiffness k_s) respectively. Inelastic properties of the springs in the normal and shear directions can also be defined, including the tensile strength (f_t), compressive strength (f_c), cohesion (c) and friction angle (ϕ). The same mechanical properties are assigned to both head and bed joints (Malomo & DeJong, 2021a).

2.2 Realization approach of the DE macro-crack networks

Typically, the conventional approach for constructing a 3D discrete model of URM structures is to sequentially place individual bricks side by side and layer by layer in an interlocking pattern using 3D modelling software. This methodology is appropriate for small-scale specimens that contain only few bricks. However, it proves to be inefficient and time-consuming for large-scale URM buildings with various openings of different sizes. Additionally, this laborious and repetitive manual modelling technique may also increase the risks of modelling mistakes. In light of the forthcoming chapter on pounding analysis, which necessitates the modelling of the extensive number of large-scale URM buildings with diverse configurations, there arises a pressing need for a fast and reliable modelling strategy to facilitate the efficient production of 3D discrete macroblocks, thereby obviating the arduous manual modelling technique.

Therefore, an automated geometry-generation code for easily and promptly generating the DE macro-crack network of any 3D configuration was developed using the visual programming language Grasshopper (Robert McNeel and Associates 2007), a plugin for the 3D geometrical modelling software Rhinoceros. **Figure 2.2**a illustrates how this program meshes a planar element into a 3D solid using the aforementioned discretization method to instantly generate readily analyzable DE macro-models. This procedure outlined comprises three steps that are required for the generation of output 3D solids (see **Figure 2.2**b). The initial step involves the introduction of an input surface, represented by a rectangular panel. Subsequently, this panel is partitioned into a mesh comprising a total of twelve sub-regions, with four columns and three rows. The second step involves the extraction of each point within the mesh, which serves as a basis for the generation of eight rectangle curves. The generation of these curves is accomplished via a specific algorithm which uses two point lists containing the diagonal corner points of each rectangle. Finally, the aforementioned set of eight rectilinear curves undergoes a transformation into surfaces, which are subsequently utilized as the foundation for the creation of the ultimate output of 3D solids through the process of extrusion.

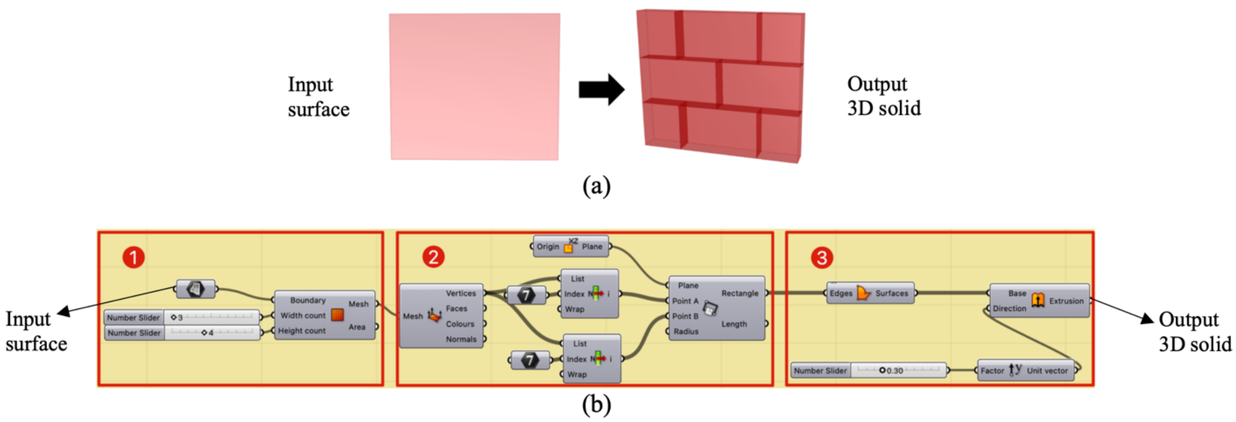

Figure 2.2. (a) a model-generation schematic using Grasshopper, (b) Grasshopper implementation steps

Thus, providing that the geometry element is rectangular, this modelling algorithm could be applied to any component or façade with different aspect ratios and/or opening layouts. In large-scale URM buildings, certain rectangle surfaces are preliminary sketched based on the building's outline and the configuration of openings. Subsequently, the grasshopper algorithm is employed to transform these sketched surfaces into 3D solids in a uniform manner (see **Figure 2.3**). Therefore, this macro modelling approach is particularly suitable for modelling large-scale complex façades to dramatically reduce geometrical modelling time. Moreover, it should be noted that at the vertical interfaces between each two horizontally connected rectangle elements assembling eight rigid macro-blocks (e.g. interfaces between elements 1 and 2, 2 and 3 in **Figure 2.3**), to artificially represent the expected interlocking over-strength, inelastic brick properties are assigned while within each rectangle element, mortar properties are used.

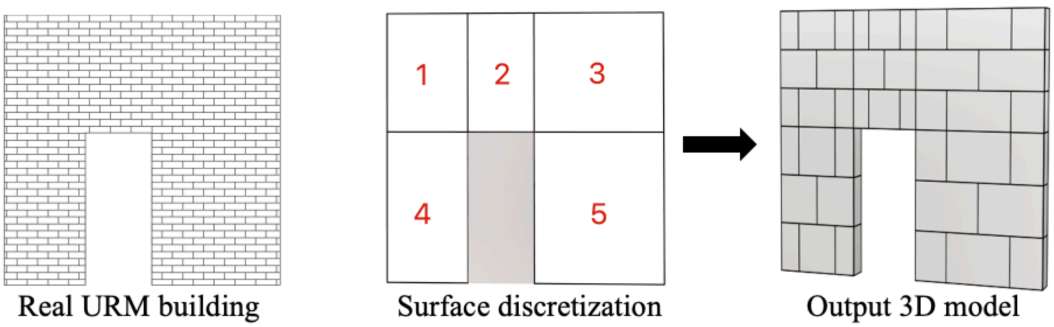

Figure 2.3. Modelling process for large-scale URM building using Grasshopper

2.3 Selecting appropriate block and joint models

In 3DEC, solid elements (i.e., blocks) can be represented as either rigid or deformable blocks. Under applied loads, rigid blocks do not change their geometry while deformable blocks are discretized internally into constant-strain tetrahedral volumes providing deformability within the domain. In general, rigid blocks require much less analysis time than deformable ones; hence, they are more applicable to large-scale simulations.

For both types of blocks (i.e. rigid and deformable) mechanical interaction between them is modelled as a set of point contacts, located at the vertexes. As described in Cundall and Hart (1992), each contact point has three springs (in 3D) which can transfer either normal or shear forces among the adjacent blocks. Brittle and elastic-softening contact models are often used to represent URM joint behaviour in DEM simulations, typically following a Mohr-Coulomb law in shear-compression. In brittle contact models, the joints experience a sudden failure after reaching the peak capacity in tension, while infinite compression is typically used – albeit not adequate when crushing is expected. In softening contact models, the nonlinear post-peak response of the material (both for tension, compression and shear) is considered according to parabolic, multi-linear or linear (i.e. the one considered in this work, developed by Pulatsu et al. (2020), see **Figure 2.4**) functions.

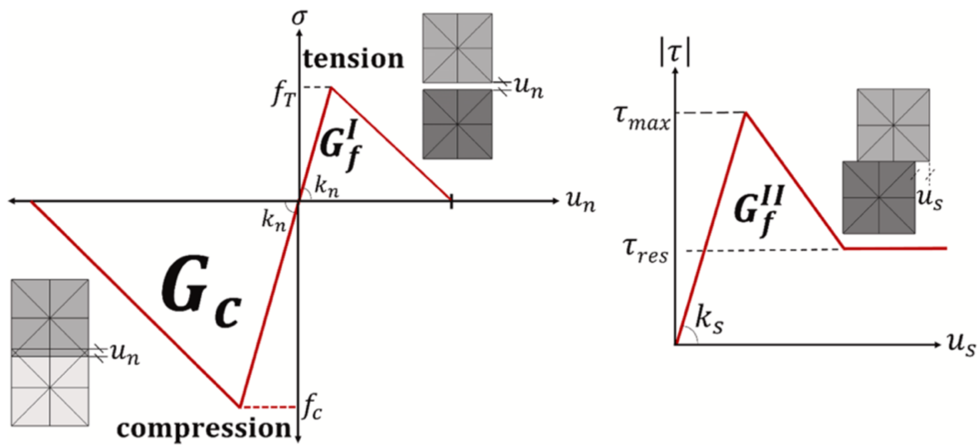

Figure 2.4. Employed strain-softening contact model (Pulatsu et al. 2020)

To select the most appropriate joint contact model and block type in terms of accuracy-efficiency balance, the use of both rigid and deformable blocks, brittle and elastic-softening contact models as well as their combinations, is investigated in this section and produced results compared. To this end, deformable-brittle (D-BJ), deformable-softening (D-SJfc), rigid-brittle (R-BJ), and rigid-softening (R-SJfc) DEM models were created and their performance was evaluated considering the 1x1x0.1 m URM solid clay brick wall tested by Vermeltfoort et al. (1993) under IP quasi-static monotonic load with different initial pre-compression σ were applied (0.3, 1.21, and 2.21MPa). The walls were clamped by two concrete beams on the top and bottom of the wall respectively to avoid the torsional effects and then were subjected to increasing lateral forces (see **Figure 2.5**b).

To avoid the potential influence of block size, a traditional micro-modelling approach was used here to provide a clearer understanding of how these choices may affect the quality of numerical predictions and the effort needed to complete them. In this micro-model, each masonry unit is modelled as a rigid distinct block with a joint defined at the mid-section to consider a potential cracking failure within the bricks. Finally, the wall is discretized into 80 bricks consisting of 144 distinct elements, as shown in **Figure 2.5**. The input parameters are given in **Table 2.1** as referenced by Pulatsu et al. (2020) where within the brick joints, brick properties were used while between the bricks, masonry properties were adopted. In **Table 2.1**, E_m is Young's modulus and G_m is shear modulus ($G_m = 0.4E_m$) that is used to infer normal ($k_n = E_m/L$) and shear ($k_s = G_m/L$) stiffnesses of the interface springs connecting the distance L between the central points of the adjacent blocks. Furthermore, nonlinear behaviour is considered in compression, tension and shear directions by introducing the fracture energy regime which is presented as G_c, G_f^I and G_f^{II}, respectively,

Table 2.1. Selected elastic and inelastic mechanical properties (Pulatsu et al. 2020)

material ID	E_m	G_m	f_c	f_t	c	ϕ	G_c	G_f^I	G_f^{II}
	[MPa]	[MPa]	[MPa]	[MPa]	[MPa]	[°]	[N/m]	[N/m]	[N/m]
Masonry	16700	*6680	5	0.2	0.3	35	*8000	*15	*125
Bricks	16700	*6680	12	*2	*3	*35	*19000	*80	*550

** Test values are missing*

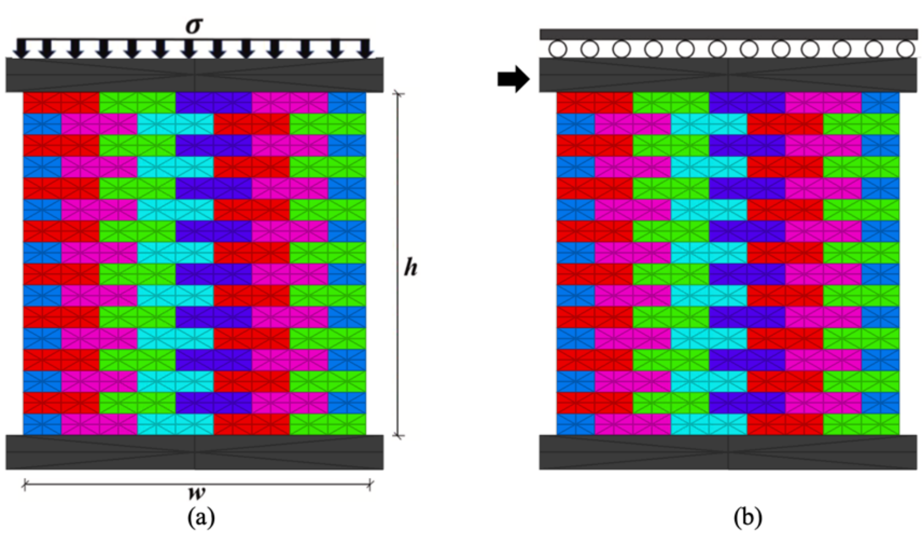

Figure 2.5. Illustration of the analyzed URM solid walls (Lourenço, 1996): (a) Initial vertical loading and (b)

lateral loading

The simulation results are shown in **Figure 2.6**; the analysis time (a computer with Intel Core i7-8650U CPU @ 1.9 GHz processor was used) required to obtain the full stress-displacement curves is summarized in **Figure 2.7**.

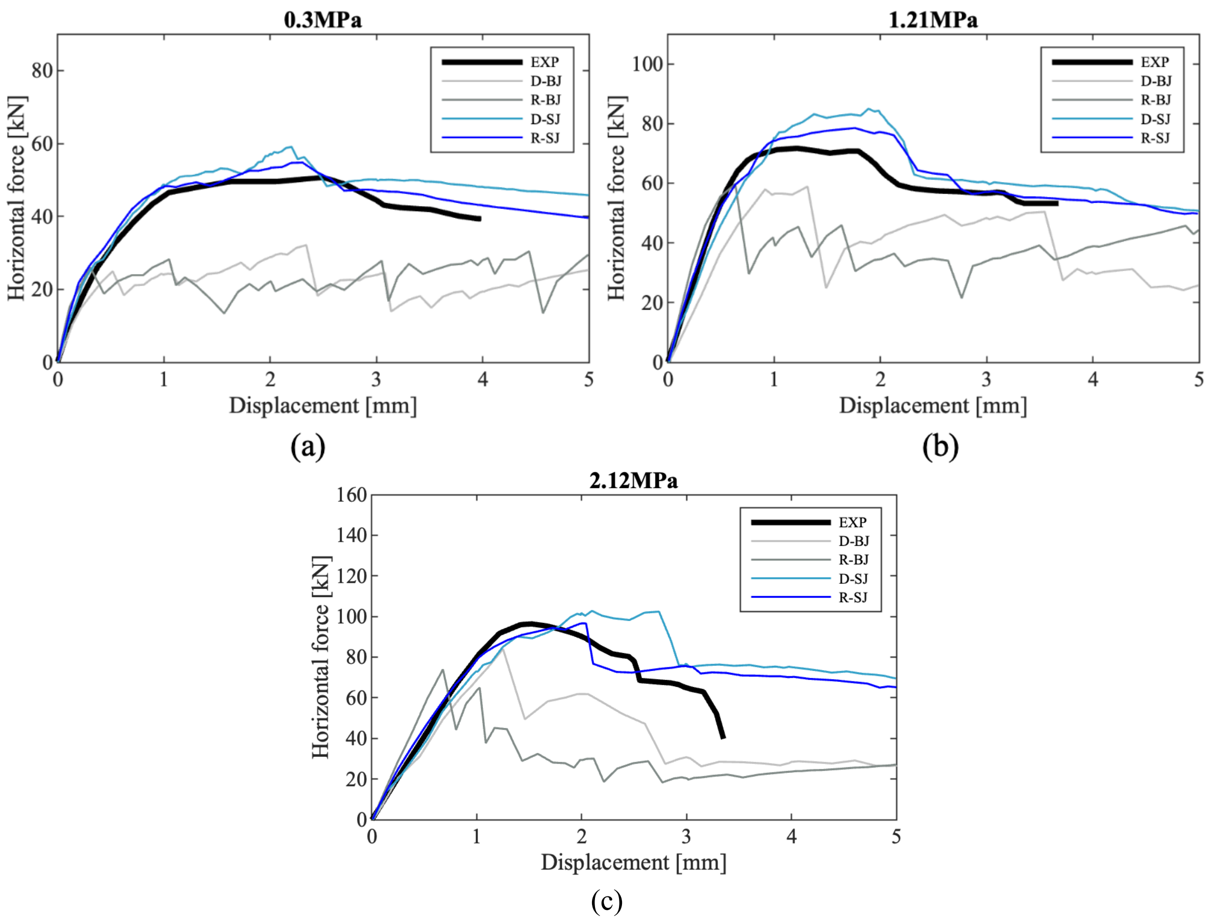

Figure 2.6. Force-displacement curves for different pre-compression conditions (a) 0.3MPa; (b) 1.21MPa; (c)2.12MPa

Based on the findings presented in **Figure 2.6**, it can be inferred that the adoption of both rigid and deformable block models utilizing brittle joints, denoted as R-BJ and D-BJ, respectively, led to a notable underestimation of the lateral strength capacity observed in experimental testing, across all three loading conditions. However, the initial stiffnesses were reasonably predicted, despite abrupt force drops observed during the post-failure phase. On the other hand, the softening contact models R-SJfc and D-SJfc provide better results, and are also more stable in terms of force-displacement curves, well-capturing both peak and residual strengths. No significant differences are observed between the results of rigid and deformable block models with strain-softening joints. Notably, however, running the R-SJfc required 23% less time than its deformable counterpart, D-SJfc (see **Figure 2.7**).

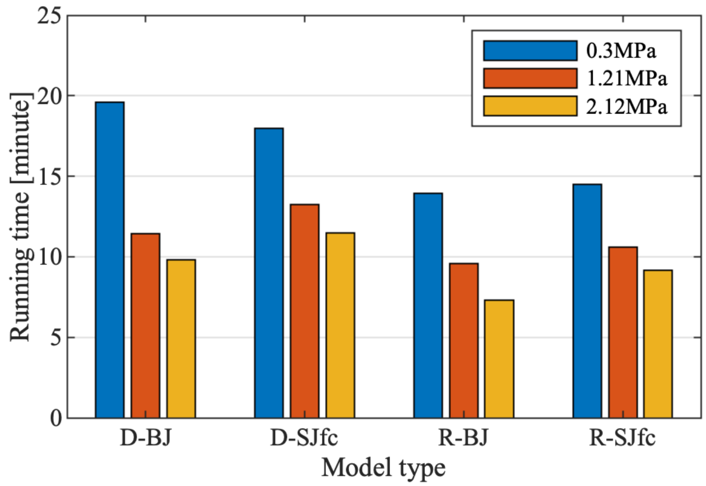

Figure 2.7. Analysis time for all models subjected to three pre-compression conditions

In terms of failure modes (see **Figure 2.8**), the wall exhibited a full diagonal crack which traversed the entirety of the wall, as evidenced by experimental observation. This mode of failure was adequately captured by the softening joint model, which employed either deformable or rigid blocks that was subjected to low (0.3 MPa) and moderate (1.21 MPa) levels of pre-compression. However, under higher vertical pressures (2.12 MPa), cracks developed vertically through the bricks, causing the diagonal cracks to narrow and converge towards the center of the wall which is reasonable theoretically. In contrast, the Brittle joint model failed to accurately depict the aforementioned mode of failure. Specifically, under low pre-compression, the wall failed diagonally, but the head and bed joints suffered discrete damage instead of a continuous diagonal crack. Moreover, only sporadic and irregular cracks were observed under moderate and high pre-compression.

Following the conducted study, the softening joint, rigid block model (R-BJ) has been identified as the most suitable option among the four proposed alternatives. The selection of this particular model was based on its optimal trade-off between temporal efficiency and modelling precision. Accordingly, the subsequent section of this paper is dedicated to exploring the application of this model and its further validation.

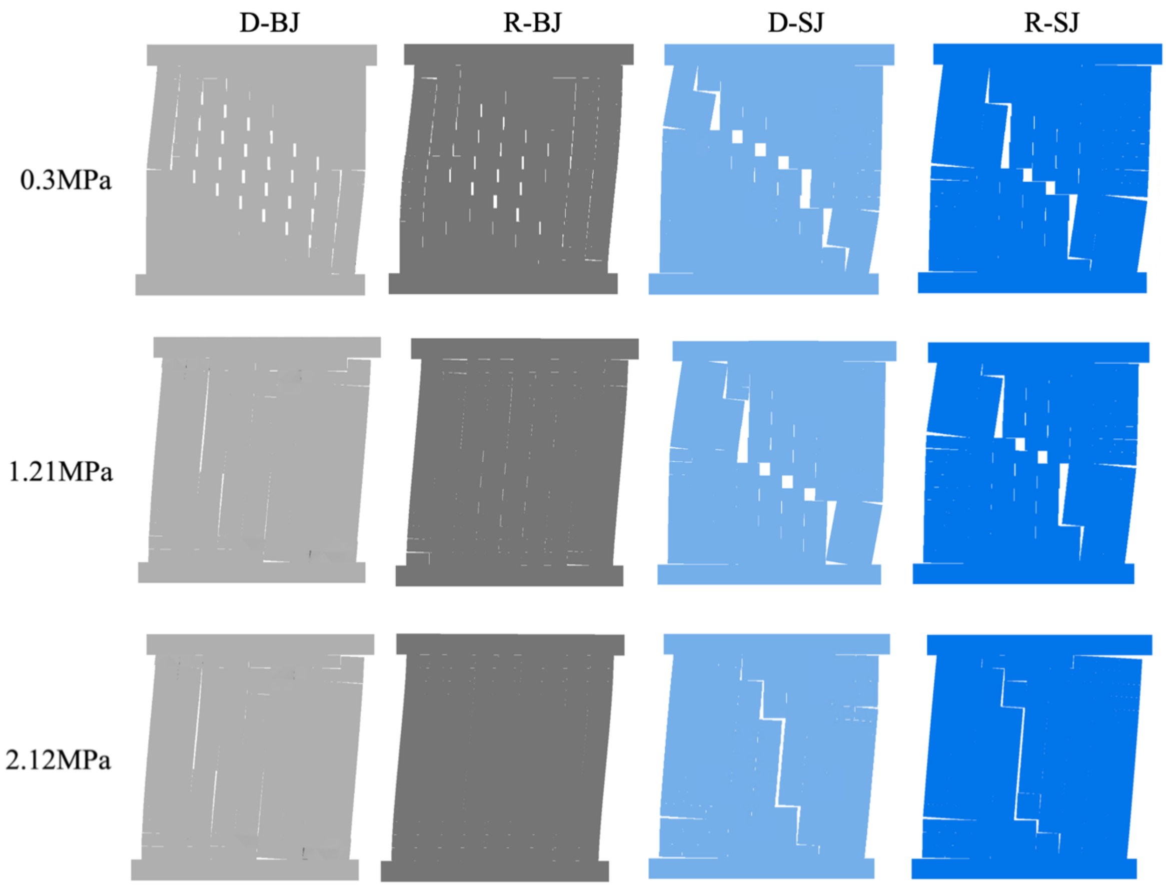

Figure 2.8. Damage pattern for all models subjected to three pre-compression conditions

2.4 Validation: IP monotonic response of small-scale URM walls

This section presents the validation of our novel DEM macro-models through comparison with experimental results of small-scale URM samples available in the existing literature. The purpose of this validation is to assess the capability of our models in accurately simulating the IP behaviour observed during real-world testing. The validation process involved two types of small-scale URM samples: a wall with an opening at the center (referred to as the opening wall) and a complete wall with no opening (referred to as the solid wall). The two 1x1x0.1 m walls subjected to quasi-static monotonic load were tested by Vermeltfoort et al. (1993) utilizing identical materials and boundary conditions.

2.4.1 Solid wall

The first small-scale specimen that has been validated was the solid wall (SW) and its experimental setups and material properties were introduced in **section 2.3** (see **Figure 2.5** and **Table 2.1** respectively). Then, the macro-modelling results for SW are compared with their micro- and experimental counterparts under different vertical pre-compression conditions (0.30, 1.21, and 2.21 MPa). After implementing the DE macro-crack discretization method, the SW was divided into the assembly of eight rigid macro-blocks, as shown in **Figure 2.9** and between the macro-blocks, the softening joints properties were applied.

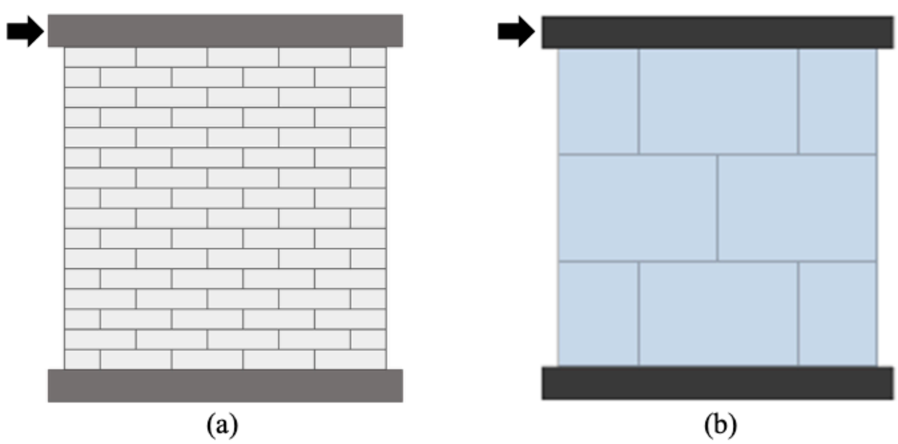

Figure 2.9. Micro and macro-model for DW

Figure 2.10 shows that the proposed DE macro-crack network model was able to capture the initial lateral stiffness and peak strength satisfactorily, albeit significantly overestimating ultimate displacement and residual strength capacities – better but not perfectly predicted by the micro-model. However, compared to the micro-model as well as the experiment results, the macro-model could not capture the sudden drop in lateral strength. This issue is currently being investigated, as mentioned by Lourenço: the sudden load drop is due to cracking in a single integration point of the potential cracks in a brick and the opening of each complete crack across one crack(Lourenço, 1996). Since the macro-model did not include the definition of the potential crack within the bricks, it is reasonable that the macro-model failed to show the sudden load drop as seen in the micro-model and the experimental prototype.

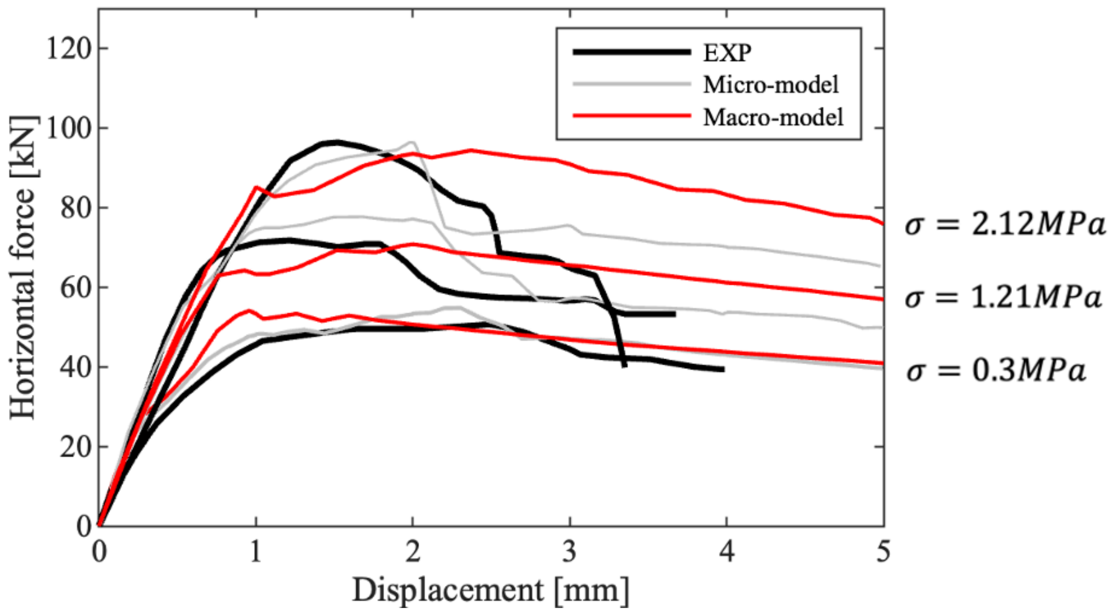

Figure 2.10. Force-displacement diagrams of the SW: macro vs. micro vs. experimental

Based on the analysis presented in Figure 2.11, it can be inferred that the damage patterns anticipated by the macro and micro models exhibit significant similarities, with both models revealing diagonal shear failure. In the context of high pre-compression conditions, it has been observed that the ultimate diagonal crack width is decreased in both macro and micro models.

In terms of computational efficiency, macro-model demonstrated a significant advantage over the micro-model. The macro-model was able to produce the entire force-displacement curve for low, moderate, and high pre-compression conditions in a substantially shorter time frame, with respective durations of 40s, 35s, and 30s. In contrast, the micro-model required considerably more time, taking 15 mins, 11 mins, and 9 mins, respectively, to conduct the same analysis. This significant difference in computation time amounts to an approximately 20-fold increase in analysis time for the micro-model. Overall, these findings clearly demonstrate the superiority of the macro-model in terms of computational speed.

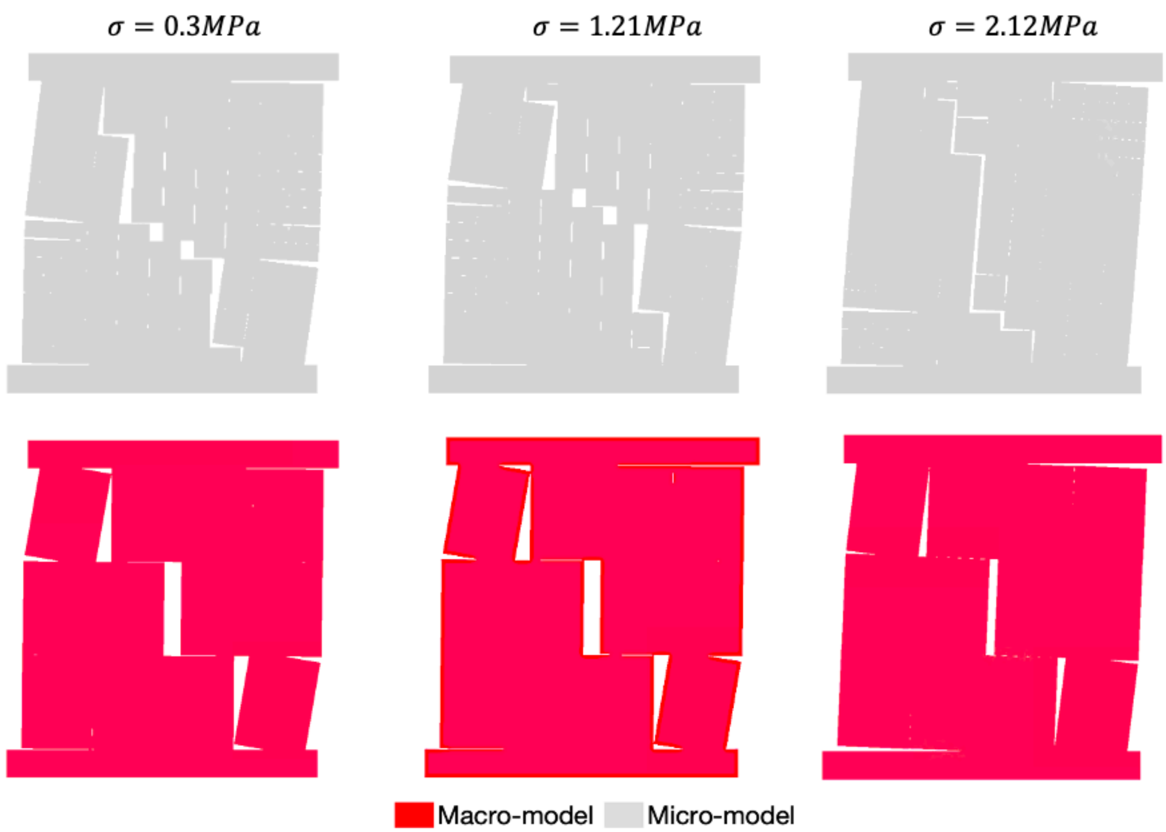

Figure 2.11. Damage pattern of the SW: macro vs. micro

2.4.2 Opening wall

Next, the opening wall (OW) experiment is analyzed with the same material and contact properties as given earlier. Before the horizontal loading, a vertical pressure (0.30 MPa) is applied to replicate the experimental setup. The central opening defines two small relatively weak piers and forces the compressive strut that develops under horizontal loading to spread around both sides of the opening. In the micro-model, the block arrangement remained exactly the same as the experimental specimen (see Figure 2.12a). While for the macro-model, because of the central opening of OW, the corresponding model was instead divided into eight rectangle elements (i.e. two piers, two spandrels, four nodes), and then further subdivided to obtain the macro-crack networks (see Figure 2.12b).

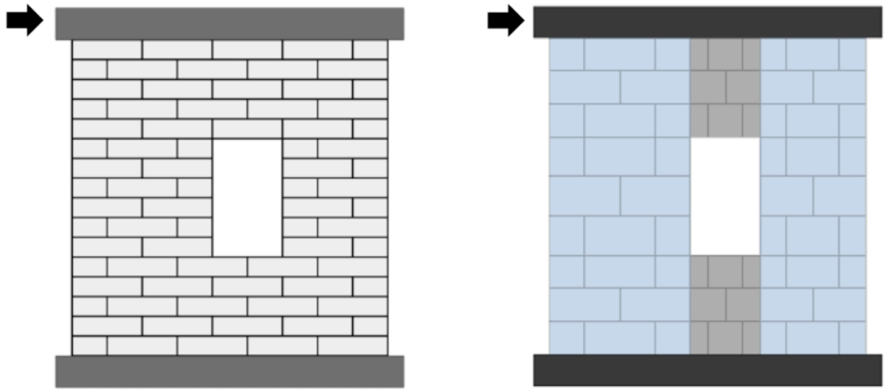

(a) (b)

Figure 2.12. Micro and macro-model for OW

As per the OW simulation, as shown in **Figure 2.13**, the macro-model predicted a similar force-displacement result to the micro-model, which mostly falls within the experimental envelope (in dark gray colour; multiple experimental tests on the same wall geometry were conducted). Once again, the main dissimilarities lie in the post-peak response, slightly underestimated by the macro-model but significantly different in the last displacement phases for the micro-model.

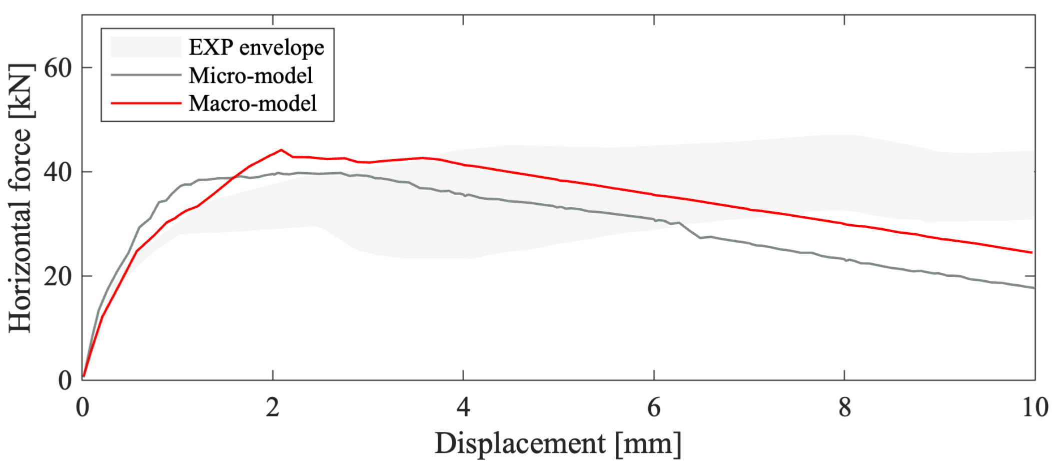

Figure 2.13. Force-displacement diagrams of the SW: macro vs. micro vs. experimental

The proposed macro-model has demonstrated the ability to accurately predict the failure mechanism observed in experimental results. This failure mechanism is characterized by stair-step cracks that initiate from the top and bottom of the opening and subsequently propagate toward the edges of the masonry walls. Moreover, compressed toes are present at the top and bottom of the wall as well as at the bottom and top of the small piers due to the rocking behaviour of the strut piers (see **Figure 2.14**c) were also captured by the macro-model. However, the configuration of the cracks in the macro-model is more concentrated in the spandrel than in the experimental and micro-model results (as evidenced by **Figure 2.14**a,b). This difference can be attributed to the variation in block arrangements in the macro-model, which affects the path of crack development.

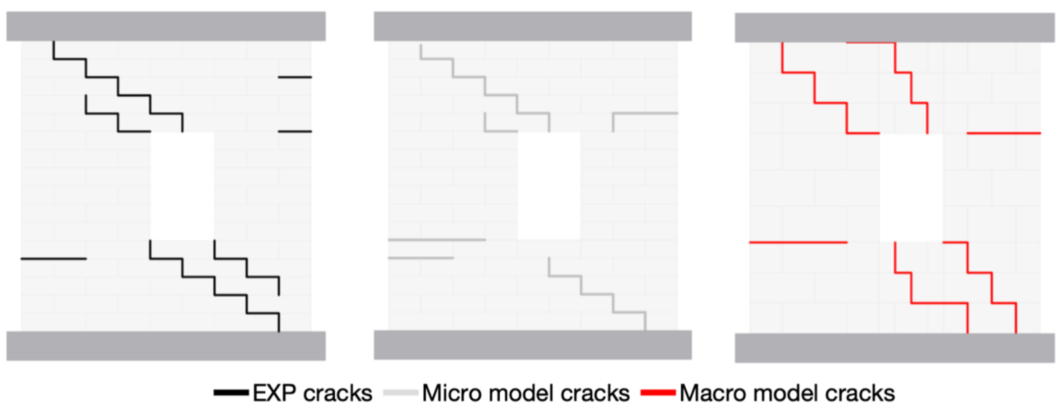

(a) (b) (c)

Figure 2.14. Damage pattern of the SW: macro vs. micro vs. experimental

2.4.3 Parametric analysis

After validation of two small-scale URM walls using the DE macro-crack model, the numerical results indicate that the model is able to capture the force-displacement curve and damage pattern within an acceptable range. However, there still are deviations from experimental results due to the model's inability to accurately estimate the highly non-uniform material characteristics and actual mechanical behaviours of URM structures.

Therefore, a parametric analysis is herein presented to explore the influence of mechanical properties of the numerical model to represent the actual behaviour of URM structures. The main variables of the parametric analysis are compressive strength (f_c) and compressive fracture energy (G_c) as the compressive properties are considered to be representative of any masonry type (Leite et al., 2012). To test the compressive properties dependency of the results, various values of f_c and G_c proportional to the original value (80%, 60%, and 40%) are used in the SW model that is subjected to high pre-compression of 2.12 MPa.

The results, as illustrated in **Figure 2.15**a, demonstrate a significant reduction in the initial stiffness and peak shear force of the shear walls as f_c decreases, while maintaining a consistent level of ductility. In addition, a tendency towards overall rocking failure is observed as f_c decreases. In contrast, reducing G_c leads to lower ductility in the shear wall, with only a negligible decrease (less than 10%) in the peak shear force (see **Figure 2.15**b). Furthermore, the damage pattern indicates that similar collapse mechanisms are obtained for varying G_c values.

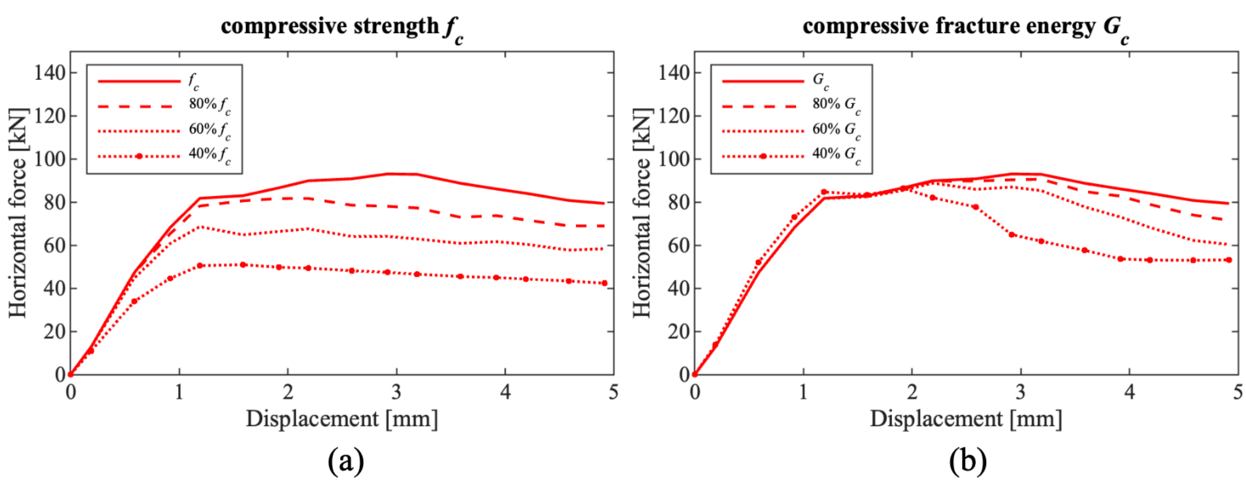

Figure 2.15. Parametric analysis of (a) compressive strength; (b) compressive fracture energy

2.5 Validation: IP monotonic response of a URM pier-spandrel system

In URM buildings, piers and spandrels constitute the predominant components, with piers serving as the primary load-bearing elements, supporting vertical loads and resisting horizontal actions. Spandrels, on the other hand, influence the behaviour of piers by modulating their boundary conditions, lateral capacity, and crack propagation (Lagomarsino et al., 2013). During seismic events, spandrels typically experience the heaviest damage, especially if local OOP failure does not occur and walls are predominantly subjected to IP lateral loads (Augenti & Parisi, 2010). This behaviour underscores the importance of spandrels in the global seismic response of URM buildings, as they effectively couple with piers. Therefore, before embarking on full-scale URM building validation work, it is essential to first evaluate the proposed DE macro modelling approach by examining the in-plane modelling accuracy of the spandrel-piers coupling system, which is the most critical structural component.

This section presents the validation of a pier-spandrel system (see **Figure 2.16**a) utilizing the proposed DE macro-crack network in comparison with a previously published experimental study by Augenti et al., 2011. The studied pier-spandrel system consisted of a tuff stone masonry wall with a central opening of 1.70 meters width, supported by two equal piers with a width of 1.70 meters, and a spandrel with a height of 1 meter. The masonry above the opening was supported by a timber lintel, resulting in a specimen with an overall length and height of 5.10 meters and 3.62 meters, respectively, and a thickness of 0.31 meters. Two reinforced concrete beams were placed on top of each pier to apply vertical pressure while IP lateral loading was monotonically applied to the specimen using displacement control through a servo-hydraulic actuator.

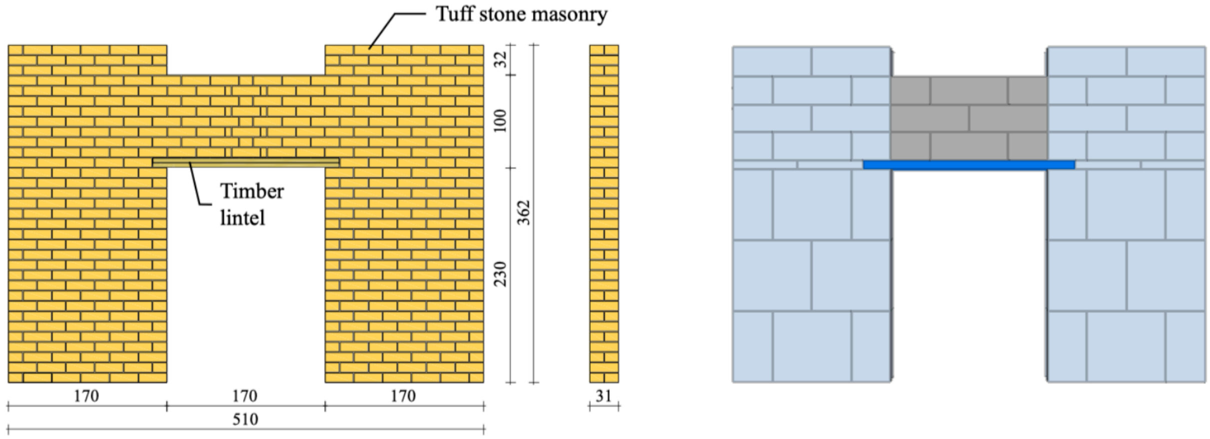

(a) (b)

Figure 2.16. (a) Experimental (Pulatsu et al., 2022) and (b) numerical configurations of the pier-spandrel system

The present study describes the numerical model development of a proposed pier-spandrel wall using the DE macro-crack discretization method with discrete rigid blocks. Finally, the wall configuration was divided into 5 elements and 51 blocks (see **Figure 2.16**b). It should be noted that, for the sake of simplicity, the timber lintel was simulated as rigid, although may potentially underestimate the effect of flexural and shear deformations of the lintel on the overall system response. The linear and non-linear strength parameters of the model are provided in **Table 2.2**, based on the values suggested by (Pulatsu et al., 2022). Also, the model incorporated brick properties to simulate the block interlocking at the connection between the pier and the spandrel. The loading conditions applied in the model include gravity loads corresponding to 200 kN per pier, as indicated in **Figure 2.16**b. Furthermore, lateral pushover loading was applied on a rigid 2D plate fixed on the top right side of the left pier at relatively low displacement rates.

Table 2.2. Selected elastic and inelastic mechanical properties for the pier-spandrel system

material ID	E_m	G_m	f_c	f_t	c	ϕ	G_c	G_f^I	G_f^{II}
	[MPa]	[MPa]	[MPa]	[MPa]	[MPa]	[°]	[N/m]	[N/m]	[N/m]
masonry	2070	828*	3.96	0.15	0.15	14.6	12800*	4.3*	125*
bricks	2070	828*	3.96	0.23*	0.46*	35*	12800*	8*	550*

** Test values are missing*

The damage patterns of the experimental and numerical model are presented in **Figure 2.17** which are attributed to the maximum displacement of the top reinforced concrete beam (approximately 30mm). The diagonal crack observed at the spandrel during the experiment, which was the dominant failure mechanism, was successfully replicated in the numerical model. However, the numerical model exhibited additional cracks around the left end of the lintel on the left pier that was not observed during the experiment. This disparity could due to the rigid lintel's reverse leverage force on the left pier when both piers tilt under lateral force.

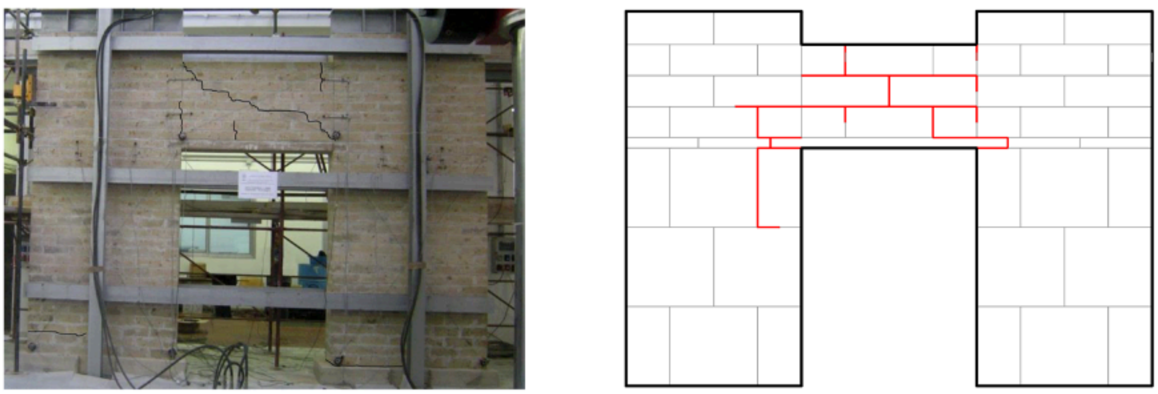

Figure 2.17. Experiment (Augenti et al., 2011) vs. numerical: damage pattern of the pier-spandrel system

Further, in **Figure 2.18**, the force-displacement curve of the numerical model shows a good agreement with the experiment curve in terms of the initial stiffness and the peak base shear.

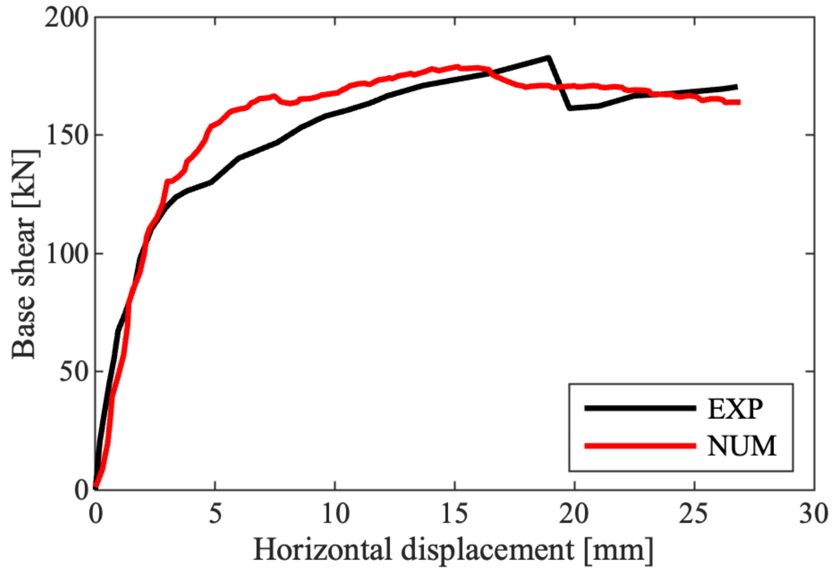

Figure 2.18. Experiment vs. numerical: the force-displacement curve of the pier-spandrel system

2.6 Validation: IP cyclic response of a full-scale URM building

In this section, the proposed strategy for modelling the quasi-static in-plane cyclic behaviour of a full-scale two-storey URM facade with regular opening layouts (see **Figure 2.19**a), which was tested at the University of Pavia, is presented and validated (Magenes et al. (1995). The specimen subjected to testing featured non-symmetric openings and had a total wall height of 6.4 m, with a wall thickness of 0.25 m. Its plan view dimensions measured 6 m × 4 m and were arranged in English bond patterns. Notably, the door wall (wall D) did not connect to the transverse walls A and C, while the window wall (wall B) connected to the adjacent walls through an interlocking brick pattern at the corners. Hence, the practical test setup consisted of two individual shear walls (the door and window walls) with no coupling effect due to a non-interlocking brick pattern. The floors were constructed using a series of isolated steel beams with a section depth of 140 mm, designed to simulate a highly flexible diaphragm. Both vertical and horizontal loads were applied through the floor beams, while concrete blocks were used to simulate gravity loads, resulting in a total added vertical load of 248.4 kN on the first floor and 236. kN on the second floor, approximately equivalent to a distributed load of 10 kN/m per floor. During the experiment, four concentrated horizontal forces were applied at the floor levels of the two longitudinal walls to simulate seismic forces (see **Figure 2.19**a). Moreover, **Figure 2.19**b presents the displacement histories of the top floor for both the door wall and the window wall, as obtained from the experimental data. Then, the proposed DE macro network is herein extended to the building scale.

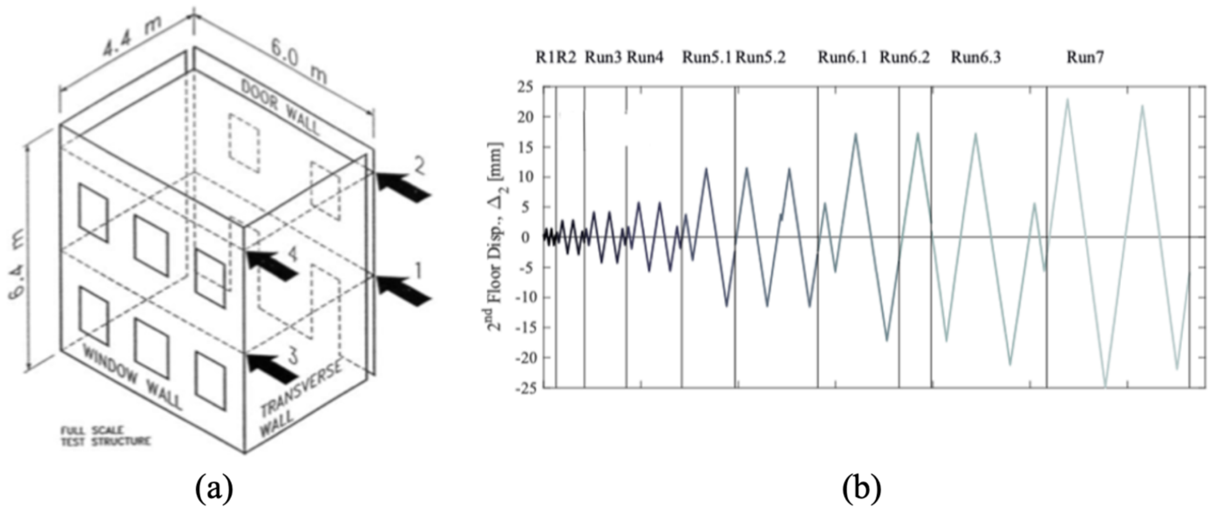

Figure 2.19. (a) Experimental configuration and loading locations; (b) 2nd-floor experimental displacement history (Magenes et al. 1995)

Figure 2.20a illustrates the door wall, which is composed of a total of 16 primary elements and subdivided into 144 rigid macro-blocks. Moreover, the masonry lintels have been idealized as rigid blocks, highlighted in dark blue while the steel beams were modelled as rigid solid elements of reduced thickness ("beam plates" hereinafter) fixed to the façade, to which vertical loads and the horizontal loads were applied to simulate the distributed gravity loads and the pushover loads respectively, indicated in red. The contact properties of the proposed DE macro-crack networks used to simulate these specimens are summarized in **Table 2.3**. It is important to note that it is difficult to calculate the contact stiffness of each masonry joint due to the high variability of the block sizes caused by the discretization method. Thus, the joint stiffnesses in the numerical model were estimated from the provided Young's modulus of 2400 MPa, and the average horizontal spacing of 0.6m. Depending on the availability of the experimental data, some parameters are taken from experimental results, whereas other parameters are estimated, considering (DeJong et al., 2009; Lourenço, 2009). The contact properties are given in **Table 2.3**. Notably, the interlocking over-strength is simulated by utilizing the bricks properties of **Table 2.3**, with provisions carried over from Section **2.2**, as illustrated in the joints between the grey and light blue elements in **Figure 2.20**a.

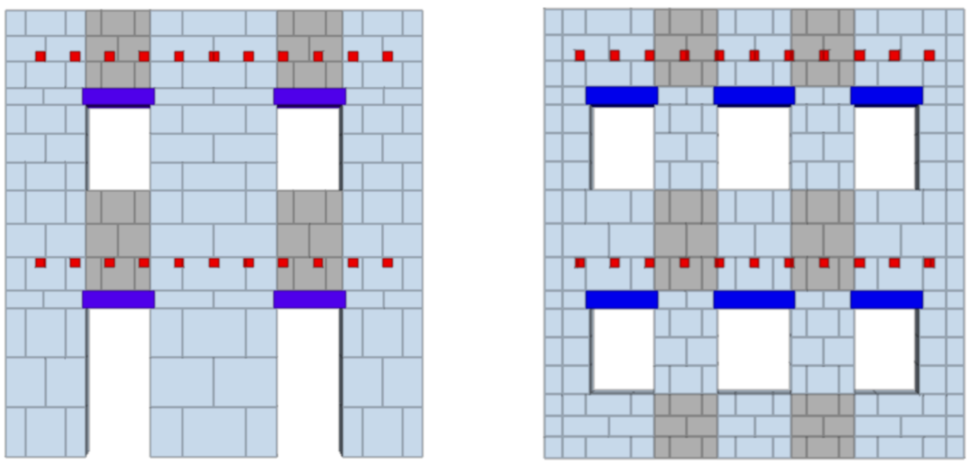

(a) (b)

Figure 2.20. Numerical configuration of (a) door wall and (b) window wall

In relation to the building's response to IP loads, the window wall is considered an IP/OOP complex system as it is comprised of the two pre-existing longitudinal walls, referred to as wall A and wall C, which contribute as the out-of-plane (OOP) components. As this section exclusively focuses on the IP behaviour of the unreinforced masonry (URM) façade, the analysis isolated wall B, which is the transversal wall with openings, from the window wall system (The IP/OOP issue will be discussed in **section 2.8**). The mechanical properties of the masonry component were derived from **Table 2.3**. Adopting the same discretization approach as the door wall, the window wall was divided into 19 elements, which are further subdivided into 216 rigid macro-blocks.

Table 2.3. Selected elastic and inelastic mechanical properties for the full-scale URM building

material ID	E_m	G_m	f_c	f_t	c	ϕ	G_c	G_f^I	G_f^{II}
	[MPa]	[MPa]	[MPa]	[MPa]	[MPa]	[°]	[N/m]	[N/m]	[N/m]
masonry	2400	960*	6.2	0.05	0.075	30	10000*	5*	20*
bricks	2400	960*	15	1*	1.5*	35*	20640*	80*	125*

** Test values are missing*

Figure 2.21 presents the results of the cyclic test conducted on the door wall. The figure compares the predicted hysteretic response and corresponding damage propagation of selected test phases (test 4, test 5, test 6, and test 7) with their experimental counterparts. The numerical model accurately predicted the crack propagation and overlapping hysteretic curves with experimental records after test 4. Specifically, the numerical model accurately predicted cracks appearing on the spandrel and around the lintels (see **Figure 2.21**a). Subsequently, as shown in **Figure 2.21**b, after test 5, diagonal cracks in the central squat pier dominated the failure mechanism, while cracks in the first-floor spandrels increased their width, and new cracks were generated on the two outside piers on the first floor. The numerical model also predicted similar behaviour and similar energy dissipation, albeit with a slight overestimation of the shear force in the negative direction as well as the damage on the two outside piers and the damage on the second floor. Upon the completion of test 6, it was observed that the diagonal cracks propagated symmetrically on the exterior piers of the slender wall, starting from the bottom outside corner and progressing toward the top inside corner (see **Figure 2.21**c). Following the seventh test, the cracks were found to have developed entirely throughout the façade, with the exception of the cracks in the slender pier on the second floor, which were not experimentally detected (see **Figure 2.21**d). Notably, both the cracking pattern and hysteretic curve demonstrated favourable consistency with the test outcome. Moreover, when comparing the running time of this macro-model with those obtained using a DEM micro-model by (Malomo & DeJong, 2021a), the analysis time was reduced by 4800%.

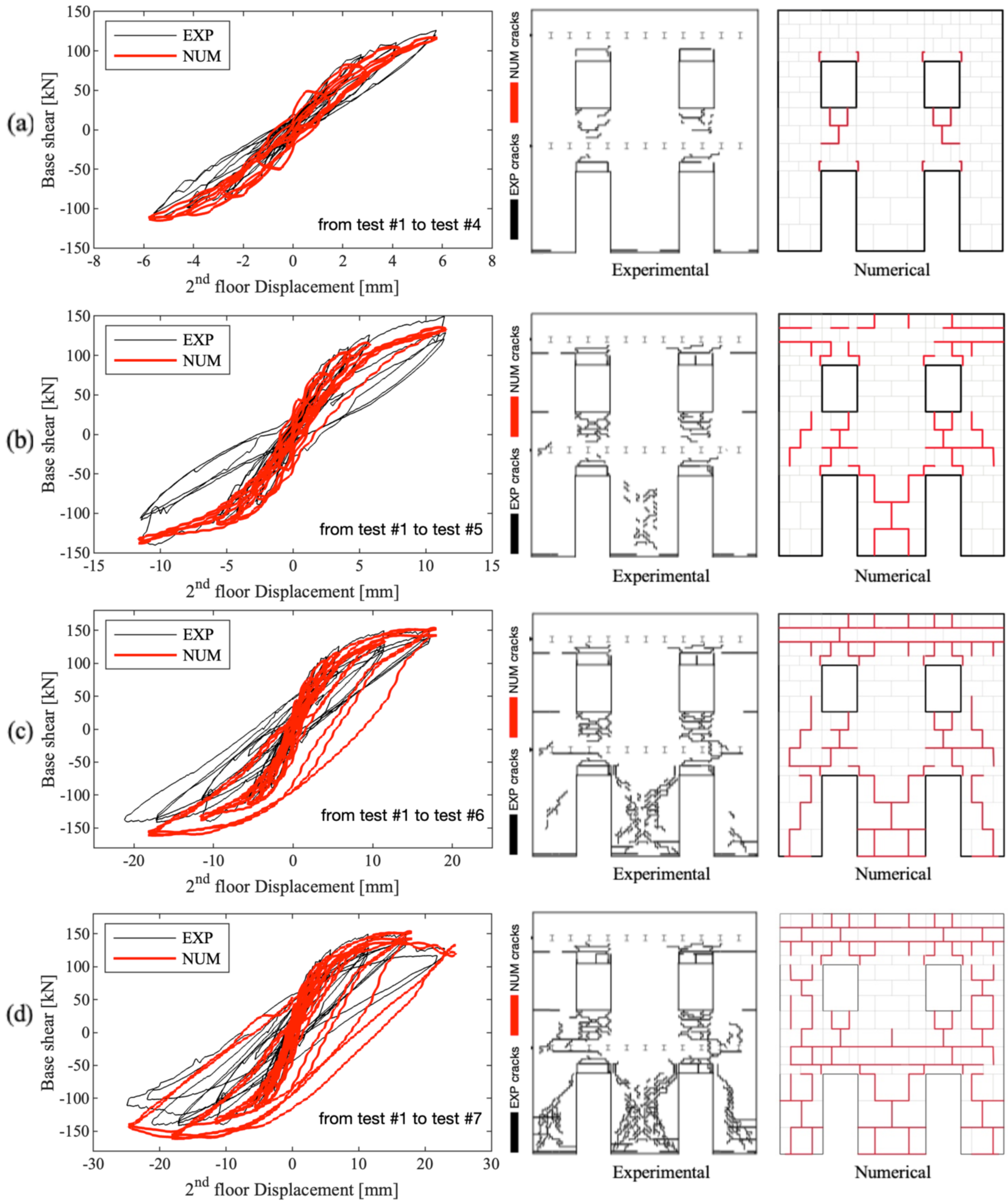

Figure 2.21. Experimental (Magenes et al. (1995) vs numerical force-displacement hysteretic response and damage pattern for selected phases of the door wall (a) phase 4; (b) phase 5; (c) phase 6; (d) phase 7

The proposed comparison regimen was also implemented on the window wall, and the predicted hysteretic response and damage propagation of tests 2, 5, and 7 were compared with experimental results (see **Figure 2.22**). In the numerical model, the first crack was observed on the spandrel between openings, similar to the door wall, but this occurred earlier after test 2 when the door wall showed no damage (see **Figure 2.22**a). However, in the experiment, the initial cracks were concentrated outside while they were more apparent at the center in the numerical model. In test 5, although the actual damage at the second-floor central pier was overestimated, the shear cracks observed experimentally on the first-floor central piers towards the two bottom outside corners were accurately captured numerically. Additionally, there was a low level of energy dissipation in the negative loading direction in the numerical model indicated in **Figure 2.22**b. Finally, after test 7, the cracks on the central piers on both floors increased their width as the wall reached its shear force capacity. Although there still was an underestimation of energy dissipation in the negative direction, the hysteretic curve demonstrated good agreement with the test results (see **Figure 2.22**c).

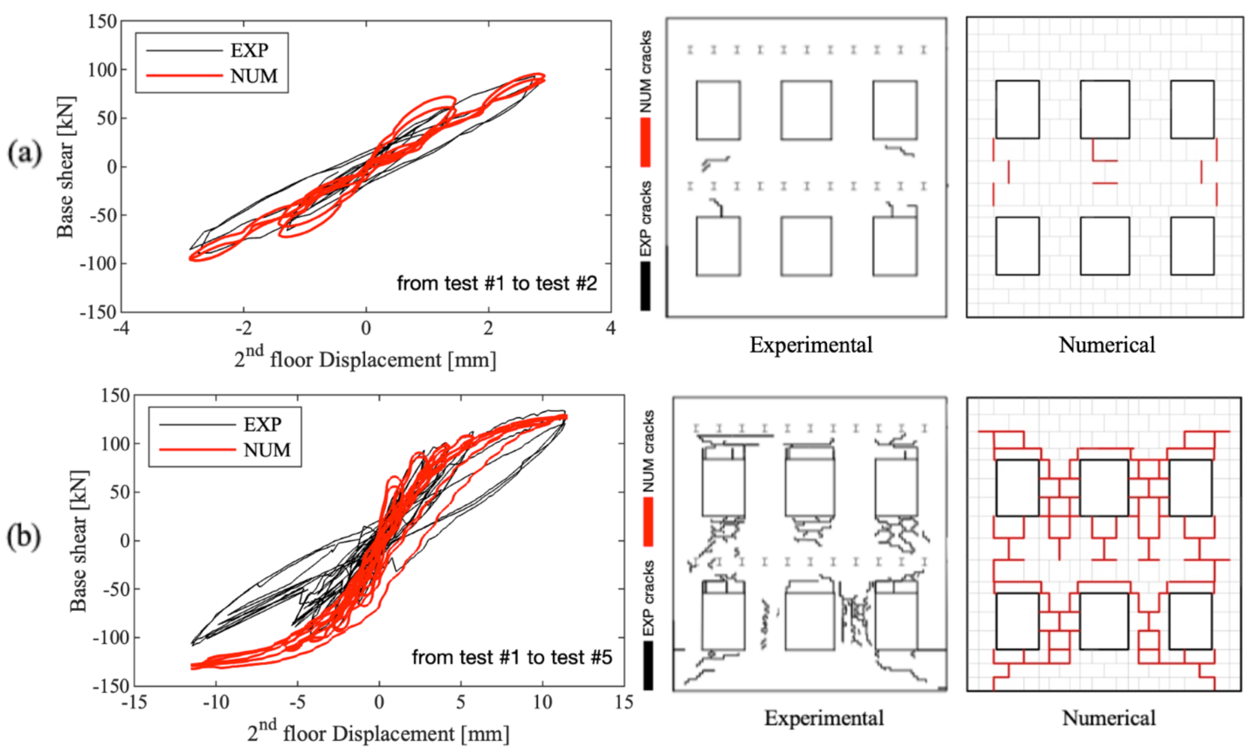

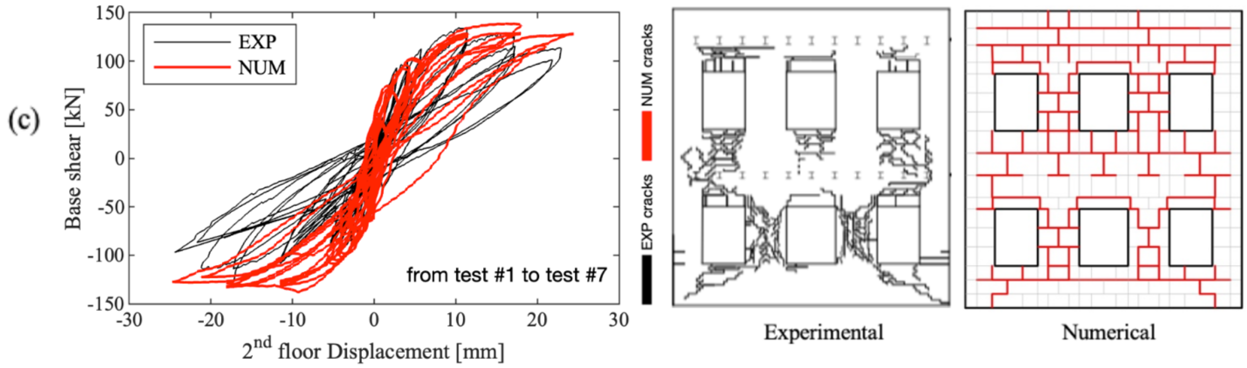

Figure 2.22. Experimental (Magenes et al. (1995) vs numerical force-displacement hysteretic response and damage pattern for selected phases of the window wall (a) phase 2; (b) phase 5; (c) phase 7

The overall numerical predictions of two independent walls, namely the door wall and window wall, are compared with their experimental counterparts. The comparison is based on the plots of base shear versus roof displacements and corresponding cyclic envelopes, as presented in **Figure 2.23**. The results show a good agreement between the computational models and the experimental findings, especially in terms of the initial stiffness and maximum capacity. The door wall and window wall achieved maximum base shear values of approximately 150 kN and 140 kN, respectively (see **Figure 2.23**). The numerical model also predicts that both walls will experience a simultaneous force drop after test 6, once the base shear reaches its maximum value. However, the experimental results indicate an asymmetrical response that has a slightly lower capacity in the negative loading direction, about 7% lower than in the positive loading direction, which was not observed in the numerical model. As previously indicated, the hysteretic response of the door and window walls reveals an underestimation of energy dissipation efficiency in the negative loading direction for both walls (see **Figure 2.21** and **Figure 2.22**). The present observation elucidates a feasible justification concerning the heterogeneous mechanical characteristics of the experimental specimen, attributable to the fabrication process and the workmanship (Lourenço, 2002), consequently leading to an asymmetrical response in the experimental outcome. By contrast, the numerical model employed in this study features uniform material properties and block composition throughout, thus implying a nearly symmetric response.

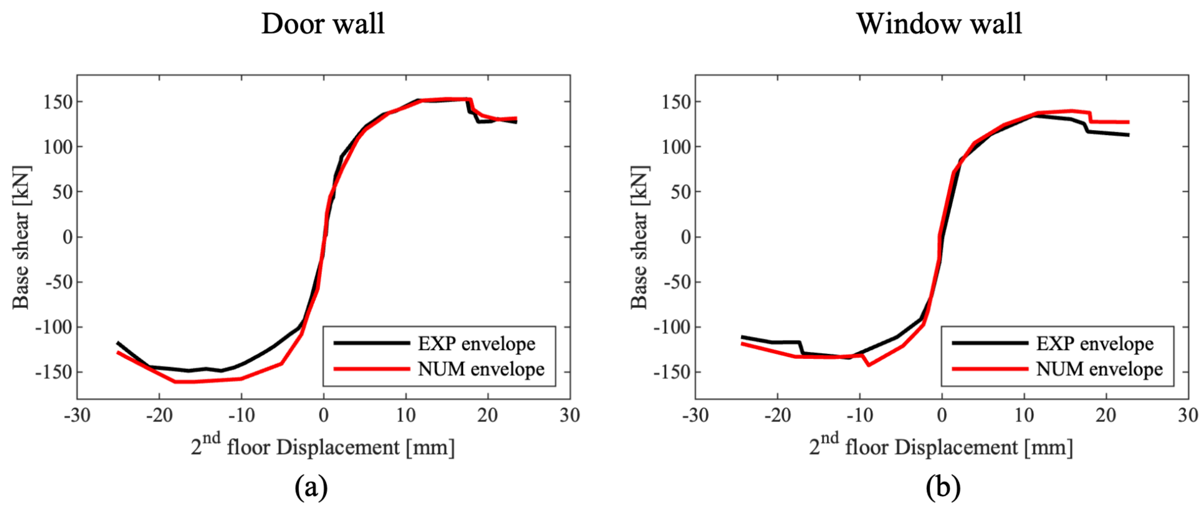

Figure 2.23. Comparison between the experimental and numerical envelope of (a) door wall and (b) window wall

Additionally, in the following sections, pushover analyses will be conducted on large-scale URM buildings to access the influence of the opening layouts on the modelling accuracy. Thus, the same macro-models of door wall and window wall are employed to perform monotonic pushover analysis, and the ensuing results are compared with the corresponding cyclic envelopes for both experimental and macro-model results.

As illustrated in **Figure 2.24**, similar damage patterns, initial lateral stiffness, and peak base shear were obtained in both the door wall and the window wall under monotonic pushover load, relative to the cyclic envelope of the experimental model and the same macro-model. Nevertheless, a comparison of the force-displacement curves indicates that pushover loading may not precisely depict the force level and the force drop, as cyclic loading does, despite the usage of the same macro-model. This discrepancy is attributable to the fact that pushover loading may not reflect the accumulation of damage and the consequent reduction in stiffness under cyclic loading.

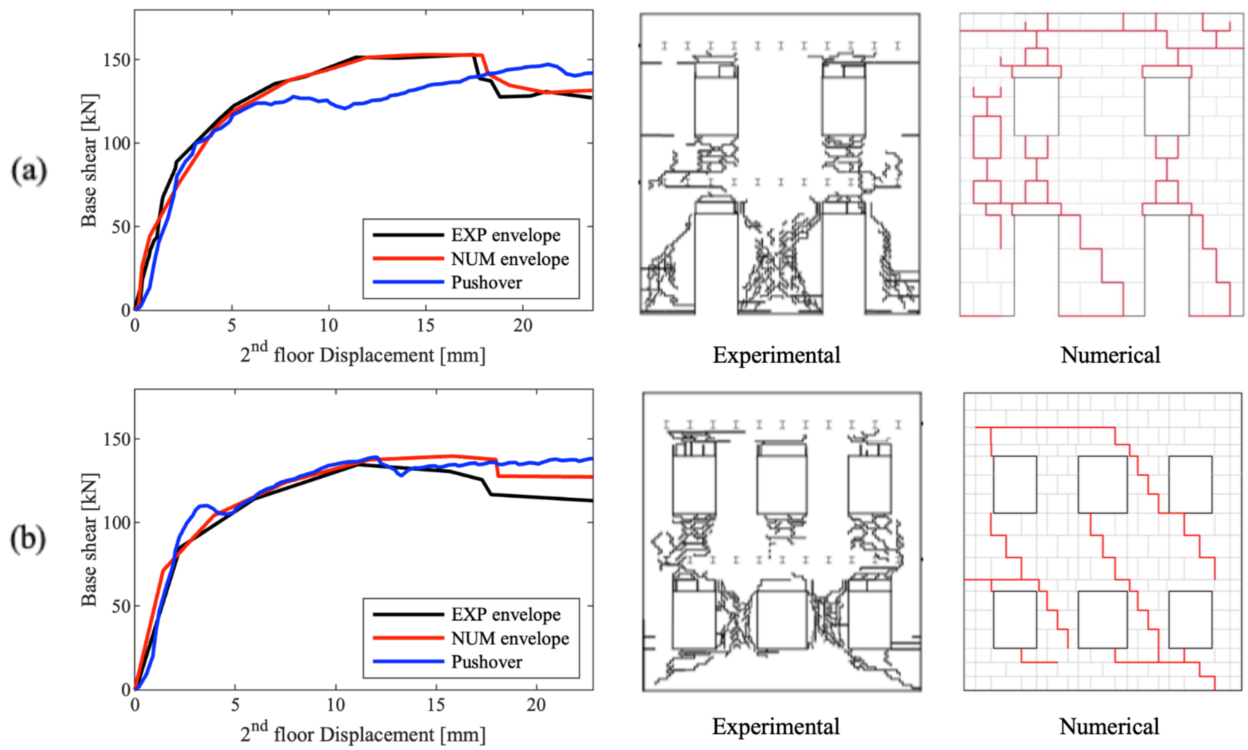

Figure 2.24. Pushover force-displacement curves and damage patterns of (a) door wall and (b)window wall (Magenes et al. (1995)

2.7 Simulation of URM façades with irregular opening layouts

As for the previous sections, the validations were only conducted on the URM specimens with regular openings. However, in the presence of irregular opening layouts, the identification of the effective height/ length of URM members becomes non-unique and may lead to epistemic modelling errors (Berti et al., 2017), resulting in a significant dependency of predicted results on the considered discretization scheme (Quagliarini et al., 2017). With the view to further evaluating the adequacy of the proposed model, the capability of the DE macro-crack network in modelling the façades with irregular opening layouts is presented in this section.

To access the modelling accuracy of the proposed modelling strategy when considering the irregular opening layouts, four clay brick two-storey facades of different opening arrangements were selected according to Parisi & Augenti, 2013. The modifications were made to the original door wall presented in **section 2.6,** specifically pertaining to the relocation and removal of door and window openings (see **Figure 2.25**a). The first facade underwent alterations with the substitution of the lower right door opening with a window opening that matched the size of the second-floor window. In the second facade, the door opening was completely eliminated. The third facade saw the removal of the window opening situated on the right of the second floor. The fourth facade saw a horizontal shift in the window openings to the right, resulting in a vertical misalignment with the door openings on the first floor. The material properties of the four walls with irregular openings are all adopted values from **Table 2.3**. After the implementation of the DE macro-crack network, the numerical models of the four irregular opening façades are shown in **Figure 2.25**b.

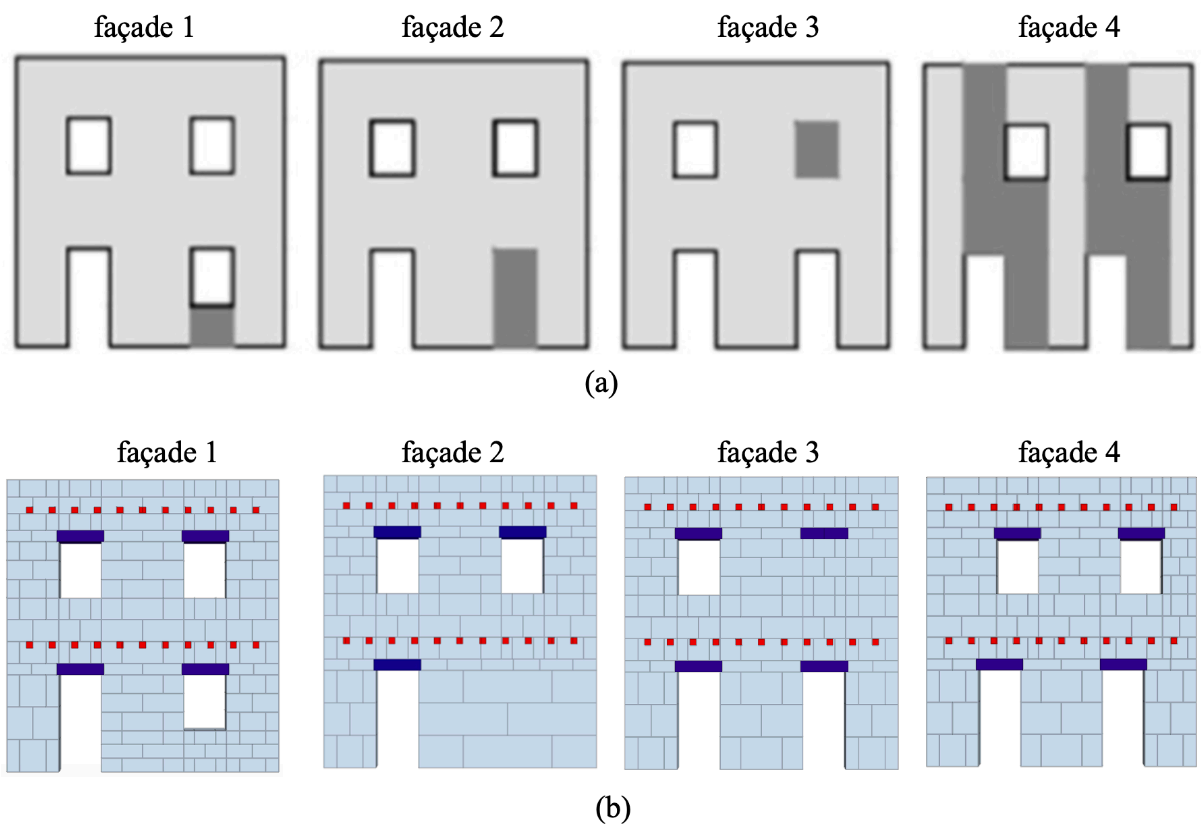

Figure 2.25. (a) Selected façade layouts (Morandini et al., 2022); (b) Numerical models using DE macro-crack discretization method

Different from the cyclic test made in section **2.6**, to reduce the potential computation cost and easier for demonstration, monotonic pushover analysis in displacement control was performed in both directions with the four numerical models. Their results were then compared to the DEM micro-models created explicitly representing actual brick size and bond pattern of experimental façades (Morandini et al., 2022). Due to time constraints, the micro-model analysis of façade 4 was not conducted in the referenced paper, and the result of an Equivalent Frame Method (EFM) analysis (presented in the same paper) is taken as a reference instead.

Figure 2.26 compares the results obtained from the macro-models using the DE macro-crack discretization method with their corresponding micro-model in terms of initial lateral stiffness (ILS_n) and peak base shear (V_{bp}), where the ILS_n was computed considering the inclination of the line connecting the points that correspond to the 15% and the 30% of the V_{bp} (Morandini et al., 2022). The force-displacement results of the micro and macro models are found in good agreement in both loading directions for all four configurations (see **Figure 2.26**a), with a difference under 8% and 10% for ILS_n (see **Figure 2.26**b) and V_{bp} (see **Figure 2.26**c) respectively. In comparing the results of the negative and positive loading directions of the four configurations, it was observed that all the configurations (configurations 1, 3, 4) manifested similar magnitudes in terms of ILS_n and V_{bp} in both loading directions, except for configuration 2 where both values were approximately 20% higher during positive loading. This finding is attributable to the additional rigidity in the positive loading direction resulting from the squat pier, which was present due to the absence of the window opening, consequently contributing to greater base shear as a result of the reduced potential for lateral deformation.

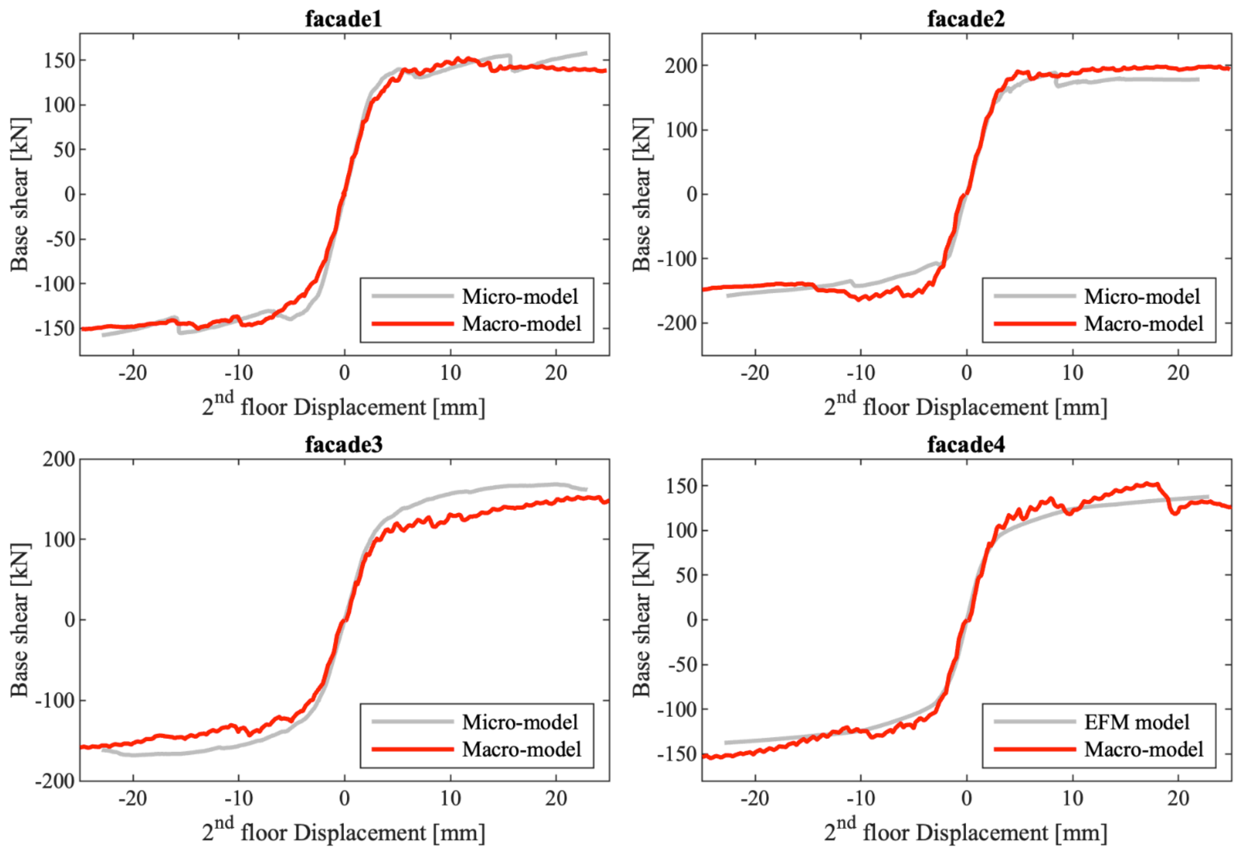
facade1
facade2
facade3
facade4
Base shear [kN]
2nd floor Displacement [mm]
Micro-model
Macro-model
EFM model
150
100
50
0
-50
-100
-150
200
-200
-20
-10
10
20
(a)

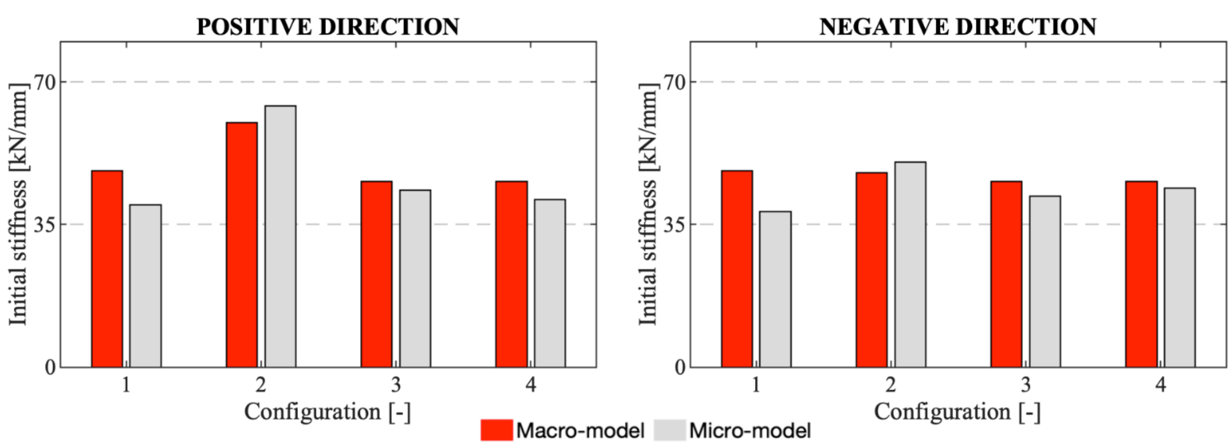
POSITIVE DIRECTION
NEGATIVE DIRECTION
Initial stiffness [kN/mm]
Configuration [-]
70
35
0
1
2
3
4
Macro-model
Micro-model
(b)

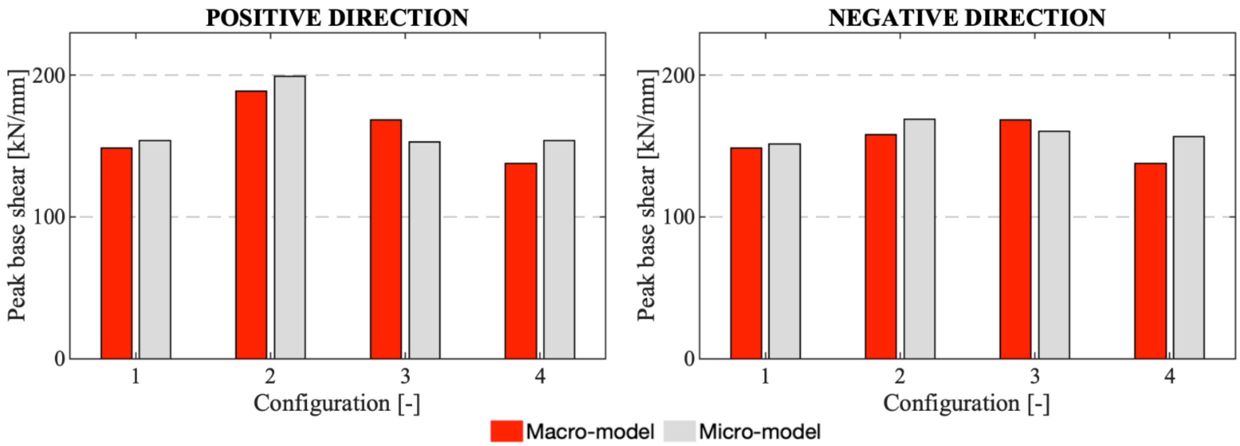

(c)

Figure 2.26. Macro vs. micro (a) force-displacement curves, (b) initial stiffness and (c) peak base shear

When comparing the damage patterns of macro-modelling predictions with those inferred using traditional micro-models (see **Figure 2.27**), a notable degree of consistency in the predicted failure mechanism was observed. Nonetheless, some minor differences were observed due to the existence of irregularities. In configuration 1, the negative loading on the macro-model resulted in the emergence of diagonal shear cracks at the slender pier and the central squat pier, which were not detected in the micro-model. Similarly, in configuration 2, the macro-model exhibited an additional diagonal crack on the slender pier under negative loading, which was not apparent in the micro-model. These variations could potentially be attributed to the larger block size employed in the macro-model, in contrast to the original brick size adopted in the micro-model.

Moreover, it is noteworthy to mention that the macro-model demonstrated a significantly lower computational cost compared to its micro-model counterpart, with a speed-up factor of approximately 50 times, while ensuring a high level of modelling accuracy.

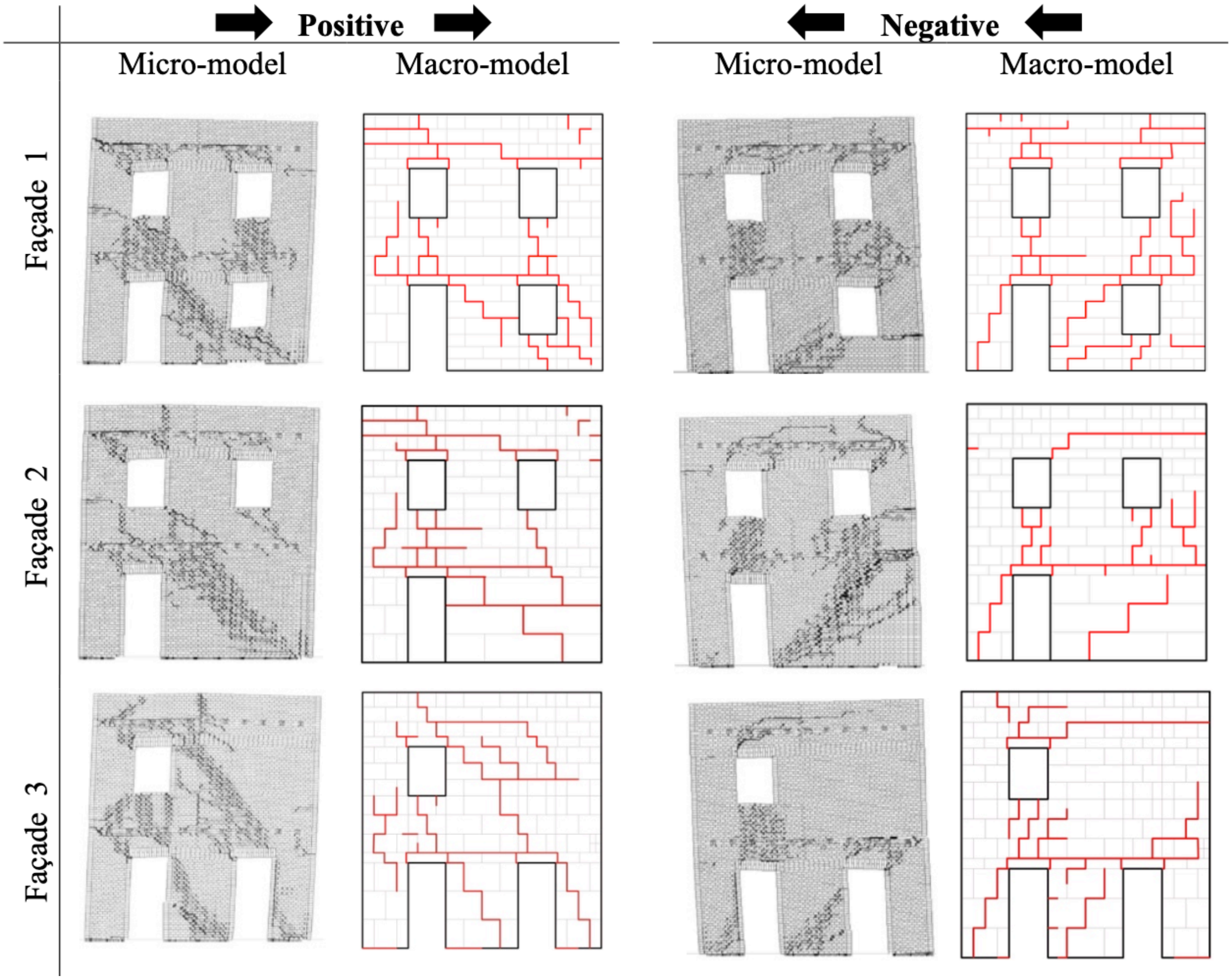

Figure 2.27. Micro (Morandini et al., 2022) vs. macro damage pattern under positive and negative loading directions

2.8 Validation: IP/OOP dynamic response of a full-scale U-shaped URM house

In the preceding section, the efficacy of the proposed DE macro-crack network in representing the IP behaviour of masonry structures was tested and verified, ranging from small-scale URM specimens to pier-spandrel components and full-scale URM buildings with both regular and irregular opening layouts. However, the modelling was restricted to a single transversal wall without OOP coupling effects with adjacent longitudinal walls. While this constraint reduces the computational cost of numerical analysis, it can lead to imprecise estimations of the global response of URM structures during earthquakes due to the neglect of OOP effects and mechanical interaction among elements under both IP and OOP combined actions. Previous experimental tests (Costa et al., 2013; Tomassetti et al., 2019) have nonetheless shown that OOP failures might preclude the full exploitation of the global capacity associated with the IP resistance of URM members, while post-earthquake damage observations (e.g., Brando et al., 2020; Leite et al., 2012) highlighted how the separation between orthogonal walls and ineffectiveness of façade-diaphragm connections might lead to the development of early collapse phenomena. In order to incorporate OOP failures in the analysis of structural response during earthquakes, several scholars have suggested efficient approaches involving the utilization of macroelements to simulate the structural behaviour of URM systems. The recent implementation of such techniques has demonstrated that the failure mechanisms associated with IP and OOP modes can be adequately replicated through numerical simulations. (Malomo & DeJong, 2021b; Pantò et al., 2017; Yi et al., 2006).

To further scrutinize the DE macro-crack network capabilities to model IP/OOP interaction, the proposed modelling strategy is applied in this section to the simulation of the dynamic response of a full-scale double-wythe clay brick U-shaped specimen tested at the LNEC laboratory (National Laboratory for Civil Engineering, Lisbon, Portugal) by Candeias et al., 2016 (see **Figure 2.28**a). The eastern central wall was characterized by a 0.5-m high triangular tympanum and by a 0.8 × 0.8-m opening located in the middle of the façade. The North return wall had an opening of 0.8 × 1.0 m. The South wall featured no openings. The lack of symmetry triggered different responses in the two lateral walls, influencing the final crack distribution and global failure mode, as further discussed below. The specimen was tested up to collapse on the shake table under a uniaxial ground motion component (approximately 27 seconds of duration) of the Christchurch (New Zealand) earthquake (February 21, 2011) that applied in the east-west direction (perpendicular to the central wall). This ground motion component is progressively scaled increasing the peak ground acceleration from 0.179g (TEST01) to 1.273g (TEST08), in eight distinct consecutive testing phases.

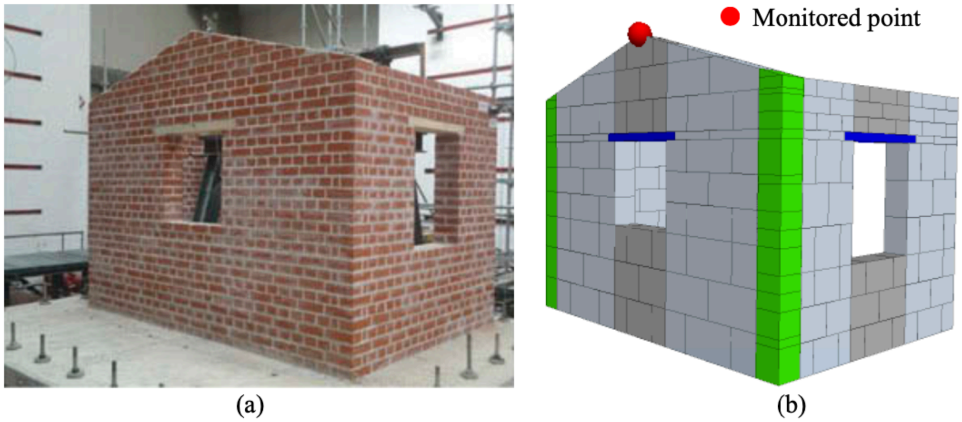

Figure 2.28. (a) Experiment setup (Candeias et al., 2017); (b) DE macro-crack idealization of the U-shaped URM wall

In the numerical model, the first simplification is to replace the real double-wythe structure with a single block across the wall thickness. Furthermore, in real-world URM structures, the connection between the transversal and longitudinal walls is normally characterized by complex interlocking patterns between units which can be explicitly reproduced using micro-modelling approaches (Chácara et al., 2017). To minimize computational efforts, in this work, corner rigid blocks are utilized to connect the transversal and two longitudinal walls at the same height as the horizontal interfaces on both sides of the corner. These blocks are depicted as green-coloured columns in **Figure 2.28**b and are akin to an example employed by (Malomo & DeJong, 2022a). The comprehensive linear and nonlinear material properties of the numerical model are summarized in **Table 2.4**. As highlighted in the previous section, the discretization method employed in the numerical model results in a high variability of block sizes, making it difficult to accurately estimate the joint stiffnesses of the U-shaped wall. Therefore, in the numerical model, the joint stiffnesses were estimated using the provided young's modulus of 5170 MPa and an average horizontal spacing of 0.5m. The masonry properties listed in **Table 2.4** were also utilized between the spandrels and the piers, consistent with previous investigations.

Table 2.4. Selected elastic and inelastic mechanical properties for the full-scale U-shaped wall

material ID	E_m	G_m	f_c	f_t	c	ϕ	G_c	G_f^I	G_f^{II}
	[MPa]	[MPa]	[MPa]	[MPa]	[MPa]	[°]	[N/m]	[N/m]	[N/m]
masonry	5170	2068*	25	0.1	0.2	35	23500*	8.1*	81*
bricks	5170	2068*	15	1*	2*	37*	20640*	40.6*	406*

** Test values are missing*

Prior to conducting the shake-table test outlined earlier, quasi-static monotonic analyses were carried out by applying uniform pressure at a relatively low velocity to the front façade, considering both pushing and pulling loads. The OOP displacement was monitored at the top of the tympanum, which was identified by a red dot in **Figure 2.28**b. The results were then compared to those obtained by other researchers using FEM (Chácara et al., who employed either a rotating or a fixed crack failure criterion) and DEM (Cannizzaro & Lourenço , who performed their analysis at either the micro or macro-scale and Malomo & DeJong, who used a new M-DEM discretization method), as depicted in **Figure 2.29**. The initial stiffness and peak base shear exhibited good agreement with the comparison results. Additionally, it is noteworthy that the base shear capacity during pushing loading was significantly greater than that observed during pulling loading, which was expected due to the additional resistance provided by the two longitudinal walls.

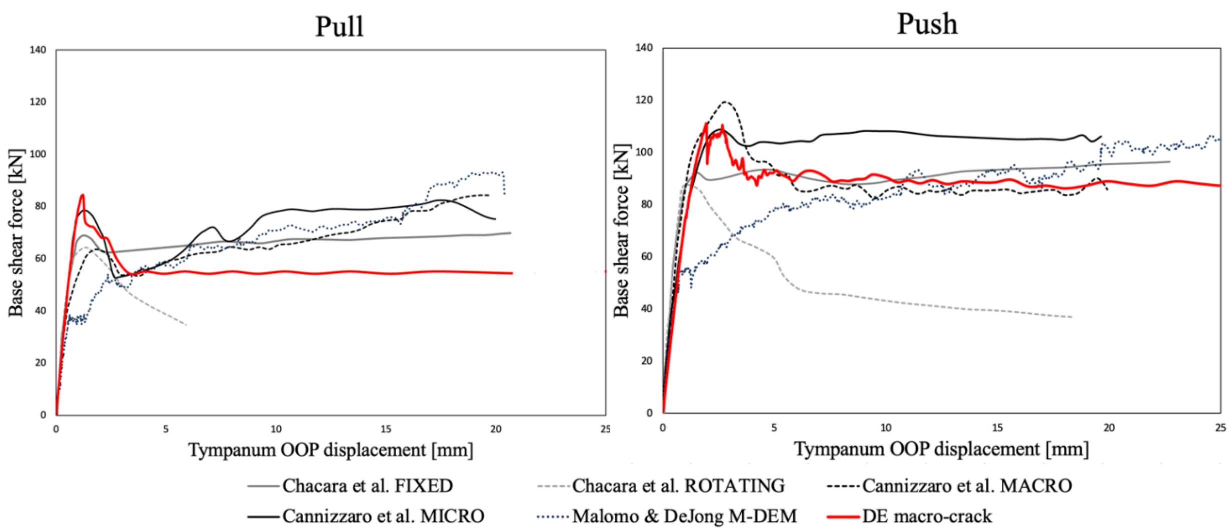

(a) (b)

Figure 2.29. Comparison between the force-displacement curves versus previous FEM/DEM results under (a) pulling load and (b) pushing load

With regard to the collapse mechanism, the U-shaped wall exhibits distinct behaviour in two orthogonal directions. Specifically, during a pull-type loading scenario, the central opening façade is observed to detach from both longitudinal walls, as evidenced in **Figure 2.30**a. On the other hand, under a push-type loading condition, the central façade is subject to severe damage, primarily characterized by the fracture of the top tympanum at its midpoint and the formation of two diagonal cracks originating from the bottom outside corners of the central opening and extending towards the bottom outside corner of the façade, as illustrated in **Figure 2.30**b.

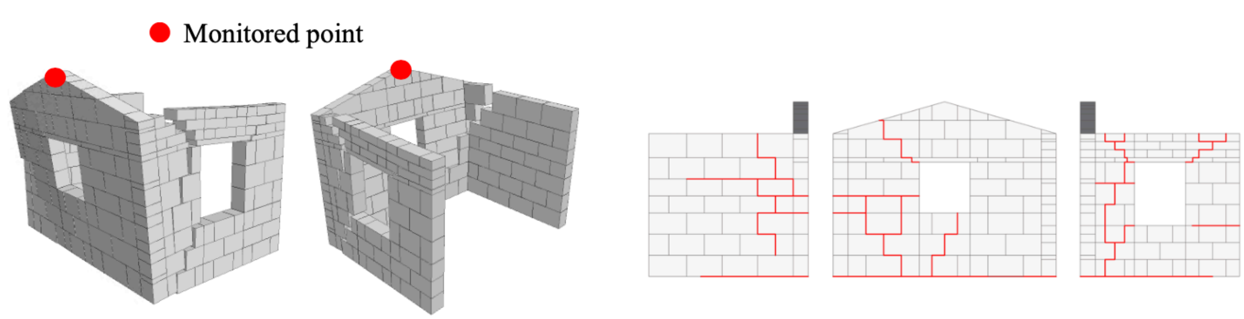

(a)

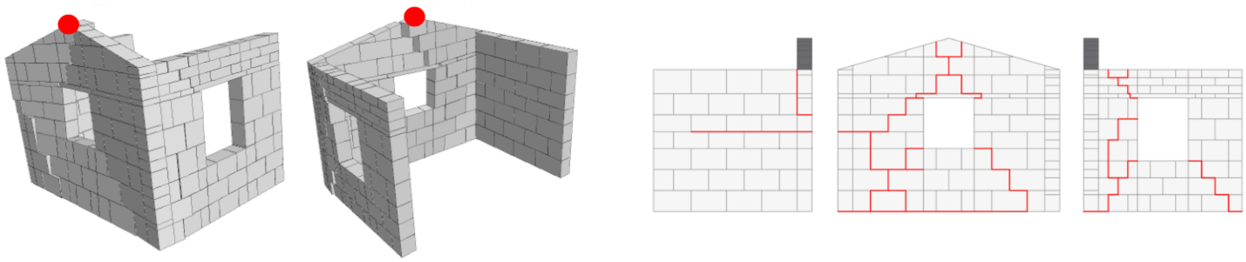

(b)

Figure 2.30. Damage and crack patterns of the U-shaped wall under (a) pulling load and (b) pushing load

In order to conduct the shake-table test on the U-shaped wall, it is imperative to examine its dynamic characteristics beforehand. The 3DEC software facilitates the assessment of eigenfrequencies in the presence of rigid blocks. Subsequently, an eigenvalue analysis using the aforementioned software yielded a fundamental natural frequency of 26 Hz, which was predominantly governed by the OOP motion of the top tympanum. The obtained frequency was found to be in agreement with the experimentally determined natural frequency of 21.3 Hz. The second dynamic parameter is the damping ratio and the damping ratio scheme may range from zero to stiffness, mass, or a combination of these factors, as observed in studies conducted by (Malomo, Mehrotra, et al., 2021), (Malomo & DeJong, 2021b), (Çaktı et al., 2016) and (Kim et al., 2021) respectively. However, when conducting DEM simulations, particularly for large structures, as noted by Lemos & Campos Costa, mass-proportional damping is often the only viable option, a view supported by recent papers (Malomo & DeJong, 2022a, 2022b). Therefore, the dynamic analysis outlined in the study under consideration employed a 5% mass-proportional damping.

Following the dynamic shake-table test, a comparative analysis was conducted between the final damage pattern observed in the numerical model and the corresponding experimental findings. The presence of a window opening in the North wall and a blind wall on the South side resulted in an asymmetric dynamic behaviour, which led to a concentration of damage on the North side of the U-shaped wall, while the South wall remained relatively undamaged. Notably, **Figure 2.31** reveals that the majority of the cracks observed in the test were accurately replicated in the numerical model, with the exception of partial collapses that were observed in the experimental findings did now show numerically, specifically on the North wall, and the top tympanum of the central wall.

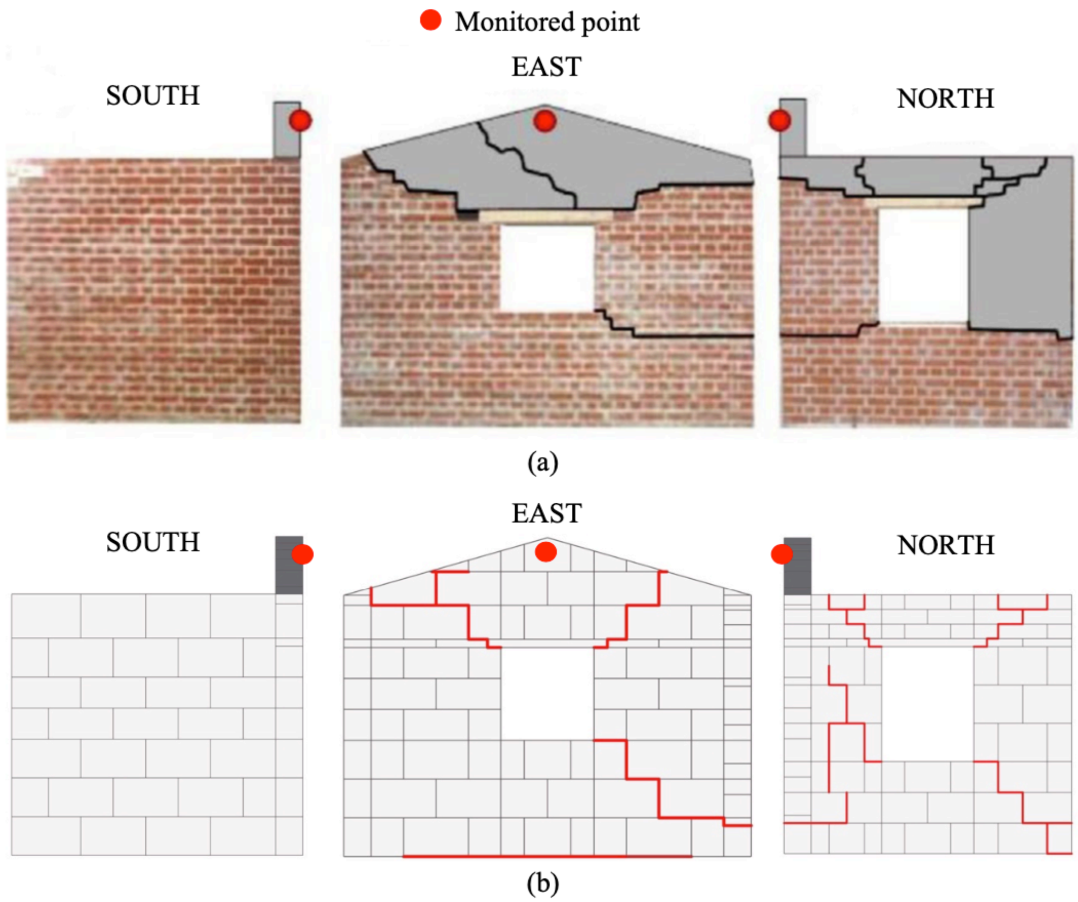

Figure 2.31. Damage pattern of the U-shaped wall of (a) experiment wall (Candeias et al., 2017); (b) numerical model

The displacement time-history records of the monitored point located at the tympanum were solely obtained from TEST04 onwards (see **Figure 2.32**), owing to the insubstantial deformation noticed during the earlier tests, namely, TEST01 to TEST03. This approach was taken to mitigate the computational expenses associated with data collection. Upon comparing the displacement histories of the studied model with those obtained via the M-DEM modelling method by Malomo and experimental results, satisfactory conformity was observed from TEST04 to TEST06, validating the model's capability to accurately replicate the measured deformations under low-level acceleration phases. However, during TEST07, the experimental displacements were notably underestimated in the numerical model. This underestimation was also observed in Malomo's M-DEM model. Finally, during TEST08, despite the numerical model accurately reproducing the experimental cracks, significant deformation was not observed numerically. This can be attributed to the use of larger blocks, resulting in a stiffer numerical model, which explains why the model did not undergo partial collapse.

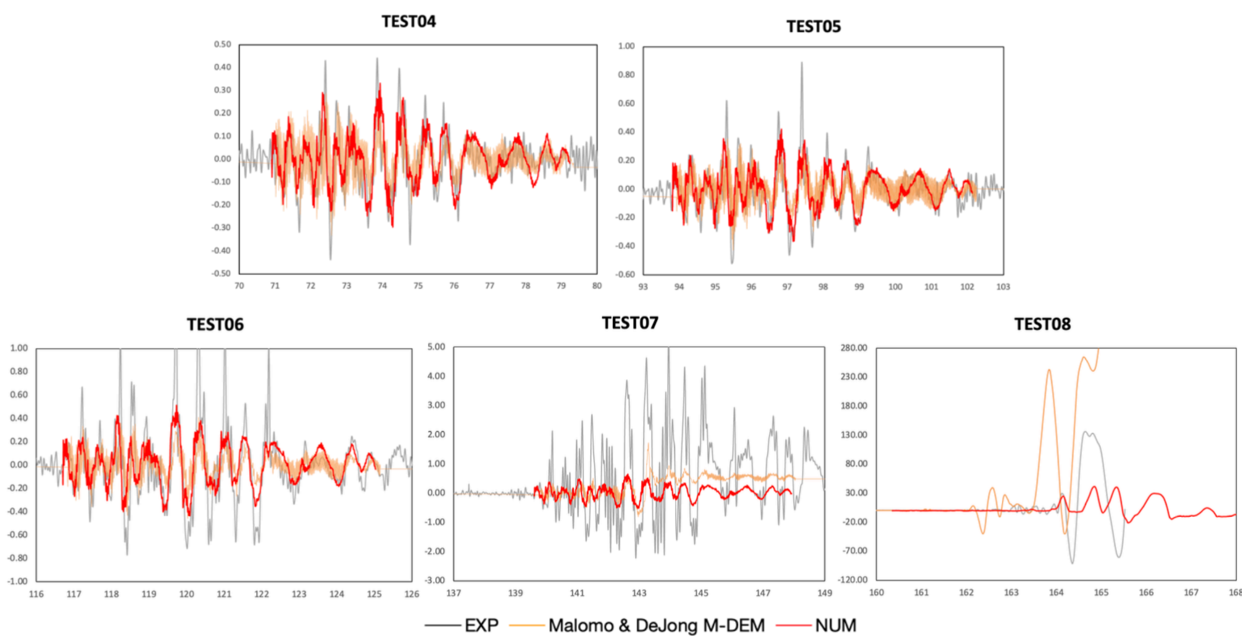

Figure 2.32. Tympanum displacement time-histories comparison

Chapter 3 - IP Seismic Response of URM Building Aggregates Using DE Macro-crack Network

3.1 Influencing factors on the monotonic response of URM building aggregates

URM building aggregates may originate from progressive construction periods typical of old structures. As cities and towns organically grow, adjacent masonry buildings may contain materials of various ages. In addition, traditional construction practices do not consistently feature the same structural system in masonry aggregates. In some instances, neighbouring buildings have individual vertical load-resisting systems. Others feature a shared wall which supports the vertical loads of both buildings (Kasai & Maison, 1997a). It can be difficult to estimate the seismic response of these masonry aggregates because of the complex construction systems present in a single masonry aggregate. Different material use, a variety in the number of adjacent buildings and a variety of building heights contribute to the large uncertainty experienced in seismic response. The interaction of these parameters and the effect on seismic resistance is largely unknown. Parametric analyses are one solution to explore the influence of the structural uncertainties on the seismic response of the masonry aggregates and provide reasonable explanations for the effects of this variation. In this study, the parametric results concerning the various typologies of masonry aggregates are included to investigate the effects of material properties construction periods, number of adjacent buildings, and building height within seismic pounding response.

3.1.1 Material degradation

The first parameter studied in this analysis is the material properties. Material properties can vary within a single structure due to the level of material degradation present as well as the presence of structural material of different ages, due to maintenance or reconstruction phases in the lifetime of a structure. Material degradation can occur in old masonry buildings due to the ongoing effects of time, environmental actions, existing damage due to external loading and level of maintenance. Adjacent buildings commonly will be constructed at different times or renovation/maintenance projects contribute to the high probability that each structure will not have the same material properties. Building aggregates with different material ages/properties may exhibit significant differences in dynamic behaviour during seismic activity. One way to incorporate the effect of masonry degradation is to use lower values for the strength parameters of masonry to reflect the degradation of masonry material properties (Park et al., 2009). In this research, two levels of degradation from the initial condition of building material properties (DL0) were considered. A slight degradation level (DL1) and severe degradation level (DL4) were incorporated in the parametric analysis, based on a probabilistic analysis of brick masonry materials (Saviano et al., 2022). Under this definition, all material parameters mentioned in **Table 3.1** were reduced by 15% and 50% for DL1 and DL4 respectively, summarized in **Table 3.1**. The studied building aggregates consist of six different combinations of three selected material levels (see **Figure 3.1**). For each material property combination, two adjacent façades contain a layout with regular openings (the DW as described in **section 2.6**) at the same height. These cases were studied under monotonic pushover analyses and all façades were modelled with the DE macro-crack modelling strategy. In each case, pushover loads were only applied to the steel beams of the leftmost façade and the horizontal displacements were monitored at the top of the mid-joint between the two adjacent facades indicated in blue dots.

Table 3.1. Degraded mechanical properties at different degradation levels.

material ID	E_m	G_m	f_c	f_t	c	ϕ	G_c	G_f^I	G_f^{II}
	[MPa]	[MPa]	[MPa]	[MPa]	[MPa]	[°]	[N/m]	[N/m]	[N/m]

DL1 (masonry)	1267	507	5.27	0.0425	0.06	25.5	8500	4.25	17
DL1 (bricks)	1267	507	12.75	0.85	1.275	30	17544	68	106
DL4 (masonry)	745	298	3.38	0.025	0.038	15	5000	2.5	10
DL4 (bricks)	745	298	7.8	0.5	0.75	18.5	10732	40	62.5

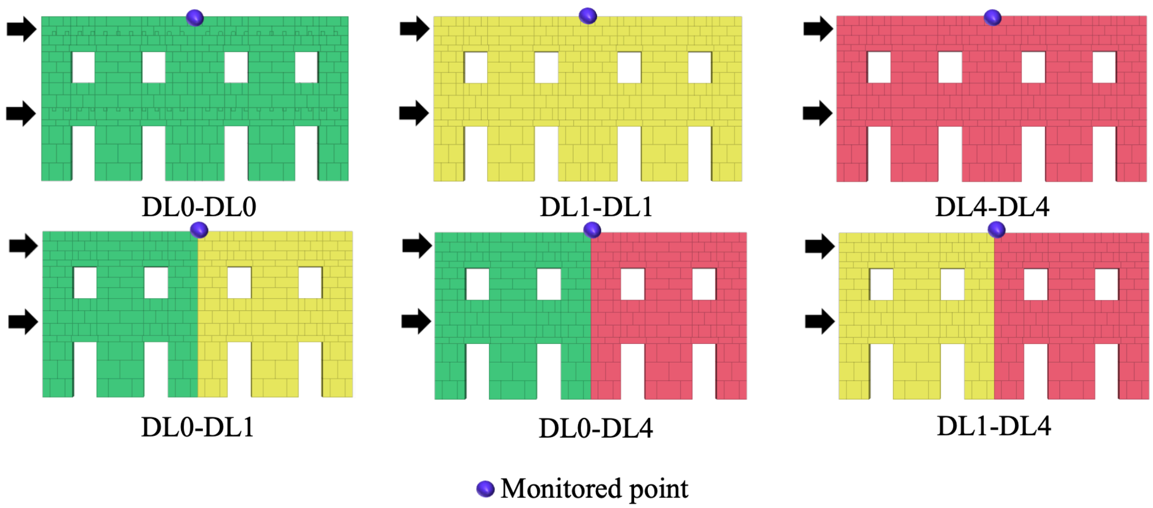

Figure 3.1. Building aggregates with different material-level combinations.

The macro-model results were processed to display the load-displacement behaviour of varying combinations of degradation levels. From the force-displacement curves (see **Figure 3.2**a), as the total degradation level of the building's aggregate increases almost all curves gradually decrease indicating a progressive reduction in stiffness and peak shear force capacity. In addition, sharp decreases in peak shear force capacity between the combination DL1-DL1 and DL1-DL4 and the combination DL1-DL4 and DL4-DL4 were observed. The severe-degraded façade (DL4) decreases the structural capacity of the aggregate to the greatest extent, displaying the importance of material degradation on structural capacity. With respect to the failure modes of each masonry aggregate, two distinct crack propagation patterns can be identified. The first pattern occurs when the same material degradation levels are applied (DL0-DL0, DL1-DL1, and DL4-DL4) while the second pattern is observed in the building aggregates with different material degradation levels (DL0-DL1, DL0-DL4, and DL1-DL4), indicated in **Figure 3.2**a. In both patterns, there were five stages in the crack propagation process. In the first crack propagation pattern, cracks first developed in the spandrels on both facades. Next, shear cracks formed first at the connection between the two facades and then after in the central piers of the loaded façade. Cracks then propagated to the exterior pier of the loaded façade and the central pier of the unloaded façade and finally cracks spread to the exterior pier of the unloaded façade. In contrast, the second pattern exhibits only one variation in comparison to the first pattern, whereby the initial structural failure occurs specifically at the mid-joint interface connecting two external facades. (**Figure 3.2**b).

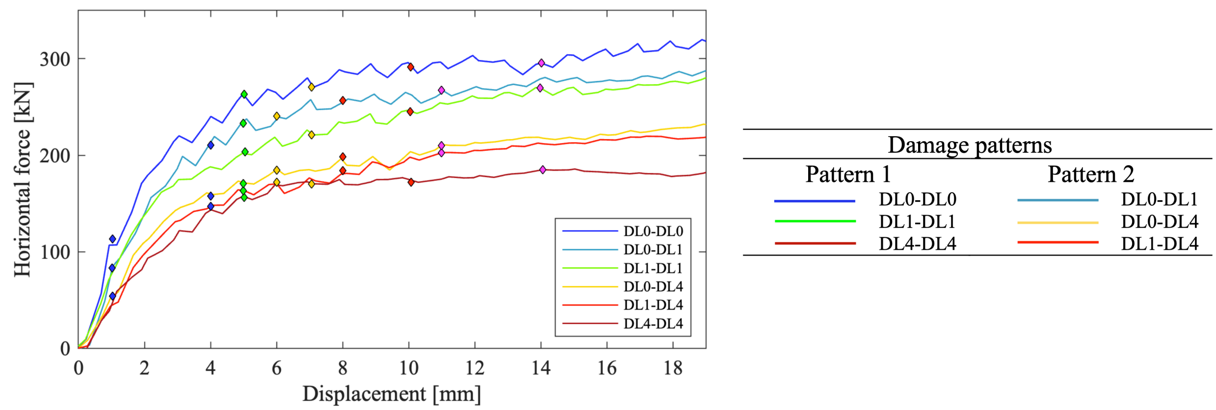

(a)

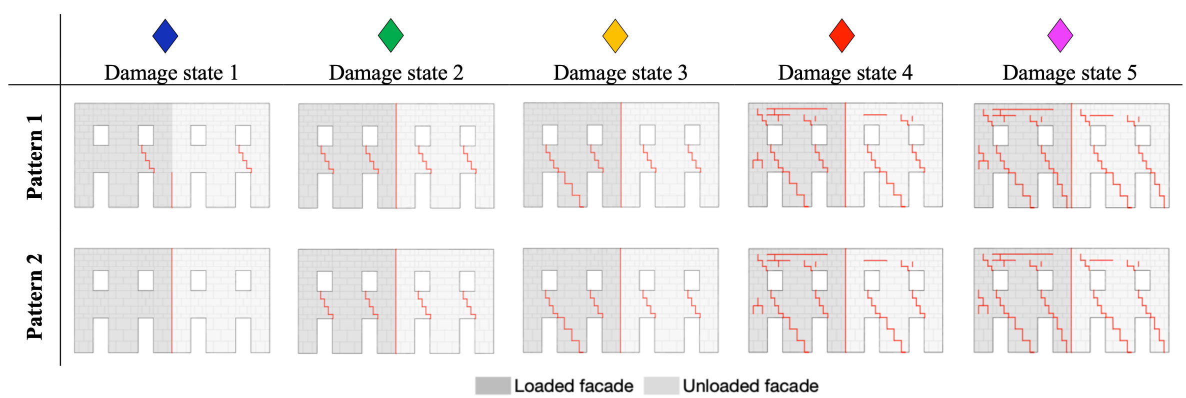

(b)

Figure 3.2. (a) Force-displacement curves and (b) crack propagation of two damage patterns

3.1.3 Number of adjacent buildings

It is imperative to emphasize that the seismic performance of a single structure can fluctuate depending on the number of neighbouring buildings within an architectural cluster. This phenomenon was observed during the 2010 Christchurch earthquake ($M_w = 6.3$), where seismic pounding transpired within a sequence of uniform-height URM buildings, leading to severe cracking in the leftmost building, as confirmed by post-event field inspections. To investigate this phenomenon, the second phase of the parametric analysis examines the impact of the number of adjacent buildings on the seismic response of the building cluster. The analysis involves a comparison of four URM clusters, each containing one to four facades (refer to **Figure 3.3**). The examined building clusters comprise adjoining facades with a uniform DW opening layout at the same overall building height and original material properties. Monotonic pushover analyses are conducted using the respective DE macro-crack models, with pushover loads applied solely to the steel beams of the leftmost façade in each scenario and the horizontal displacements of the building aggregates were monitored at the top right corner of the rightmost façade (indicated in blue dots).

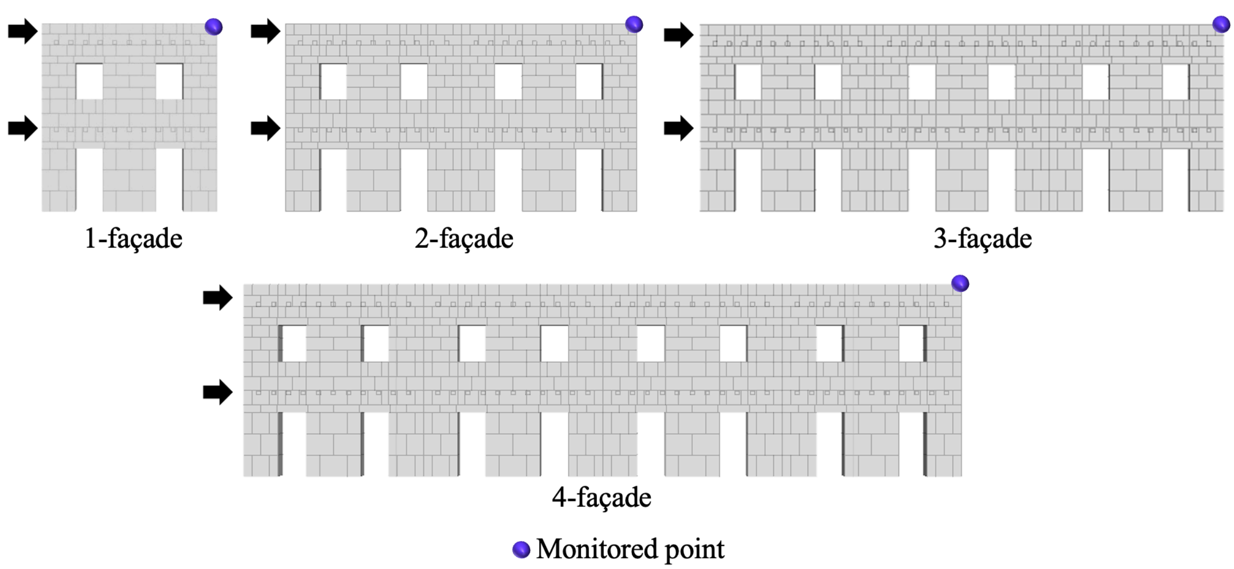

Figure 3.3. Building aggregates of different numbers of adjacent buildings

Figure 3.4a demonstrates that an augmentation in the number of adjoining buildings results in an amplification of the peak shear capacity of the URM building aggregate which is directly proportional to the number of adjacent buildings while the initial stiffness of the URM building aggregate remains unchanged. Upon analyzing the damage characteristics of four clusters of URM buildings (as shown in **Figure 3.4**b), a decrease in damage was noted on the upper floor as the number of buildings in each aggregate increased. Specifically, when three adjacent buildings were present, cracks were predominantly observed at the pier, with shear cracks on the spandrel only occurring on the farthest façade from the pushover load. The spandrels of the remaining two façades remained intact. Additionally, damage to the mid-joint between the two adjacent façades was confined to the pier level and the building as a whole did not lose its integrity. In the four façades case, no diagonal shear cracks were observed in the spandrels of any façade and all mid-joints remained undamaged.

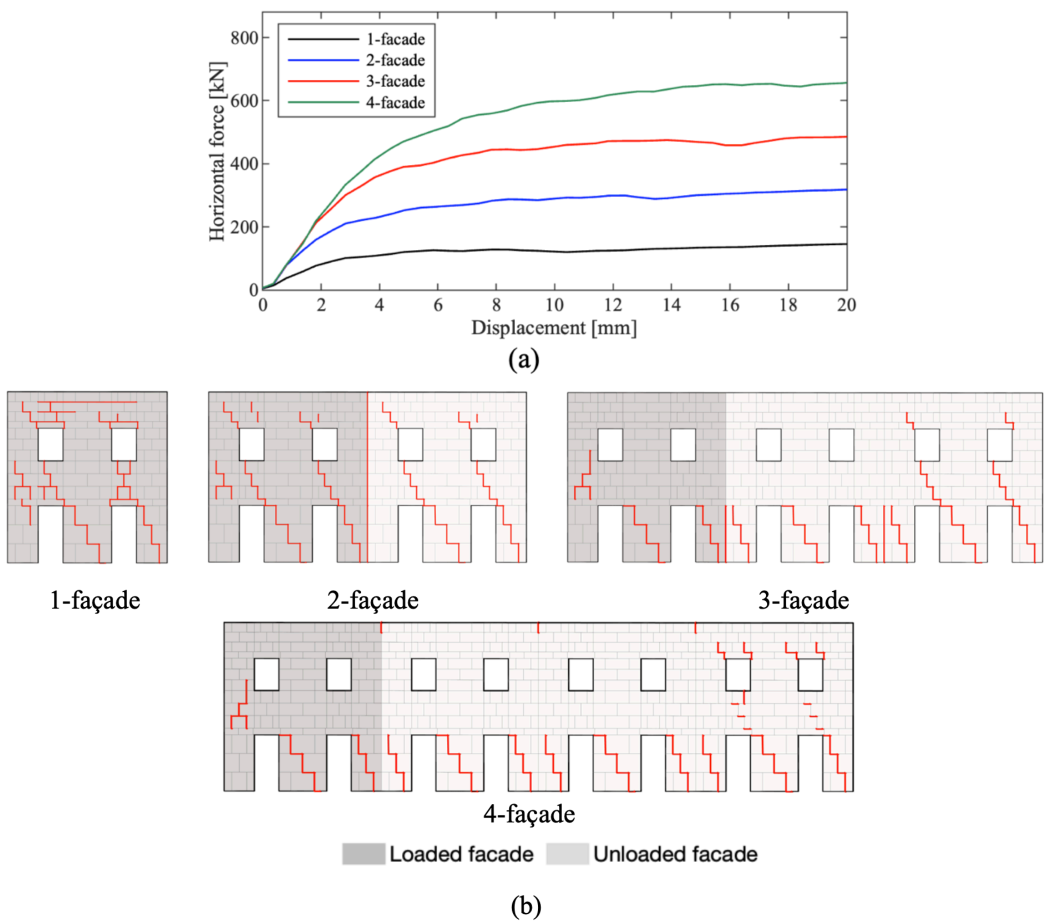

Figure 3.4. (a) Force-displacement curve and (b) damage pattern of the URM building aggregates with increasing number of façades components.

3.1.4 Building heights

The final phase of the parametric analysis considers adjacent URM buildings of differing heights. In this situation, local failures due to pounding may arise when the point of impact from the two buildings has different heights, especially when the shorter structure has a larger stiffness than the taller structure Baker 2007). The numerical investigation in this study determines the influence factor of building height in seismic response. A single-storey, 4.5 m tall, URM building with irregular opening layouts and a two-storey, 6.435 m tall, URM building with regular opening layouts are analyzed. Zero separation between the two façades is included to demonstrate the worst-case scenario pounding effects. Two in-plane monotonic pushover analyses (positive and negative directions) were performed using the DE macro-crack model (see **Figure 3.5**). In each analysis, the pushover loads were only applied to one façade directly through to steel beams (highlighted in red) and the horizontal displacements were monitored at the top of the mid-joint between the two façades (indicated in blue dots).

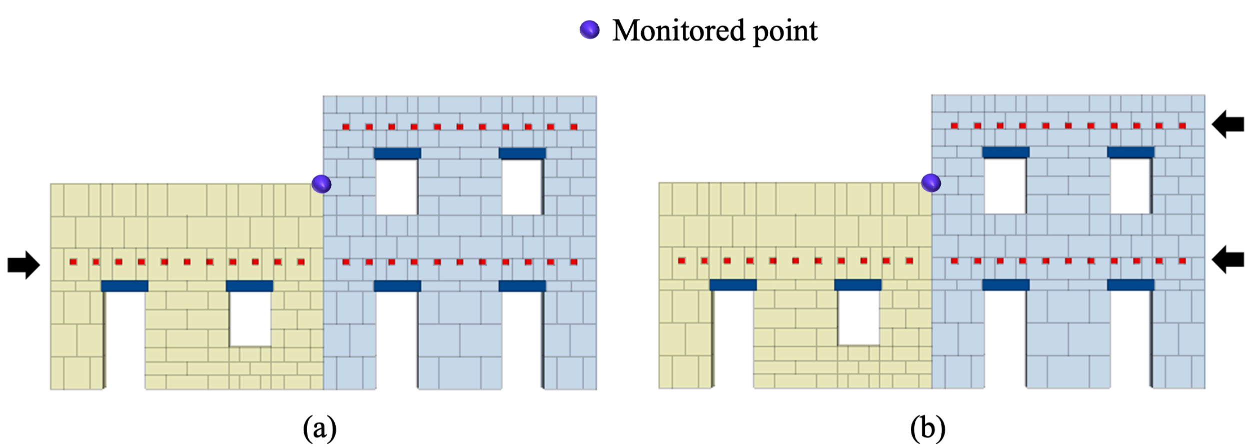

Figure 3.5. The numerical model of two unequal-height URM buildings loading in positive (left) and negative (right) directions

URM building aggregates with façades of two heights were subjected to negative and positive pushover loads and results display different damage patterns and stiffness depending on the loading direction (**Figure 3.6**). In the first damage state, damage to the entire mid-joint and the development of diagonal shear cracks in the spandrel of the taller wall were observed in both loading directions. However, the shorter wall experienced damage above both openings. In the shorter wall, a diagonal shear crack also developed below the window opening in the negative load case and minimal damage under the positive load case. In addition, the shear force at this damage state was higher in the negative direction than in the positive direction (230kN vs 150kN). In the second damage state, the extensive damage was visible and diagonal shear cracks characterize the dominant failure mechanism spreading through the spandrel and piers. The shorter façade under the negative load experienced a greater number of cracks above openings than under the positive load. Moreover, in this damaged state, the URM building aggregate displayed higher deformability in the positive loading condition as compared to the negative loading condition. In the third and final damage state, cracks were fully developed in both façades with a greater number of cracks observed in the shorter building subjected to negative loading. Interestingly, the force-displacement curve revealed a significant difference between the positive and negative loading directions. The URM building aggregate only sustained a limited extent of deformability at the peak shear force in the positive loading direction, whereas in the negative loading condition, an increase in shear force was noticed after the displacement of 18mm. In the negative pushover analysis, the shear force capacity was found to be higher than in the positive pushover analysis (approximately 350kN and 300kN, respectively). One explanation for this difference is that the shorter façade is stiffer than the taller façade due to the lower height and smaller number of openings, allowing the URM building aggregate to exhibit a higher lateral capacity and higher ductility in the negative loading direction.

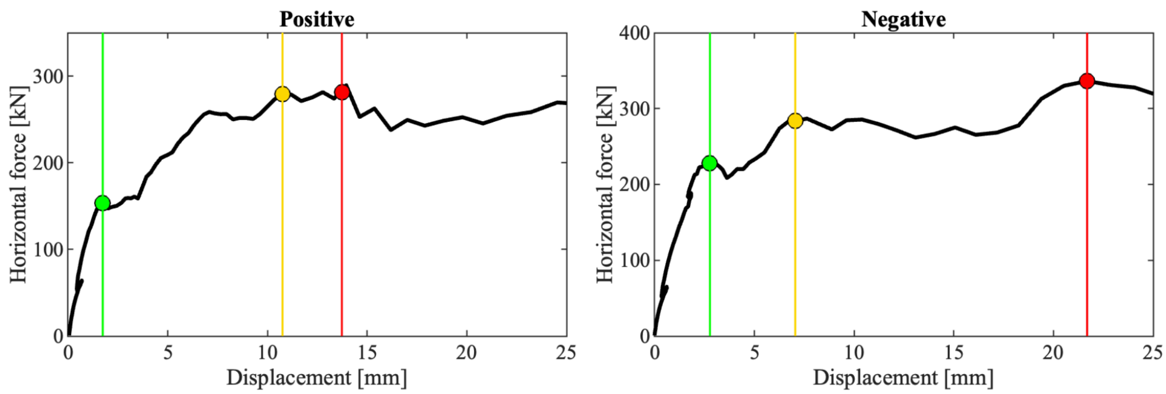

(a)

(b)

Figure 3.6. (a) Force-displacement curve, (b) crack patterns of the positive (left) and negative (right) loading directions

3.2 IP pounding response of a pair of URM façades with the same configurations under uniaxial acceleration time-histories

This section presents an analysis of the in-plane pounding response of a pair of URM façades with identical structural typologies as the DW (as described in **section 2.6**), hereafter referred to as the URM pair. The two façades in the URM pair are placed in direct contact with each other, without any structural gap, to investigate the potential interactions resulting from their proximity and to capture the pounding response as accurately as possible (refer to **Figure 3.7**). The nonlinear dynamic analyses are performed according to the experimentally validated numerical modelling strategy (see **chapter 2**), based on the use of the DE macro-crack networks, capable of accurately monitoring the load-displacement relationship and the collapse behaviour of the URM structures with a large reduced computational effort.

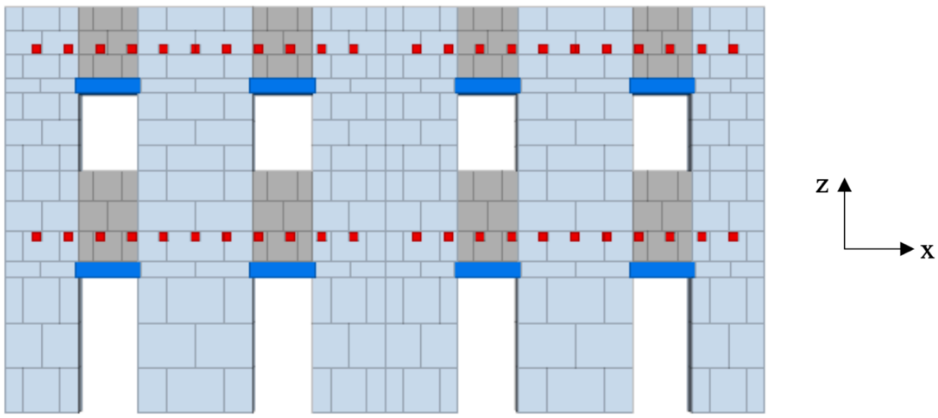

Figure 3.7. The numerical model for the in-plane pounding analyses using the DE macro-crack networks

The numerical simulations of the pounding response are obtained under the assumption that the OOP failure is prevented due to the presence of well-connected rigid floor diaphragms to the orthogonal walls. As a result, the box behaviour (Marques, 2015) of each façade of the URM pair was considered in this analysis. Prior to simulation, the fundamental frequency of the URM pair's horizontal IP mode shape was obtained from eigenvalue analysis using the 3DEC program. The frequency was determined to be 7 Hz. Then, to enable a comprehensive evaluation of the pounding effect in terms of collapse capacity, 11 uniaxial accelerometers are selected and imposed in the direction parallel to the URM pair (X-direction). These accelerometers are chosen to cover a range of intensities, as discussed in the subsequent sections. Finally, based on the obtained numerical simulation results, a broader and more realistic understanding of the impact of the pounding on the URM pair is provided.

3.2.1 Ground motion selection

The selection of accelerograms to be used as ground motions for the numerical simulations was a critical aspect of this study, given that the primary objective was to assess the interactions between the URM pair and the resulting pounding responses. Accordingly, the chosen accelerograms had to cover a wide range of intensities to reflect the pounding effect on the URM pair, subject to varying levels of ultimate damage status.

To establish a correlation between the ground motion parameter and the level of structural damage, a new intensity measure called cumulative absolute velocity (CAV) was first introduced as a potential damage-related ground motion intensity measure through a study sponsored by the Electric Power Research Institute (Reed & Kassawara, 1990). Thereafter, Several studies have looked into the global damage potential of ground motion parameter CAV (Cabañas et al., 1997; Campbell & Bozorgnia, 2010). Numerous studies have demonstrated the successful correlation between CAV obtained from ground motion instruments and qualitative levels of structural damage.

Different from other intensity measures like peak ground acceleration (PGA) which only relates to the maximum acceleration of the time history, CAV is dependent on the whole duration which is equal to the integration of acceleration over time (the dark areas in **Figure 3.8**), and its mathematical expression is as follows:

$$CAV = \int_{0}^{t_{max}} |a(t)|dt \tag{1}$$

Where $|a(t)|$ is the absolute value of acceleration at time t, and t_{max} is the duration of ground motion.

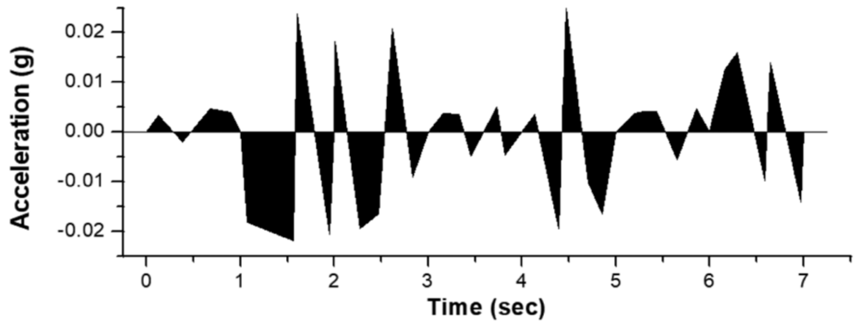

Figure 3.8. Illustration of CAV of an acceleration time history (Wu et al., 2022).

Regarding the number of ground motions, the National Building Code of Canada (NBCC 2015) recommends the use of at least eleven ground motion time histories in nonlinear dynamic analysis to more accurately predict structural responses. Therefore, for this study, a total of 11 ground motion records were selected from the Pacific Earthquake Engineering Research (PEER, 2015) strong motion database, to cover a range of intensities expressed in terms of CAV along the X direction. (see Table 3.2). These records were divided into two groups representing the near-field and far-field earthquakes, respectively. The first group contains 7 near-field ground motions with the epicentral distance (R_{rup}) ranging from 0 km to 15km. The second group comprises 4 far-field ground motions, with R_{rup} greater than 15km. Moreover, in this study, the significant duration (D595) was used to determine the duration of each ground motion record used in the analysis. D595 is calculated based on the integral of the acceleration, and specifically, the time elapsed from 5% to 95% of the total integral. The formula used to calculate D595 is based on the work of Bommer and Marytínezpereira (1999) and can be expressed mathematically as follows:

$$D595 = \int_{0.05}^{0.95} a^2 dt \quad (2)$$

Where a is the ground motion acceleration.

In the following sub-sections, for the sake of clarity, the ground motions will be indicated by using the ground motion record labels reported in Table 3.2.

Table 3.2. Main properties of the selected ground motions

label		Earthquake	Station	M_w	R_{rup} [km]	D595 [s]	PGA [g]	CAV [m/s]
1		Saguenay	Dickey	5.9	194.8	21.5	0.1	3.4
2		Hollister	Hollister City Hall	5.6	19.6	16.9	0.1	4.2
3		Southnapa	Crockett	6.0	20.1	3.1	1.0	6.0
4		Friuli	Tolmezzo	6.5	15.8	4.9	0.3	6.7
5		Christchurch	Resthaven	6.2	5.1	11.2	0.4	8.3
6		Morgan Hill	Coyote Lake Dam	6.2	0.5	4.1	0.7	9.3
7		Loma pierta	LGPC	6.9	3.9	7.8	0.6	12.6
8		Imperial Valley	Bonds Corner	6.5	2.7	9.1	0.8	16.4
9		Northridge	Jensen Filter Plant	6.7	5.4	9.0	1.0	17.9
10		Chi-Chi	CHY080	7.6	2.7	17.5	0.9	25.9
11		Nahanni	Site 1	6.8	6.8	29.6	1.1	40.5

3.2.2 Pounding damage

The typical approach for obtaining the global damage of an individual URM structure is by observing the damage pattern and crack distributions during DEM simulation. However, due to the complex nature of pounding, which comes along with the internal shear and tension failures between blocks, it is challenging to visualize numerically. To distinguish between pounding damage and global damage and evaluate its impact on the URM pair, a comparison URM pair was introduced. The only difference between the original URM pair and the comparison URM pair is the material of the mid joint between the two individual façades. In the comparison model, the mortar joint was replaced with a purely elastic material that does not allow for slip or tensile failure (see **Figure 3.9**b). This assumption guarantees that no pounding occurs between the two individual URM façades of the comparison model since they are linked into a monolithic façade. Also, the displacement monitoring point is also indicated as a green dot shown in **Figure 3.9**.

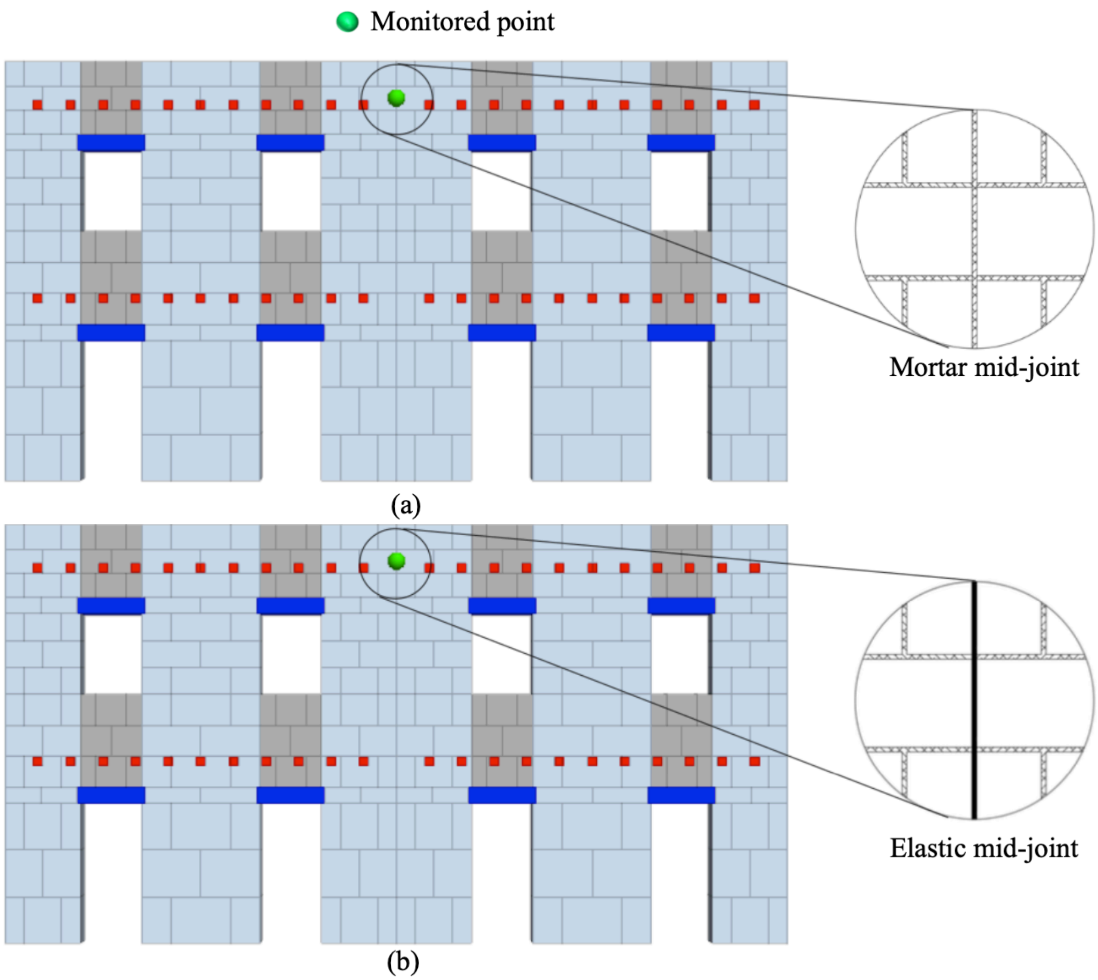

Figure 3.9. (a) Actual model with mortar mid-joint and (b) comparison model with elastic mid-joint

The analyzing results of the two comparisons of URM pairs subjecting to a wide range of different ground motion histories are herein presented. It is important to note that the results do not account for the post-collapse mechanism as it is unpredictable and contributes little to the pounding assessment. With a view to better investigating how changing the mid-joint properties will affect the pounding response, the damage level for each ground motion analysis was thus classified into the following categories referred from the paper of Malomo, Morandini, et al., 2021 (also graphically represented in **Figure 3.10**) :

i. Slight to moderate damage (S-MD) Negligible or minor damage (maximum residual crack opening lower than 1 mm, as suggested in Baggio et al., 2007), easily repairable and for which the structure could be considered fully operational.

ii. Moderate to heavy damage (M-HD) Maximum residual crack opening higher than 1 mm. At this stage, which could be considered a life safety limit state, the damage might be considered relevant but still repairable.

iii. Near collapse conditions (NC) Collapse-prevention threshold, characterized by heavy and widespread structural damage.

iv. Partial collapse (PC) is when the collapse of one or more members or entire sub-structures occurs, associated with heavy and widespread structural damage.

v. Global collapse (GC) is when the entire structure experiences global failure.

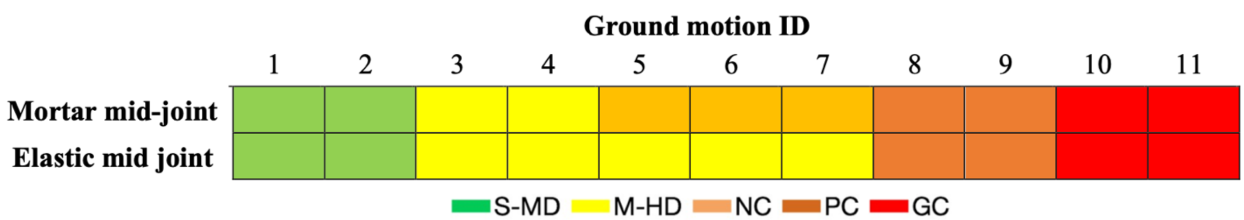

Figure 3.10. Damage states for each mid-joint scenario induced by different ground motion records

The numerical results suggest that the URM pair with mortar mid-joint has limited capacity to withstand seismic forces. Initially, the damage was isolated to the first-floor spandrel and lintel areas of both façades. Specifically, records 1 and 2 revealed S-MD damage only in these regions. Moreover, records 3 and 4 displayed a comparable damage pattern (M-HD), featuring the development of diagonal shear cracks that had yet to expand. By the time records 5, 6, and 7 were simulated, the URM pair exhibited NC damage with widespread cracking and joint failures. The weakest structural components were also noted to display signs of collapse. PC damage occurred during records 8 and 9 which are characteristerised by a higher value of CAV, wherein the widening of the cracks led to the failure of lintels and parts of the first-floor spandrel. Finally, ground motions 10 and 11 predicted the GC damage of the URM pair.

The comparison URM pair, on the other hand, indicated distinct global damage patterns resulting from the application of accelerograms 5, 6, and 7, while similar patterns were observed in other cases. Specifically, only sporadic damage in the form of M-HD was observed in the first-floor spandrel and around the lintel of the URM pair when subjected to records 5, 6, and 7 (see **Figure 3.11**). This type of damage did not significantly compromise the overall structural integrity of the URM pair. The maximum displacement diagram (see **Figure 3.12**b), which depicts the maximum absolute displacement of the monitoring point on the second floor for both mid-joint scenarios, sheds further light on this phenomenon. As anticipated, the maximum displacement experienced a decline of varying degrees in the mid-joint scenarios employing an elastic joint compared to those employing a mortar joint, resulting from the higher horizontal stiffness conferred by the use of an elastic mid-joint. This effect was most pronounced in cases 5, 6, and 7, with a reduction of over 300% relative to the mortar mid-joint counterpart. Moreover, as shown in **Figure 3.12**a, the hysteretic curves demonstrate a narrower shape for the comparison model, particularly during moderate-intensity earthquakes (records 5, 6, and 7).

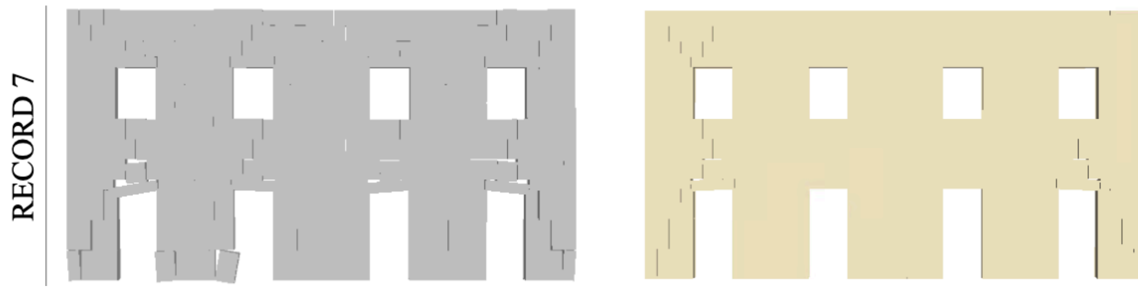

Figure 3.11. Damage pattern of two comparison model when subjecting to the moderate-intensity earthquakes

Therefore, the comparison between the global damage patterns of the two URM pairs preliminary highlights that URM structures are particularly susceptible to pounding during moderate-intensity earthquakes leading to near-collapse (with CAV ranging from 8 m/s to 13 m/s). Conversely, in high-intensity earthquakes (with CAV higher than 16m/s), its impact on the overall damage pattern, ranging from partial to global collapse, is limited. Furthermore, in low-intensity earthquakes (with CAV lower than 6m/s), pounding is either absent or minimal, with building aggregates remaining largely intact after the shock.

Based on the aforementioned study, in order to mitigate the pounding damage induced by earthquakes in URM structures, it is suggested that the mid-joint between URM building aggregates can be strengthened through various applications. As an example, the use of viscoelastic materials or friction dampers as link elements to transmit forces through structures and dissipate energy during structural vibrations (Abdel Raheem, 2014; Charleson & Southcombe, 2017; Jankowski & Mahmoud, 2016). While these papers provide valuable insights into the potential approach of utilizing special link elements to reduce pounding damage, further research is necessary to fully analyze the feasibility of its implementation and the associated implementation details.

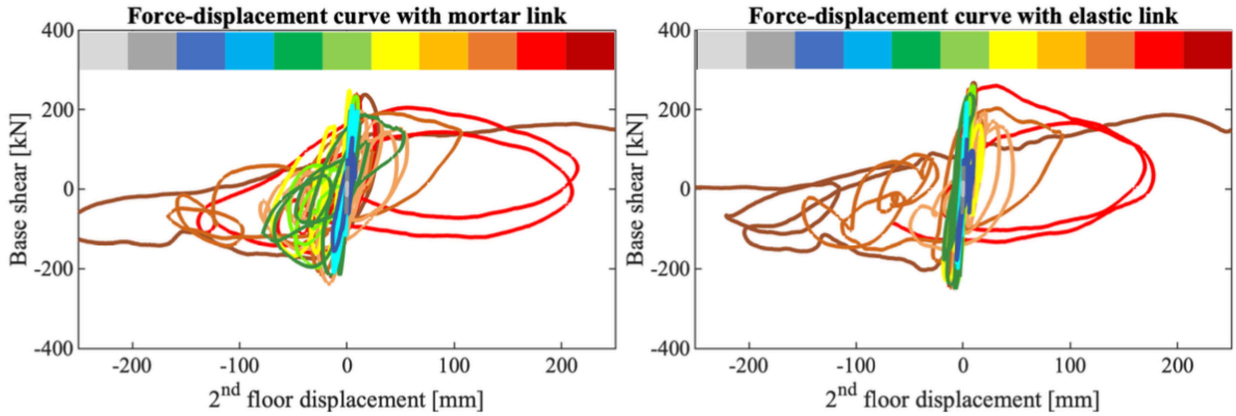

(a)

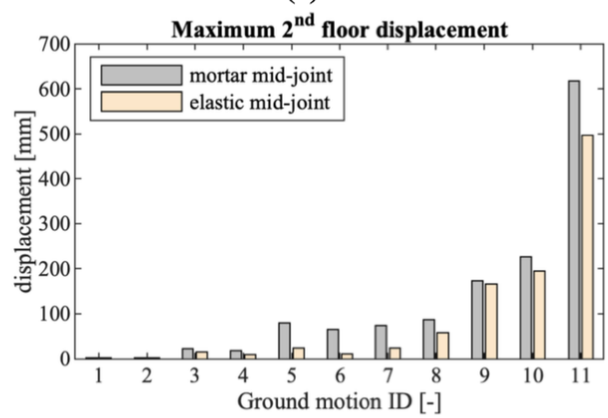

(b)

Figure 3.12. The numerical result of the two mid-joint scenarios subjected to 11 ground motion records (a) second-floor displacement vs. base shear hysteretic curves (b) maximum second-floor displacement

3.2.3 Pounding intensity

In this section, a further evaluation was conducted to investigate the pounding intensity incurred by the studied URM pair through an analysis of the impact force response spectrum induced by selected ground motions. In order to comprehensively capture the pounding response at all levels of the URM pair, four distinct points (P1, P2, P3, and P4) situated at various heights of the mid-joint were monitored for pounding impact forces in both normal (along the x-axis) and shear (along the z-axis) directions, as depicted in **Figure 3.13**.

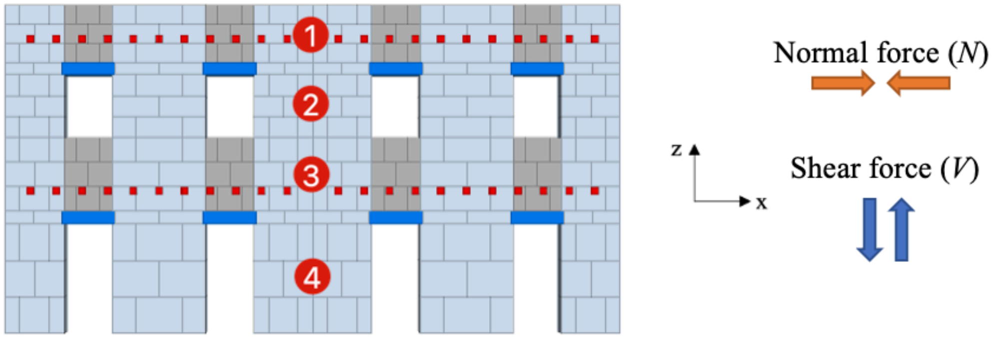

Figure 3.13. Monitoring points of the pounding impact forces in both normal and shear directions

The impact force response time histories, in both normal force and shear force, that were obtained at the four monitoring points are illustrated in **Figure 3.14**. The curves depicting the impact force time histories for the 11 ground motion records at the same monitoring point were consolidated in a single graph (the corresponding colour label was adopted from Table 3.2). Consequently, four graphs on the left were generated for normal impact forces and the other four on the right for shear impact forces.

The intensity of the pounding was first evaluated by analyzing the peak impact forces at each monitoring point. The peak normal and shear impact forces were recorded for different ground motion records and summarized in **Table 3.3**. The results indicate that the distribution of forces acting on the URM pair during an impact event varies with height. Specifically, the highest peak impact normal force was consistently observed at the top layer in every excitation record, as shown by the values of P1. Among these, the maximum value was when the URM pair subjecting to the record 11 which corresponds to about 13% of its weight. Conversely, the peak impact shear force showed a different pattern, with a gradual increase in value as the monitoring height decreased in nearly every case.

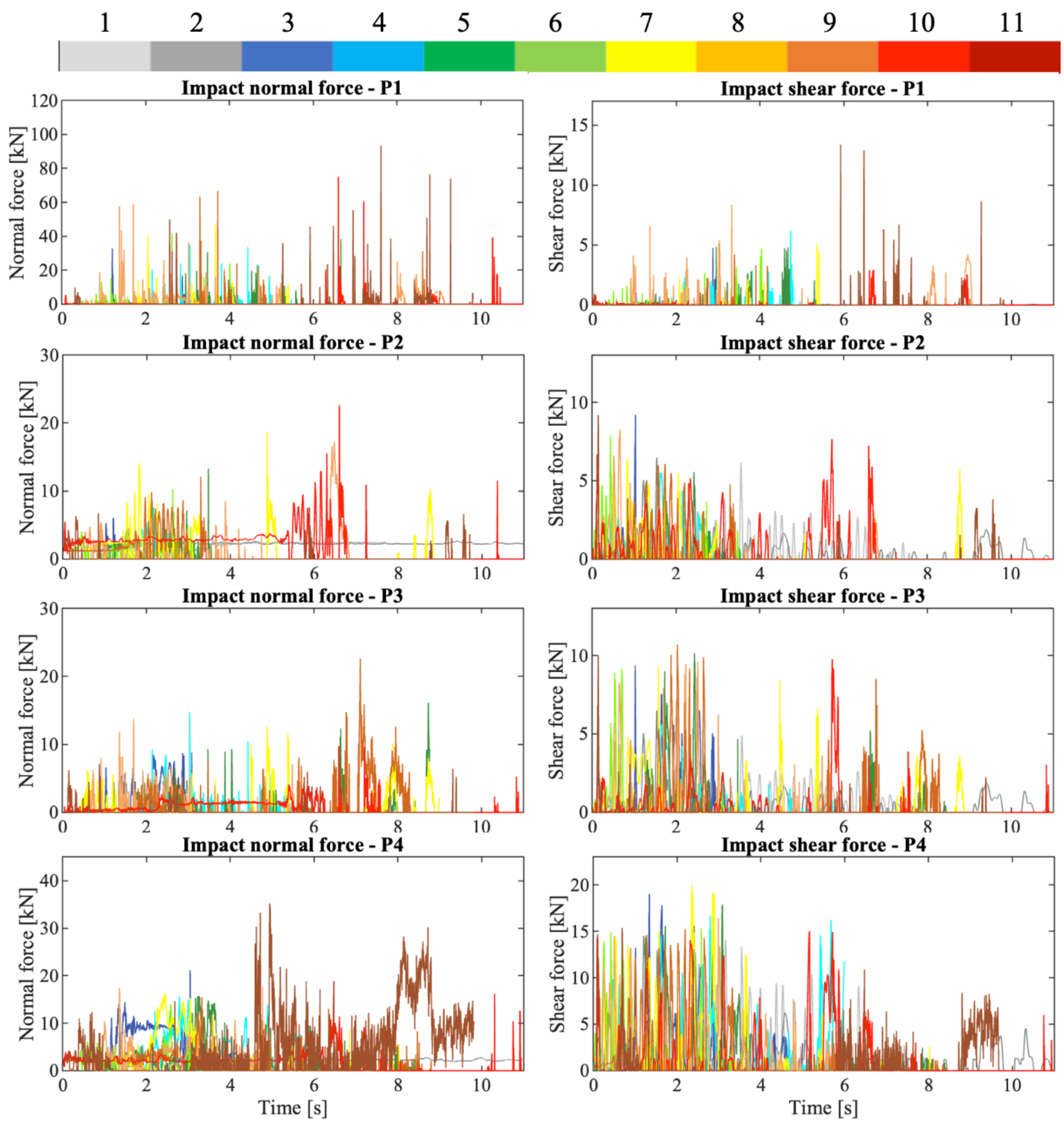

Figure 3.14. Impact force time histories at different heights in both normal and shear directions

Additionally, the factors $r(N/V)$ for each ground motion record are also reported in the same table They are defined as the ratio between the peak normal force and its corresponding peak shear force at the same monitoring points (expressed in integer form), indicating the force contribution at the certain monitored point. The results obtained from different heights of the buildings reveal that the normal force is the dominant force at the top level during the collision, with $r(N/V)$ ranging from 6 to 10. As one moves down to the bottom, the contribution of both normal and shear forces becomes similar, with around 70% of the $r(N/V) = 1$.

Table 3.3. Peak impact force in normal and shear directions and the ratios between them

Record ID	**Peak impact forces (kN)**								$r(N/V)$			
	Normal force (N)				Shear force (V)							
	P1	P2	P3	P4	P1	P2	P3	P4	P1	P2	P3	P4
1	-	-	-	-	-	-	-	-	-	-	-	-
2	-	-	-	-	-	-	-	-	-	-	-	-
3	33	6	9	21	5	9	10	19	7	1	1	1
4	35	8	15	16	6	7	11	17	6	1	1	1
5	39	13	16	16	5	8	16	19	8	2	1	1
6	41	10	6	14	5	8	11	15	9	1	1	1
7	47	19	13	16	6	9	10	20	7	2	1	1
8	59	17	14	18	10	10	11	17	6	2	1	1
9	67	12	23	15	6	7	13	15	10	2	2	1
10	75	23	25	16	11	10	12	15	7	2	2	1
11	93	10	20	56	13	9	10	23	7	1	2	2

Upon comparison of the peak impact forces resulting from various ground motion records at the same monitoring points, a remarkable discovery has emerged, revealing a nearly linear relationship between the peak impact normal forces at the highest layer (P1) and the CAV with $R^2 = 0.977$ (see **Figure 3.15**a). Moreover, this strong linear correlation was also found in the shear direction at P1 as evidenced by R^2 value of 0.923, as indicated in **Figure 3.15**b. It is worth noting that records 1 and 2 did not involve any pounding, as evidenced by the S-MD damage exhibited by the URM pair. As a result, in this part of the analysis, these records were excluded from the results. In contrast, at lower elevations (P2, P3, and P4), the observed impact force patterns lacked a discernible relationship, with the data displaying irregular trends. Thus, a positive outlook can be inferred from this outcome which suggests that the top layer's peak impact force may exhibit a robust association with the global damage condition of the building complexes, as the CAV is an indicator of the structural damage level.

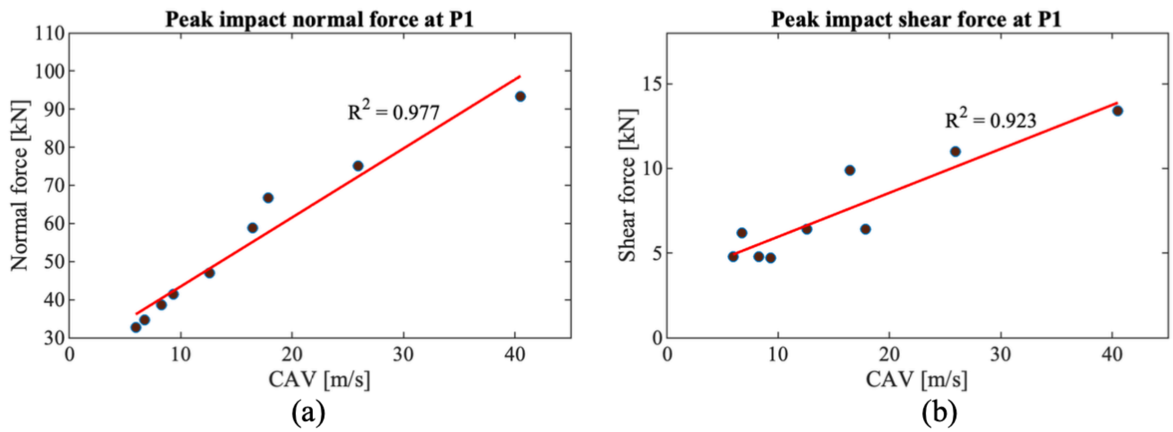

Figure 3.15. Correlation between CAV and peak impact force in (a) normal and (b) shear direction

In the context of the pounding impact forces, the effect of pounding can be observed by examining the envelopes of absolute acceleration. Considering the significant errors in the acceleration data derived by the 3DEC software due to its reliance on velocity differentiation over extremely small time increments, leading to the potential escalation of computational inaccuracies this study employs an alternative approach to determine the acceleration histories of each monitoring point by analyzing the change in velocity over time for each 11 ground motion records. The resulting absolute maximum accelerations are presented in **Table 3.4**. The study found that during the moment of collision between two URM facades, short acceleration pulses of up to 6g can be generated, whereas the maximum acceleration is below 0.7g when no pounding occurs. These findings are supported by a similar numerical simulation conducted on the pounding between two steel frames, where a maximum acceleration of 3g was obtained (Filiatrault et al., 1994). The difference between the two maximum acceleration values can be explained by the fact that masonry structures have a higher weight than steel structures, resulting in higher acceleration levels.

Table 3.4. Pounding impact accelerations, frequency and duration of the different ground motions

Record ID	Impact acceleration [m/s²]				Pounding frequency [n/s]				Pounding duration [s]			
	P1	P2	P3	P4	P1	P2	P3	P4	P1	P2	P3	P4
1	0.3	0.4	0.2	0.6	-	-	-	-	-	-	-	-
2	0.3	0.4	0.2	0.4	-	-	-	-	-	-	-	-
3	2.7	2.1	2.5	2.4	2	2	2	4	0.02	0.03	1.19	1.62
4	4.6	2.5	2.6	1.3	2	4	11	4	0.13	0.25	0.30	0.90
5	2.8	1.8	2.5	1.9	4	2	5	10	0.05	0.22	0.16	0.71
6	3.1	3.6	2.1	2.3	4	6	5	6	0.03	0.33	0.11	0.91
7	2.5	2.8	1.6	2.4	4	2	5	8	0.05	0.23	0.29	1.20
8	5.4	3.4	4.0	3.4	3	5	5	9	0.32	0.46	0.64	1.45
9	3.8	3.1	3.2	3.1	2	5	6	11	0.02	0.52	0.37	0.21
10	4.3	1.7	1.2	1.6	2	3	4	4	0.19	0.24	0.15	0.33
11	3.9	4.1	4.2	5.7	5	2	3	21	0.10	0.08	0.05	0.19

Finally, the frequency and duration of masonry pounding were investigated using different ground motions (records 3-11). The pounding frequency was determined by calculating the average pounding number per second at each monitoring point, while the maximum pounding duration was determined by identifying the longest impact duration in the ground motion history. The results in **Table 3.4** reveal that lower levels experienced a higher frequency of pounding and a longer maximum pounding duration compared to higher levels. Specifically, the URM pair at the bottom layer showed an average pounding frequency of 9 times per second, while these values were 3, 4, and 5 at P1, P2, and P3, respectively. Similarly, the average maximum pounding duration at P4 was 0.84 seconds, while the values were less than 0.4 seconds at higher levels. This observation can be explained by the higher levels' flexible nature, which results in more damping and energy dissipation during collisions, leading to a shorter pounding duration.

Furthermore, the study found that the frequency and duration of pounding varied across different ground motions, and these values did not show a strong correlation with any of the ground motion parameters. Therefore, the findings suggest that various factors contribute to the frequency and duration of masonry pounding, not solely related to the earthquake intensity.

Chapter 4 – Conclusion

Unreinforced masonry (URM) buildings are complex structures which possess non-uniform material characteristics. When masonry structures are part of a building aggregate, seismic pounding creates complex dynamics and collision effects which impact the seismic response of individual structures. In this study, the in-plane (IP) pounding response of the URM building aggregate was investigated using a recently developed DE Macro-Crack Network based on the Distinct Element Method (DEM) enabling the modelling of large-scale structures in reduced computational effort. The proposed modelling strategy consists in idealizing main URM components as an equivalent assembly of large rigid blocks connected by nonlinear interface springs, where axial, shear and torsion failures can occur. The layout of such layers forms a network of discontinuities or macro-cracks, that is conceived in such a way that diagonal and top/bottom horizontal cracks can form in URM members, enabling the macro-model to capture the main failure modes typically exhibited under IP seismic load. Before it was implemented into the pounding analysis, several validations were conducted by comparing macro-modelling outcomes against experimental outcomes obtained by previous researchers on clay brick URM under different loading conditions (monotonic pushover, cyclic load, and dynamic load). The results demonstrate the potential of the proposed methodology in facilitating the acquisition of force-displacement curves and damage patterns that align with those observed experimentally while exhibiting enhanced computational efficiency. Moreover, this model also exhibited the capability in simulating the out-of-plane (OOP) failure of walls under both IP and OOP combined actions.

Thereafter, a parametric analysis based on monotonic pushover loading was conducted to investigate the influence of material degradation state, number of adjacent buildings and varying heights of the URM building aggregate on the seismic response of adjacent buildings in seismic pounding scenarios. Such preliminary exercises explore the mechanical interaction among adjacent buildings. The results show that as the total degradation level of the building's aggregate increases, there is a progressive reduction in stiffness and peak shear force capacity. In addition, an increase in adjacent buildings can lead to an increase in the initial stiffness and peak shear capacity, but resulting in less damage as the number of buildings in each aggregate increases. it has been verified that in URM structures comprising two interconnected buildings with different heights, the lateral stiffness is greater when subjected to loading originating from the taller building compared to that from the shorter building side.

Finally, this study extends the investigation of the pounding response to a pair of URM facades under dynamic loading conditions, considering both damage and intensity perspectives. The results reveal that URM building aggregates are particularly susceptible to pounding under moderate-intensity earthquakes with a cumulative absolute velocity (CAV) ranging between 8 m/s and 13 m/s. To mitigate the pounding damage induced by earthquakes, the mid-joint between the URM building aggregates could be strengthened through various applications, such as the use of viscoelastic materials as link elements. Moreover, the distribution of impact forces acting on the URM pair during the pounding event was found to vary with height, with normal force dominating at the top level, while both normal and shear forces contributed equally at lower elevations. Notably, a linear relationship was found between peak impact forces at the highest layer and the CAV, indicating that the top layer's peak impact force may serve as an indicator of the global damage condition of the building complexes. The results also indicate that the lower levels of the URM pair experienced a higher frequency of pounding and a longer maximum pounding duration compared to the higher levels.

To summarize, this study introduces a novel analysis framework for explicitly simulating the pounding response of URM building aggregates using the DE macro-crack network. In future investigations, the proposed framework can be further developed to incorporate various uncertainties related to URM building aggregates, including but not limited to irregular opening arrangements, varying heights, and distinct typologies. This extension will provide valuable insights into the influence of uncertainties on the pounding response, constituting a promising direction for future research endeavours.

Reference

Abdel Raheem, S. E. (2014). Mitigation measures for earthquake induced pounding effects on seismic performance of adjacent buildings. *Bulletin of Earthquake Engineering*, *12*(4), 1705–1724. https://doi.org/10.1007/s10518-014-9592-2

Abrams, D. P., AlShawa, O., Lourenço, P. B., & Sorrentino, L. (2017). Out-of-plane seismic response of unreinforced masonry walls: conceptual discussion, research needs, and modeling issues. *International Journal of Architectural Heritage*, *11*(1), 22–30. https://doi.org/10.1080/15583058.2016.1238977

Anagnostopoulos, S. A. (1988). Pounding of buildings in series during earthquakes. *Earthquake Engineering & Structural Dynamics*, *16*(3), 443–456. https://doi.org/10.1002/eqe.4290160311

Anagnostopoulos, S. A., & Spiliopoulos, K. V. (1992). An investigation of earthquake induced pounding between adjacent buildings. *Earthquake Engineering & Structural Dynamics*, *21*(4), 289–302. https://doi.org/10.1002/EQE.4290210402

Antunez, G., Abo-El-Ezz, A., Nollet, M. J., & Khaled, A. (2015). Analyse de la vulnérabilité sismique hors-plan des bâtiments de maçonnerie de pierre de l'Est canadien : Application aux bâtis du Vieux-Québec et du Vieux-Montréal. *Canadian Journal of Civil Engineering*, *42*(12), 1125–1134. https://doi.org/10.1139/cjce-2015-0123

Asteris, P. G., Plevris, V., Sarhosis, V., Papaloizou, L., Mohebkhah, A., & Komodromos, P. (2015). Numerical modeling of historic masonry structures. In *Handbook of Research on Seismic Assessment and Rehabilitation of Historic Structures* (pp. 213–256). IGI Global. https://doi.org/10.4018/978-1-4666-8286-3.ch007

Augenti, N., & Parisi, F. (2010). Learning from Construction Failures due to the 2009 L'Aquila, Italy, Earthquake. *Journal of Performance of Constructed Facilities*, *24*(6), 536–555. https://doi.org/10.1061/(asce)cf.1943-5509.0000122

Augenti, N., Parisi, F., Prota, A., & Manfredi, G. (2011). In-Plane Lateral Response of a Full-Scale Masonry Subassemblage with and without an Inorganic Matrix-Grid Strengthening System. *Journal of Composites for Construction*, *15*(4), 578–590. https://doi.org/10.1061/(asce)cc.1943-5614.0000193

Baggio, C., Bernardini, A., Colozza, R., Corazza, L., Bella, M., Di Pasquale, G., Dolce, M., Goretti, A., Martinelli, A., Orsini, G., Papa, F., & Zuccaro, G. (2007). Field Manual for post-earthquake damage and safety assessment and short term countermeasures (AeDES). *JRC Scientific and Thechnical Reports*, 1–100. http://ipsc.jrc.ec.europa.eu

Baker, J. W. (2007). Measuring bias in structural response caused by ground motion scaling. *Pacific Conference on Earthquake Engineering*, *056*, 1–6. https://doi.org/10.1002/eqe

Bertero, V. V., & Collins, R. G. (1973). *Investigation of the failures of the Olive View stairtowers during the San Fernando earthquake and their implications on seismic design*. Earthquake Engineering Research Center, University of California.

Berti, M., Salvatori, L., Orlando, M., & Spinelli, P. (2017). Unreinforced masonry walls with irregular opening layouts: reliability of equivalent-frame modelling for seismic vulnerability assessment. *Bulletin of Earthquake Engineering*, *15*(3), 1213–1239. https://doi.org/10.1007/s10518-016-9985-5

Beyer, K., & Dazio, A. (2012). Quasi-static cyclic tests on masonry spandrels. *Earthquake Spectra*, *28*(3), 907–929. https://doi.org/10.1193/1.4000063/ASSET/IMAGES/LARGE/10.1193_1.4000063-TABLE1.JPEG

Bommer, J. J., & Marytínezpereira, A. (1999). The effective duration of earthquake strong motion. *Journal of Earthquake Engineering*, *3*(2), 127–172. https://doi.org/10.1080/13632469909350343

Brando, G., Rapone, D., Spacone, E., O'Banion, M. S., Olsen, M. J., Barbosa, A. R., Faggella, M., Gigliotti, R., Liberatore, D., Russo, S., Sorrentino, L., Bose, S., & Stravidis, A. (2017). Damage Reconnaissance of Unreinforced Masonry Bearing Wall Buildings After the 2015 Gorkha, Nepal, Earthquake. *Earthquake Spectra*, *33*(Special issue 1), S243–S273. https://doi.org/10.1193/010817EQS009M

Brown, T., & Elshaer, A. (2022). Pounding of structures at proximity: A state-of-the-art review. *Journal of Building Engineering*, *48*, 103991. https://doi.org/10.1016/j.jobe.2022.103991

Bruneau, M. (1994). State-of-the-art report on seismic performance of unreinforced masonry buildings. *Journal of Structural Engineering*, *120*(1), 230–251. https://doi.org/10.1061/(asce)0733-9445(1994)120:1(230)

Cabañas, L., Benito, B., & Herráiz, M. (1997). An approach to the measurement of the potential structural damage of earthquake ground motions. *Earthquake Engineering and Structural Dynamics*, *26*(1), 79–92. https://doi.org/10.1002/(SICI)1096-9845(199701)26:1<79::AID-EQE624>3.0.CO;2-Y

Çaktı, E., Saygılı, Ö., Lemos, J. V., & Oliveira, C. S. (2016). Discrete element modeling of a scaled masonry structure and its validation. *Engineering Structures*, *126*, 224–236. https://doi.org/10.1016/j.engstruct.2016.07.044

Caliò, I., Marletta, M., & Pantò, B. (2012). A new discrete element model for the evaluation of the seismic behaviour of unreinforced masonry buildings. *Engineering Structures*, *40*, 327–338. https://doi.org/10.1016/J.ENGSTRUCT.2012.02.039

Campbell, K. W., & Bozorgnia, Y. (2010). A ground motion prediction equation for the horizontal component of cumulative absolute velocity (CAV) based on the PEER-NGA strong motion database. *Earthquake Spectra*, *26*(3), 635–650. https://doi.org/10.1193/1.3457158

Candeias, P. X., Campos Costa, A., Mendes, N., Costa, A. A., & Lourenço, P. B. (2017). Experimental Assessment of the Out-of-Plane Performance of Masonry Buildings Through Shaking Table Tests. *International Journal of Architectural Heritage*, *11*(1), 31–58. https://doi.org/10.1080/15583058.2016.1238975

Cannizzaro, F., & Lourenço, P. B. (2017). Simulation of Shake Table Tests on Out-of-Plane Masonry Buildings. Part (VI): Discrete Element Approach. *International Journal of Architectural Heritage*, *11*(1), 125–142. https://doi.org/10.1080/15583058.2016.1238973

Chácara, C., Mendes, N., & Lourenço, P. B. (2017). Simulation of Shake Table Tests on Out-of-Plane Masonry Buildings. Part (IV): Macro and Micro FEM Based Approaches. *International*

Journal of Architectural Heritage, *11*(1), 103–116. https://doi.org/10.1080/15583058.2016.1238972

Charleson, A., & Southcombe, M. (2017). Strategies for the seismic upgrading of pairs of buildings in a historic precinct. *Bulletin of the New Zealand Society for Earthquake Engineering*, *50*(1), 50–58. https://doi.org/10.5459/bnzsee.50.1.50-58

Chau, K. T., Wang, L. X., & Wei, X. X. (2006). Torsional poundings between two adjacent asymmetric structures. *4th International Conference on Earthquake Engineering*, 12–13.

Chau, K. T., Wei, X. X., Guo, X., & Shen, C. Y. (2003). Experimental and theoretical simulations of seismic poundings between two adjacent structures. *Earthquake Engineering and Structural Dynamics*, *32*(4), 537–554. https://doi.org/10.1002/eqe.231

Chen, S. Y., Moon, F. L., & Yi, T. (2008). A macroelement for the nonlinear analysis of in-plane unreinforced masonry piers. *Engineering Structures*, *30*(8), 2242–2252. https://doi.org/10.1016/j.engstruct.2007.12.001

Cole, G., Dhakal, R., Carr, A., & Bull, D. (2010). Interbuilding pounding damage observed in the 2010 darfield earthquake. *Bulletin of the New Zealand Society for Earthquake Engineering*, *43*(4), 382–386. https://doi.org/10.5459/bnzsee.43.4.382-386

Costa, A. A., Arêde, A., Costa, A. C., Penna, A., & Costa, A. (2013). Out-of-plane behaviour of a full scale stone masonry façade. Part 2: Shaking table tests. *Earthquake Engineering and Structural Dynamics*, *42*(14), 2097–2111. https://doi.org/10.1002/eqe.2314

Crozet, V., Politopoulos, I., & Chaudat, T. (2019). Shake table tests of structures subject to pounding. *Earthquake Engineering and Structural Dynamics*, *48*(10), 1156–1173. https://doi.org/10.1002/eqe.3180

Cundall, P. A., & Hart, R. D. (1992). Numerical modelling of discontinua. *Engineering Computations*, *9*(2), 101–113. https://doi.org/10.1108/EB023851/FULL/XML

Davis, L., & Malomo, D. (2022). Safeguarding Eastern Canada's old unreinforced masonry buildings from the seismic threat: a state-of-the-art review. *CSCE 2022 Annual Conference*.

Davis, R. O. (1992). Pounding of buildings modelled by an impact oscillator. *Earthquake Engineering & Structural Dynamics*, *21*(3), 253–274. https://doi.org/10.1002/eqe.4290210305

DeJong, M. J., Belletti, B., Hendriks, M. A. N., & Rots, J. G. (2009). Shell elements for sequentially linear analysis: Lateral failure of masonry structures. *Engineering Structures*, *31*(7), 1382–1392. https://doi.org/10.1016/j.engstruct.2009.02.007

Erdogan, Y. S., Kocatürk, T., & Demir, C. (2019). Investigation of the seismic behavior of a historical masonry minaret considering the interaction with surrounding structures. *Journal of Earthquake Engineering*, *23*(1), 112–140. https://doi.org/10.1080/13632469.2017.1309725

Ferrante, A., Loverdos, D., Clementi, F., Milani, G., Formisano, A., Lenci, S., & Sarhosis, V. (2021). Discontinuous approaches for nonlinear dynamic analyses of an ancient masonry tower. *Engineering Structures*, *230*, 111626. https://doi.org/10.1016/J.ENGSTRUCT.2020.111626

Filiatrault, A., & Cervantes, M. (1995). Separation between buildings to avoid pounding during earthquakes. *Canadian Journal of Civil Engineering*, *22*(1), 164–179. https://doi.org/10.1139/l95-015

Filiatrault, A., Cervantes, M., Folz, B., & Prion, H. (1994). Pounding of buildings during earthquakes: Canadian perspective. *Canadian Journal of Civil Engineering*, *21*(2), 251–265. https://doi.org/10.1139/l94-028

Ford, C. R. (1926). Earthquakes and Building Construction. In *Whitcombe and Tombs Limited, New Zealand*. Whitcombe \& Tombs, Limited.

Ghandil, M., & Aldaikh, H. (2017). Damage-based seismic planar pounding analysis of adjacent symmetric buildings considering inelastic structure–soil–structure interaction. *Earthquake Engineering and Structural Dynamics*, *46*(7), 1141–1159. https://doi.org/10.1002/eqe.2848

Giordano, N., De Luca, F., & Sextos, A. (2020). Out-of-plane closed-form solution for the seismic assessment of unreinforced masonry schools in Nepal. *Engineering Structures*, *203*, 109548. https://doi.org/10.1016/J.ENGSTRUCT.2019.109548

Gonen, S., Pulatsu, B., Erdogmus, E., Karaesmen, E., & Karaesmen, E. (2021). Quasi-Static Nonlinear Seismic Assessment of a Fourth Century A.D. Roman Aqueduct in Istanbul, Turkey. *Heritage 2021, Vol. 4, Pages 401-421*, *4*(1), 401–421. https://doi.org/10.3390/HERITAGE4010025

Hamp, E., Gerber, R., Pulatsu, B., Quintero, M. S., & Erochko, J. (2022). Nonlinear Seismic Assessment of a Historic Rubble Masonry Building via Simplified and Advanced Computational Approaches. *Buildings 2022, Vol. 12, Page 1130*, *12*(8), 1130. https://doi.org/10.3390/BUILDINGS12081130

Itasca Consulting Group Inc. (2013). *3DEC. Three Dimensional Distinct Element Code*.

Jankowski, R., & Mahmoud, S. (2016). Linking of adjacent three-storey buildings for mitigation of structural pounding during earthquakes. *Bulletin of Earthquake Engineering*, *14*(11), 3075–3097. https://doi.org/10.1007/s10518-016-9946-z

Jankowski, R., Seleemah, A., El-Khoriby, S., & Elwardany, H. (2015). Experimental study on pounding between structures during damaging earthquakes. *Key Engineering Materials*, *627*, 249–252. https://doi.org/10.4028/www.scientific.net/KEM.627.249

Karayannis, C. G., & Favvata, M. J. (2005). Inter-story pounding between multistory reinforced concrete structures. *Structural Engineering and Mechanics*, *20*(5), 505–526. https://doi.org/10.12989/sem.2005.20.5.505

Kasai, K., Jeng, V., & Maison, B. F. (1990). The significant effects of pounding-induced accelerations on building appurtenances. *Proceedings of Seminar on Seismic Design, Retrofit, and Performance of Nonstructural Components, ATC*, *29*.

Kasai, K., Jeng, V., Patel, P. C., Munshi, J. A., & Maison, B. F. (1992). Seismic pounding effects—survey and analysis. *Proceeding of 10th World Conference on Earthquake Engineering*, 3893–3898.

Kasai, K., & Maison, B. F. (1997). Building pounding damage during the 1989 Loma Prieta earthquake. *Engineering Structures*, *19*(3), 195–207. https://doi.org/10.1016/S0141-0296(96)00082-X

Kazemi, F., Miari, M., & Jankowski, R. (2021). Investigating the effects of structural pounding on the seismic performance of adjacent RC and steel MRFs. *Bulletin of Earthquake Engineering*, *19*(1), 317–343. https://doi.org/10.1007/s10518-020-00985-y

Khatiwada, S., Chouw, N., & Butterworth, J. W. (2013). Evaluation of numerical pounding models with experimental validation. *Bulletin of the New Zealand Society for Earthquake Engineering*, *46*(3), 117–130. https://doi.org/10.5459/bnzsee.46.3.117-130

Kim, J., Lorenzoni, F., Salvalaggio, M., & Valluzzi, M. R. (2021). Seismic vulnerability assessment of free-standing massive masonry columns by the 3D Discrete Element Method. *Engineering Structures*, *246*, 113004. https://doi.org/10.1016/j.engstruct.2021.113004

Lagomarsino, S., & Cattari, S. (2015). PERPETUATE guidelines for seismic performance-based assessment of cultural heritage masonry structures. *Bulletin of Earthquake Engineering*, *13*(1), 13–47. https://doi.org/10.1007/s10518-014-9674-1

Lagomarsino, S., Penna, A., Galasco, A., & Cattari, S. (2013). TREMURI program: An equivalent frame model for the nonlinear seismic analysis of masonry buildings. *Engineering Structures*, *56*, 1787–1799. https://doi.org/10.1016/j.engstruct.2013.08.002

Leite, J., Lourenco, P. B., & Ingham, J. M. (2012). Statistical Assessment of Damage to Churches Affected by the 2010–2011 Canterbury (New Zealand) Earthquake Sequence. *Http://Dx.Doi.Org/10.1080/13632469.2012.713562*, *17*(1), 73–97. https://doi.org/10.1080/13632469.2012.713562

Lemos, J. V., & Campos Costa, A. (2017). Simulation of Shake Table Tests on Out-of-Plane Masonry Buildings. Part (V): Discrete Element Approach. *International Journal of Architectural Heritage*, *11*(1), 117–124. https://doi.org/10.1080/15583058.2016.1237587

Lourenço, P. B. (1996). Computational strategies for masonry structures. In *PhD Thesis* (Vol. 70, Issue 08). http://www.narcis.nl/publication/RecordID/oai:tudelft.nl:uuid:4f5a2c6c-d5b7-4043-9d06-8c0b7b9f1f6f

Lourenço, P. B. (2002). Computations on historic masonry structures. *Progress in Structural Engineering and Materials*, *4*(3), 301–319. https://doi.org/10.1002/pse.120

Lourenço, P. B. (2009). Recent advances in masonry modelling: Micromodelling and homogenisation. *Multiscale Modeling In Solid Mechanics: Computational Approaches*, 251–294. https://doi.org/10.1142/9781848163089_0006

Lourenço, P. B., Mendes, N., Ramos, L. F., & Oliveira, D. V. (2011). Analysis of Masonry Structures Without Box Behavior. *Https://Doi.Org/10.1080/15583058.2010.528824*, *5*(4–5), 369–382. https://doi.org/10.1080/15583058.2010.528824

Lourenço, P. B., & Rots, J. G. (1997). Multisurface interface model for analysis of masonry structures. *Journal of Engineering Mechanics*, *123*(7), 660–668. https://doi.org/10.1061/(asce)0733-9399(1997)123:7(660)

Magenes, G., & Calvi, G. M. (1997a). In-plane seismic response of brick masonry walls. *Earthquake Engineering and Structural Dynamics*, *26*(11), 1091–1112. https://doi.org/10.1002/(SICI)1096-9845(199711)26:11<1091::AID-EQE693>3.0.CO;2-6

Magenes, G., & Calvi, G. M. (1997b). In-plane seismic response of brick masonry walls. *Earthquake Engineering and Structural Dynamics*, *26*(11), 1091–1112.

https://doi.org/10.1002/(SICI)1096-9845(199711)26:11<1091::AID-EQE693>3.0.CO;2-6

Magenes, G., Calvi, G. M., & Kingsley, G. R. (1995). Seismic testing of a full-scale, two-storey masonry building: Test procedure and measured experimental response. *Experimental and Numerical Investigation on a Brick Masonry Building-Prototype - Numerical Prediction of the Experiment, Report 3.0 - G.N.D.T.*, *January*, 1.1-1.41. https://doi.org/10.13140/RG.2.1.4590.2962

Malomo, D., & DeJong, M. J. (2021a). A Macro-Distinct Element Model (M-DEM) for simulating the in-plane cyclic behavior of URM structures. *Engineering Structures*, *227*(November 2020), 111428. https://doi.org/10.1016/j.engstruct.2020.111428

Malomo, D., & DeJong, M. J. (2021b). A Macro-Distinct Element Model (M-DEM) for out-of-plane analysis of unreinforced masonry structures. *Engineering Structures*, *244*, 112754. https://doi.org/10.1016/j.engstruct.2021.112754

Malomo, D., & DeJong, M. J. (2022a). A Macro-Distinct Element Model (M-DEM) for simulating in-plane/out-of-plane interaction and combined failure mechanisms of unreinforced masonry structures. *Earthquake Engineering and Structural Dynamics*, *51*(4), 793–811. https://doi.org/10.1002/eqe.3591

Malomo, D., & DeJong, M. J. (2022b). M-DEM simulation of seismic pounding between adjacent masonry structures. *Bulletin of Earthquake Engineering*, 1–26. https://doi.org/10.1007/s10518-022-01545-2

Malomo, D., DeJong, M. J., & Penna, A. (2019). Distinct element modelling of the in-plane cyclic response of URM walls subjected to shear-compression. *Earthquake Engineering & Structural Dynamics*, *48*(12), 1322–1344. https://doi.org/10.1002/EQE.3178

Malomo, D., Mehrotra, A., & DeJong, M. J. (2021). Distinct element modeling of the dynamic response of a rocking podium tested on a shake table. *Earthquake Engineering and Structural Dynamics*, *50*(5), 1469–1475. https://doi.org/10.1002/eqe.3404

Malomo, D., Morandini, C., Crowley, H., Pinho, R., & Penna, A. (2021). Impact of ground floor openings percentage on the dynamic response of typical Dutch URM cavity wall structures. *Bulletin of Earthquake Engineering*, *19*(1), 403–428. https://doi.org/10.1007/s10518-020-00976-z

Marques, R. (2015). Masonry Box Behavior. *Encyclopedia of Earthquake Engineering*, 1379–1396. https://doi.org/10.1007/978-3-642-35344-4_155

Mendes, N., & Lourenço, P. B. (2014). Sensitivity analysis of the seismic performance of existing masonry buildings. *Engineering Structures*, *80*, 137–146. https://doi.org/10.1016/j.engstruct.2014.09.005

Miranda, E., & Bertero, V. V. (1989). The Mexico earthquake of september 19, 1985—performance of low-rise buildings in Mexico City. *Earthquake Spectra*, *5*(1), 121–143. https://doi.org/10.1193/1.1585515

Mohebi, B., Yazdanpanah, O., Kazemi, F., & Formisano, A. (2021). Seismic damage diagnosis in adjacent steel and RC MRFs considering pounding effects through improved wavelet-based damage-sensitive feature. *Journal of Building Engineering*, *33*, 101847. https://doi.org/10.1016/J.JOBE.2020.101847

Monteiro, R., Marques, M., Adhikari, G., Casarotti, C., & Pinho, R. (2014). Spectral reduction factors evaluation for seismic assessment of frame buildings. *Engineering Structures*, *77*, 129–142.

Morandini, C., Malomo, D., & Penna, A. (2022). Equivalent frame discretisation for URM façades with irregular opening layouts. In *Bulletin of Earthquake Engineering* (Vol. 20, Issue 5). Springer Netherlands. https://doi.org/10.1007/s10518-022-01315-0

Orford, J. (1975). Alcoholism and marriage. The argument against specialism. *Journal of Studies on Alcohol*, *36*(11), 1537–1563. https://doi.org/10.15288/jsa.1975.36.1537

Pantò, B., Cannizzaro, F., Caliò, I., & Lourenço, P. B. (2017). Numerical and Experimental Validation of a 3D Macro-Model for the In-Plane and Out-Of-Plane Behavior of Unreinforced Masonry Walls. *International Journal of Architectural Heritage*, *11*(7), 946–964. https://doi.org/10.1080/15583058.2017.1325539

Parisi, F., & Augenti, N. (2013). Seismic capacity of irregular unreinforced masonry walls with openings. *Earthquake Engineering & Structural Dynamics*, *42*(1), 101–121. https://doi.org/10.1002/EQE.2195

Park, J., Towashiraporn, P., Craig, J. I., & Goodno, B. J. (2009). Seismic fragility analysis of low-rise unreinforced masonry structures. *Engineering Structures*, *31*(1), 125–137. https://doi.org/10.1016/j.engstruct.2008.07.021

PEER. (2015). *NGA-East : Adjustments to MedianGround-Motion Models for Central and Eastern North America*. Peer Report.

Pulatsu, B., Bretas, E. M., & Lourenço, P. B. (2016). Discrete element modeling of masonry structures: Validation and application. *Earthquake and Structures*, *11*(4), 563–582. https://doi.org/10.12989/eas.2016.11.4.563

Pulatsu, B., Erdogmus, E., Lourenço, P. B., Lemos, J. V., & Hazzard, J. (2020). Discontinuum analysis of the fracture mechanism in masonry prisms and wallettes via discrete element method. *Meccanica*, *55*(3), 505–523. https://doi.org/10.1007/s11012-020-01133-1

Pulatsu, B., Erdogmus, E., Lourenço, P. B., Lemos, J. V., & Tuncay, K. (2020). Simulation of the in-plane structural behavior of unreinforced masonry walls and buildings using DEM. *Structures*, *27*(August), 2274–2287. https://doi.org/10.1016/j.istruc.2020.08.026

Pulatsu, B., Gonen, S., Parisi, F., Erdogmus, E., Tuncay, K., Funari, M. F., & Lourenço, P. B. (2022). Probabilistic approach to assess URM walls with openings using discrete rigid block analysis (D-RBA). *Journal of Building Engineering*, *61*, 105269. https://doi.org/10.1016/j.jobe.2022.105269

Quagliarini, E., Maracchini, G., & Clementi, F. (2017). Uses and limits of the Equivalent Frame Model on existing unreinforced masonry buildings for assessing their seismic risk: A review. *Journal of Building Engineering*, *10*, 166–182. https://doi.org/10.1016/j.jobe.2017.03.004

Reed, J. W., & Kassawara, R. P. (1990). A criterion for determining exceedance of the operating basis earthquake. *Nuclear Engineering and Design*, *123*(2–3), 387–396. https://doi.org/10.1016/0029-5493(90)90259-Z

Rezavandi, A., & Moghadam, A. S. (2007). Experimental and Numerical Study on Pounding Effects and Mitigation Techniques for Adjacent Structures. *Advances in Structural*

Engineering, *10*(2), 121–134. https://doi.org/10.1260/136943307780429752

Robert McNeel and associates. (2007). *Grasshopper 3D*.

Saviano, F., Parisi, F., & Lignola, G. P. (2022). Material aging effects on the in-plane lateral capacity of tuff stone masonry walls: a numerical investigation. *Materials and Structures/Materiaux et Constructions*, *55*(7), 1–24. https://doi.org/10.1617/s11527-022-02032-5

Senaldi, I., Magenes, G., & Penna, A. (2010). Numerical investigations on the seismic response of masonry building aggregates. *Advanced Materials Research*, *133–134*, 715–720. https://doi.org/10.4028/www.scientific.net/AMR.133-134.715

Shrestha, B., & Hao, H. (2018). Building pounding damages observed during the 2015 gorkha earthquake. *Journal of Performance of Constructed Facilities*, *32*(2), 04018006. https://doi.org/10.1061/(asce)cf.1943-5509.0001134

So, E., & Spence, R. (2013). Estimating shaking-induced casualties and building damage for global earthquake events: A proposed modelling approach. *Bulletin of Earthquake Engineering*, *11*(1), 347–363. https://doi.org/10.1007/s10518-012-9373-8

Sołtysik, B., & Jankowski, R. (2013). Non-linear strain rate analysis of earthquake-induced pounding between steel buildings. *International Journal of Earth Sciences and Engineering*, *6*(3), 429–433.

Sołtysik, B., & Jankowski, R. (2016). Earthquake-induced pounding between asymmetric steel buildings. In *Geotechnical, Geological and Earthquake Engineering* (Vol. 40, pp. 255–261). Springer. https://doi.org/10.1007/978-3-319-14246-3_23

Tinawi, R., Mitchell, D., & Law, T. (1990). Les dommages dus au tremblement de terre du Saguenay du 25 novembre 1988. *Canadian Journal of Civil Engineering*, *17*(3), 366–394. https://doi.org/10.1139/l90-042

Tomassetti, U., Correia, A. A., Candeias, P. X., Graziotti, F., & Campos Costa, A. (2019). Two-way bending out-of-plane collapse of a full-scale URM building tested on a shake table. *Bulletin of Earthquake Engineering*, *17*(4), 2165–2198. https://doi.org/10.1007/s10518-018-0507-5

Tomaževič, M., Lutman, M., & Petković, L. (1996). Seismic Behavior of Masonry Walls: Experimental Simulation. *Journal of Structural Engineering*, *122*(9), 1040–1047. https://doi.org/10.1061/(ASCE)0733-9445(1996)122:9(1040)

Vanin, F., Penna, A., & Beyer, K. (2020). Equivalent-frame modeling of two shaking table tests of masonry buildings accounting for their out-of-plane response. *Frontiers in Built Environment*, *6*, 42. https://doi.org/10.3389/fbuil.2020.00042

Vermeltfoort, A. T., Raijmakers, T., & Janssen, H. J. M. (1993). *Shear tests on masonry walls*. 1183–1193.

Warnotte, V. (2007). Mitigation of pounding between adjacent buildings in earthquake situation . *ArGEnCo / Structural Engineering*, *PhD*, 214.

Wood, P., Robins, P., & Hare, J. (2010). Preliminary observations of the 2010 Darfield (Canterbury) earthquakes: An introduction. *Bulletin of the New Zealand Society for*

Earthquake Engineering, *43*(4), i–iv. https://doi.org/10.5459/bnzsee.43.4.i-iv

Wu, M. H., Wang, J. P., & Chiang, P. E. (2022). Cumulative absolute velocity (CAV) seismic hazard assessment for Taiwan. *Journal of Earthquake Engineering*, *26*(7), 3440–3460. https://doi.org/10.1080/13632469.2020.1803161

Yi, T., Moon, F. L., Leon, R. T., & Kahn, L. F. (2006). Analyses of a Two-Story Unreinforced Masonry Building. *Journal of Structural Engineering*, *132*(5), 653–662. https://doi.org/10.1061/(asce)0733-9445(2006)132:5(653)

Zhang, Z., Pulatsu, B., & Malomo, D. (2023). Fast and reliable in-plane seismic analysis of loadbearing masonry structures using DE macro crack networks. *In Proceedings of the 15th North American Masonry Conference*.